

# Methods and Devices for Optical and Electrical Metrology with Application to Phase-Shifting Interferometers, Torsional Microstructures, and Levitated Accelerometers

*David G Garmire*



Electrical Engineering and Computer Sciences  
University of California at Berkeley

Technical Report No. UCB/EECS-2007-118

<http://www.eecs.berkeley.edu/Pubs/TechRpts/2007/EECS-2007-118.html>

September 20, 2007

Copyright © 2007, by the author(s).  
All rights reserved.

Permission to make digital or hard copies of all or part of this work for personal or classroom use is granted without fee provided that copies are not made or distributed for profit or commercial advantage and that copies bear this notice and the full citation on the first page. To copy otherwise, to republish, to post on servers or to redistribute to lists, requires prior specific permission.

Methods and Devices for Optical and Electrical Metrology  
with Application to  
Phase-Shifting Interferometers, Torsional Microstructures, and Levitated Accelerometers

by

David Gordon Garmire

B.S. (Carnegie Mellon University) 2000

A dissertation submitted in partial satisfaction of the

requirements for the degree of

Doctor of Philosophy

in

Engineering-Electrical Engineering and Computer Sciences

in the

Graduate Division

of the

University of California, Berkeley

Committee in charge:

Professor James Demmel, Chair

Professor Richard S. Muller

Professor Carlo Séquin

Professor Sanjay Govindjee

Fall 2007

The dissertation of David Gordon Garmire is approved:

---

Professor James Demmel, Chair

Date

---

Professor Richard S. Muller

Date

---

Professor Sanjay Govindjee

Date

---

Professor Carlo Séquin

Date

University of California, Berkeley

Fall 2007

Methods and Devices for Optical and Electrical Metrology with Application to  
Phase-Shifting Interferometers, Torsional Microstructures, and Levitated Accelerometers

© 2007

by David Gordon Garmire

Abstract

Methods and Devices for Optical and Electrical Metrology

with Application to

Phase-Shifting Interferometers, Torsional Microstructures, and Levitated Accelerometers

by

David Gordon Garmire

Doctor of Philosophy in Computer Science

University of California, Berkeley

Professor James Demmel, Chair

Tiny variations in the fabrication process, environmental conditions, and operational dynamics of Microelectromechanical Systems (MEMS) can lead to devices that do not perform within the specified operating range, can plague the control of MEMS in precision-motion applications, and may ultimately reduce the commercialization of MEMS. We respond to this challenge by developing both *ex situ* (off chip), optical metrology techniques and *in situ* (on chip), electrical metrology techniques to precisely and inexpensively characterize the motion of MEMS and the variations inherent to the MEMS process. We apply these metrology techniques to (1) control a fast MEMS-based phase-shifting interferometer that allows the precise, realtime monitoring of microscopic phenomena, (2) control torsional microscanners for use in corneal laser surgery and cell-phone projectors, and (3) sense the motion of a MEMS-based levitated accelerometer for inexpensively and precisely measuring low-frequency seismic and instrumentation vibrations.

In more detail, our optical metrology contributions include both in-plane and out-of-plane measurement capabilities. We develop computer-vision algorithms to enable the teleoperation and automation of testing for MEMS. We also develop methods to rapidly monitor the in-plane and out-of-plane deformation of microstructures to compare simulation and experimentation and to enable the listed applications.

Our electrical metrology contributions include the development of devices and methods for in situ measurement of process parameters like the gap variation, effective Young's Modulus, and comb-drive forces using only electrical circuitry. We show that these measurements are at least as good as optical measurements of the same parameters. These techniques may lead to inexpensive process characterization and device control.

Finally, we create out-of-plane actuating and sensing devices using process developments for manufacturing vertically offset comb-drives. By applying our metrology methods, we demonstrate a fast phase-shifting interferometer that can capture and analyze out-of-plane motion at a rate of 20 Hz with a noise level having a standard deviation of 6 nm. We demonstrate a microscanner in the application of corneal laser surgery that improves over a present-day commercial corneal surgery apparatus. We also demonstrate a levitated accelerometer that has improved sensitivity over other types of accelerometers making it possible to measure low-frequency vibrations in an inexpensive process.

Chair \_\_\_\_\_

Date \_\_\_\_\_

Professor James Demmel

# Acknowledgements

I thank all of the members of my thesis committee for their patience, attention to detail, critical thought, and audience. I especially thank my advisor, Professor James Demmel, for giving me guidance through the years, preparing me for the harder times that lie ahead, and not only permitting me the freedom to follow my own path but encouraging me to do so. I also thank him for not giving up on me when the times were rough and continually providing me with sources of funding so that I could stay in school and afford all of the materials that made this study possible. I thank Professor Richard S. Muller for giving support, providing laboratory space to carry out my experiments, continually helping me improve my writing ability on our technical research papers, and teaching me some of the history behind the great discoveries of our time. I thank Professor Sanjay Govindjee for bringing me on-board the levitation project, introducing me to the computational problems facing mechanical simulations in MEMS, and for providing a computer and data acquisition hardware with which to conduct my experiments. I thank Professor Carlo Séquin for injecting enthusiasm, stirring up ideas, and showing that dreaming and technical research are not mutually exclusive.

Aside from my thesis committee, I thank the following people for support throughout my graduate studies:

- My wife, Lana, for her love, support, contribution, thoughts, and motivation,
- My parents for giving me motivation and helping to pay rent

- Colleagues Hyuck Choo, Rishi Kant, Sarah Bergbreiter, Babak Jamshidi, Debbie Jones, Rob Azevedo, Kaushik Datta, Westley Weimer, David Bindel, Jason V. Clark, and many others for giving me assistance when I needed it or just lending an ear.

# Table of Contents

Chapter 1: Introduction.....	1
1.1 Chapter Outlines and Key Contributions.....	4
Chapter 2: The Dilemma of MEMS Simulation.....	10
2.1 Problem Statement.....	10
2.2 Example Problem.....	13
2.3 Summary.....	20
Chapter 3: Optical Metrology Techniques.....	22
3.1 Motivation for Optical Metrology.....	22
3.2 In-plane Optical Metrology.....	24
3.3 Out-of-plane optical metrology.....	37
3.4 Summary of Optical Metrology.....	46
Chapter 4: Electrical Metrology Techniques.....	47
4.1 Motivation.....	47
4.2 Capacitance Sensing Theory.....	51
4.3 Capacitance Sensing Procedures and Details.....	57
4.3.1 Measurements.....	66
4.3.2. Levitation Effect.....	68
4.3.3. Cut-error Refinement.....	69
4.4 Results.....	70
4.5 Conclusions.....	72
Chapter 5: Reliable Out-of-plane Actuation and Sensing.....	74
5.1 Motivation for Vertically Offset Comb-Drives.....	74
5.2 Dynamics of Vertically Offset Comb-Drives.....	76
5.3 Fabrication of Vertically Offset Comb-Drives.....	77
5.4 Potential Applications of Vertically Offset Comb-Drives.....	84
5.4.1 Metrology for Characterizing Out-of-Plane Actuation and Sensing.....	85
5.4.2 Torsional Twist-Up Structures using Staggered Comb-drive Arrays.....	86
5.4.3 Deformable Parabolic Mirrors.....	88
5.5 Summary.....	90
Chapter 6: MEMS Metrology Applied to Enable Phase-Shifting Interferometry.....	91
6.1 Motivation for MEMS-based Phase-Shifting Interferometry.....	92

6.2 Time-domain Limitations .....	93
6.3 Phase-shifting Procedures.....	95
6.4 Fabrication and Characterization .....	98
6.5 Conclusions.....	104
Chapter 7: MEMS Metrology Applied to Enable Torsional-Microscanner Applications .....	106
7.1 Introduction.....	107
7.2 Design of the Torsional Microscanner.....	109
7.3 Fabrication of the Torsional Microscanner.....	111
7.4 Testing and Characterization of the Torsional Microscanner.....	113
7.5 Application of the Torsional Microscanner to Refractive Laser Surgery.....	114
7.6 Conclusions.....	121
Chapter 8: MEMS Metrology Applied to Enable Levitated Accelerometry .....	122
8.1. Equations of Motion .....	122
8.2. Diamagnetic Force.....	124
8.2.1 Diamagnetic Force Experimental Validation.....	125
8.3. Proof-of-Concept Results.....	126
8.4. Ideal Fabrication and Design .....	131
8.6. Conclusions.....	133
Chapter 9: Conclusion.....	134
Bibliography .....	137
Appendix.....	150

# Table of Figures

Figure 1: Traditional control-feedback architecture (Stengel 1994) (top) and a componentized MEMS architecture broken down into the subsystems: Controls, Simulation, Metrology, and Device ..... 13

Figure 2: Desired step function of the plate (left) and calculated forcing function (square of potential) applied to the comb drives (right) ..... 16

Figure 3: This schematic shows the plate that is moved vertically (top) with appropriate measurements shown (bottom). ..... 16

Figure 4: Actual step response of the plate for a 1% error in each spring parameter assuming open-loop control and stepping from 0 nm to 266 nm. .... 17

Figure 5: Table summarizing how much temperature, Young’s Modulus, and gap changes affect the governing parameters (stiffness (K), damping (D), mass (M), and force (F)) and then the parameters of interest (resonant frequency,  $f_r$ , settling time,  $t_s$ , and stepping position,  $y_s$ ). Each entry is the relative change in the row 1 parameter divided by the relative change in the column 1 parameter. .... 21

Figure 6: Teleoperated experimental setup derives from a Stroboscopic Microscopic Interferometer System (SMIS). The addition of the lamp allows the system to function as a microscope as well as an interferometer. .... 26

Figure 7: Automatic focus control is conducted on the torsional mirror. Focus as a function of z-axis displacement is plotted over 6 sample images and the minimum, maximum, and average focus scores are plotted (top). The resulting focus on a torsional scanner is shown at the bottom. .... 27

Figure 8: Pseudocode representing the iterative best-approximation algorithm. Note that a fit can be a line or an arc depending on which returns the lowest standard deviation (std). A fit also stores all of the pixels associated with that fit. .... 29

Figure 9: Extracted structural information is shown. Blue pixels are edge pixels returned by the Canny edge detector. Green pixels show the line and arc fits of the edge pixels. Red x’s show the end points (or corners) of the fits. .... 30

Figure 10: Pseudocode representing the pose consistency algorithm for establishing correspondence: Note that an optimization is to not include all chains, but just the “best” chains (which can be the longest chains so that their lengths and angles are known the best)..... 32

Figure 11: Extracted structural information is shown (left). The system calibrates the lateral motion of the stage by translating (center) and rotating (right) the sample and measuring the displacement of the image. Matching structural edges improves calibration speed. .... 32

Figure 12: The screen for the user at the remote terminal: The user centers the micromirror by a mouse click on the mask layout (top) and the system automatically centers the chosen mirror in the microscope view (middle). In a following experiment, dynamic deformation measurements are performed (bottom). .... 34

Figure 13: This sequence of figures shows the correspondence algorithm applied to a simulated suspension and a fabricated suspension when undergoing deformation produced from a probe tip (off-screen). .... 36

Figure 14: Phase-shifting interferometry using a Twyman-Green configuration (Malacara 1992). .....	38
Figure 15: Pseudocode representing the unwrapping of interferograms using breadth-first search. ....	40
Figure 16: Pseudocode representing the unwrapping of interferograms using hierarchical breakdown. Initially, DoRectangle can be called on the full array of pixels in the interferogram.....	42
Figure 17: Merge operation on subrectangle sets of pixels merging groups (shown in different colors) whose boundaries along the cut have a jump in values that is a multiple of $2\pi$ indicating that the surface should be smooth along that boundary.....	42
Figure 18: (prior art) Unwrapping interferograms by sweeping and using best previous row match.....	43
Figure 19: (prior art) Unwrapping interferograms by sweeping and using the best of the previous column match and the previous row match.....	43
Figure 20: (our work) Unwrapping interferograms using breadth-first search. The boxes illustrate slivers and pixilated noise.....	44
Figure 21: (our work) Unwrapping interferograms using hierarchical merging. There are still slivers, but not as large.....	44
Figure 22: Slice of a comb-drive with the y-component of the electric field superimposed .....	52
Figure 23: Metrology device schematic (top) and blow-up of the complementary comb-drive (bottom) .....	54
Figure 24: Simulation of complementary comb-drive – an equipotential surface is superimposed. Capacitances of A and B are subtracted over the motion of travel. Note that although the equipotential surfaces are similar, in A the electric field is larger as the two mating combs are closer to each other than in B. ....	56
Figure 25: Simulated results for complementary comb-drive – capacitance of B minus capacitance of A (blue) ( $h = 5 \mu\text{m}$ , $g = w = 3 \mu\text{m}$ , separation = 500 nm). ....	56
Figure 26: Simplified view of the measurement circuit.....	57
Figure 27: Overall device schematic; Note that electrical terminals are shown as italic letters in boxes. This device is an abstract representation of Figure 23. ....	59
Figure 28: Complementary comb-drive schematic (abstraction of the schematic shown at the bottom of Figure 23) (this figure is a blow-up of the orange rectangle surrounding D in Figure 27).....	61
Figure 29: Complementary comb-drive schematic (alternative) .....	62
Figure 30: Gap-closing sense schematic.....	63
Figure 31: Drive / Sense comb-drive schematic.....	64
Figure 32: Differential sense circuit schematic (does not include capacitive bypassing of the power supply).....	65
Figure 33: Overall circuit schematic with device terminals .....	66
Figure 34: SEM of fabricated device (left) with blow-up of complementary combs (top right) and fingers of a comb-drive set (bottom right) .....	71
Figure 35: Differential capacitance measurement from an SOI complementary comb-drive as comb-drive set 1 is actuated with a voltage. The 95% confidence interval is shown in the inset (red and green). .....	71

Figure 36: Vertical offset combs close-up; unactuated device (top), actuated device (bottom).....	77
Figure 37: Brief view of the process used to fabricate vertically offset combs.....	81
Figure 38: Uneven sidewalls as a result of the anisotropic silicon etch. ....	82
Figure 39: SEM image close-up shows the 25 $\mu\text{m}$ offset height on the combs for a 50 $\mu\text{m}$ thick device layer. The protective silicon dioxide layer is visible.....	83
Figure 40: SEM image close-up of the released vertically offset combs showing the clearly defined sidewalls and sharp edges (labeled). ....	84
Figure 41: Balanced twist-up structure. The three main bars along the shaft must be glued to the outer suspensions with insulative glue (epoxy) (Choo and Muller, 2003). ....	87
Figure 42: Sugar model of the twist-up. Note that the combs will always be aligned. ....	87
Figure 43: Mirror element made with vertical offset combs. ....	89
Figure 44: Mirror layout on a 1 cm by 1 cm chip that contains about 100K vertically offset comb fingers. Red (dark) represents the device layer, and purple (light) represents the offset-combs.....	89
Figure 45: Deformation of a mirror (radius = 10 mm, thickness = 2 mm) anchored in the center with uniform forces supplied at the 4 outer points. The deformation near the center is approximately parabolic.....	90
Figure 46: Error for each measurement using the standard and predictor-corrector methods along with the predictor-corrector estimated error. The contrast, B, and intensity, A, values were given 1% uniform random noise, and the average relative measured phase error using the predictor-corrector method was 1%. ....	94
Figure 47: Phase-shifting setup showing the collimated laser entering a beam splitter, one path reflecting off of the device under test (DUT), and the other path reflecting off of the MEMS plate which is shifted by $\lambda/8$ for each of the 4 phase-shifts. A CCD records the interference between the two paths.....	95
Figure 48: Phase-shifting by resonating the plate (top) and by stepping the plate (bottom). The blue (solid) curves show the plate motion over time, and the black dots show the time and shift of each laser pulse.....	96
Figure 49: All stages of phase shifting interferometry are shown. First, image 1, 2, 3, 4 with necessary phase offsets are shown. Second, the wrapped image is produced (bottom left). Finally, the image is unwrapped (bottom right).....	97
Figure 50: WYKO of MBPSI plate (top) and SEM of combs (bottom).....	99
Figure 51: Resonant-motion analysis for the phase-shifting MEMS mirror at 5 locations on the plate (left) and the linear region used for phase-shifting (right) (peak-to-peak deviation in position: < 6 nm). The 5 locations are shown in Figure 50 at locations labeled 1, 2, 3, 4, and the center of the plate.....	102
Figure 52: Measurement the response of a PZT stepper (device under test) using our MEMS-based phase shifting interferometer after the plate motion was characterized. .	103
Figure 53: Motion of stepping plate (top) driven by stepping function (bottom).....	104
Figure 54: The different components of a scanning mirror. Anchored components are shown in gray.....	110
Figure 55: SEM image of circular microscanners (5 kHz – 7 kHz resonant frequencies). .....	112
Figure 56: SEM image of rectangular microscanners (17 kHz – 24 kHz).....	112
Figure 57: Table representing different attributes of tested scanning mirrors.....	113

Figure 58: Scanning magnitude of the mirrors. ....	114
Figure 59: Ocular refractive surgery: a flap of tissue is removed from the cornea and the underlying area is ablated with an excimer laser to reshape the surface and correct the vision. ....	115
Figure 60: A single ablation (top) and multiple ablations (bottom): by using many ablations in the appropriate spots, the eye surface may be reshaped to correct vision... ..	116
Figure 61: Laser-scanning experimental setup showing the physical device setup (top) and system setup (bottom). ....	118
Figure 62: Comparison of ablating an image from a dime with our setup (top) vs. ablating an image of a penny with a state-of-the-art setup (bottom). ....	120
Figure 63: The accuracy of accelerometers using four different suspensions is measured by finding the standard deviation of the suspension response compared to a sinusoidal input at each frequency. ....	124
Figure 64: Two equipotential surfaces of the diamagnetic field above alternating north-pole and south-pole magnets (potential increases closer to the magnets). ....	125
Figure 65: We use Eq. 24 to predict the levitation height of the proof mass (a) under load and (b) with varying thicknesses of graphite. ....	126
Figure 66: Schematic of experimental setup (top); microscope photo of levitated proof mass (bottom left); the magnets under the levitated proof mass (bottom right). ....	128
Figure 67: Comparison of an ADXL 203 and the levitated accelerometer excited (a) and at rest (b). ....	129
Figure 68: Tilt of levitated proof mass that shows some out-of-plane effects in the first 0.4 seconds. ....	129
Figure 69: The fast phase-shifted interferometer (a) measures the acceleration (b) of the 300 kg air table after a 1.6 N impulse is applied to it. ....	130
Figure 70: The levitated proof mass construction. ....	132
Figure 71: Vertical sensing using offset combs. ....	133

# Chapter 1: Introduction

A majority of micro-electromechanical systems (MEMS) rely on electrical signals to generate mechanical motion or rely on mechanical motion to alter electrical signals. The generated mechanical motion may control some integrated system whether it be optical, microfluidic, or biological in nature. The altered electrical signals may represent the measurement of parameters such as acceleration, change in pressure, or change in strain. Whatever the transduction or sensing mechanism, the performance of the MEMS device will be subject to the variation in the electrical and mechanical components of the system. Someone designing algorithms for a computer or microprocessor system that is interfaced to such a MEMS device must then have knowledge of this variation to be able to develop robust algorithms to control it. If the knowledge of this variation does not exist, the control of the device will vary in unpredictable ways and reduce the accuracy of the device operation. On the flip-side of the coin, someone designing MEMS components for certain applications can and should use this knowledge to optimize the design. If the designer does not use this knowledge to optimize the design, variations may cause the MEMS devices to fail to meet the specification required of the application. In this thesis, we describe the methods of measuring variation in MEMS processes, simulation approaches to understanding variation effects on performance, and control and sensing techniques to surmount these variations. As a consequence of this work, we introduce new methods, devices, and controls for fast and accurate phase-shifting interferometry, microscanner-based displays, and levitated accelerometry.

A major challenge to successfully engineering MEMS for commercial applications has been that the mechanical and electrical operation of MEMS are sensitive to process and environmental variations (Tadigadapa and Najafi 2003). Similar problems faced CMOS integrated circuits as their sizes were scaled down. The solution for integrated-circuit reliability was to develop E-test structures that would allow for rapid measurement of electronic properties so that the semiconductor process could be improved and maintained (Qin, et al. March 2006). For MEMS, such rapid measurement techniques for the mechanical properties have been met with difficulty in their robustness to process variation and their ultimate reliance on using expensive imaging techniques like scanning electron microscopy (SEM) as one of their stages (Clark, Electro Micro-Metrology 2005).

There is little disagreement that measurement methods are required to characterize these variations. The types of measurement methods, also known as metrology, can range from an *in situ* method like electrostatic probing that usually involves the design of on-chip structures (e.g. E-test) to *ex situ* methods like interferometry and microscopy. While *ex situ* is useful for single-device, one-time characterization, *in situ* methods are preferred for continuous characterization of arrays of devices and for process monitoring and control across the processed wafer. Our work provides improvements to *ex situ* methods in terms of both spatial and temporal resolutions. Our work also provides answers to the primary challenges for *in situ* methods which involve precisely measuring mechanical properties of the processed materials through a novel measurement device and a

nondestructive, CMOS-compatible, all-electronic method that requires no difficult-to-determine apriori knowledge and requires relatively little area on the MEMS chip. This research demonstrates a means to integrate metrology devices and circuits together with the functional MEMS devices.

In this thesis, we detail an approach to developing and designing MEMS metrology that is robust to process- and environmental- variations that can improve device yield by making it possible process monitoring and adaptable MEMS control systems. This approach relies on two main advances: the development of new metrology devices and the advancement of simulation systems to rapidly model MEMS over the time domain.

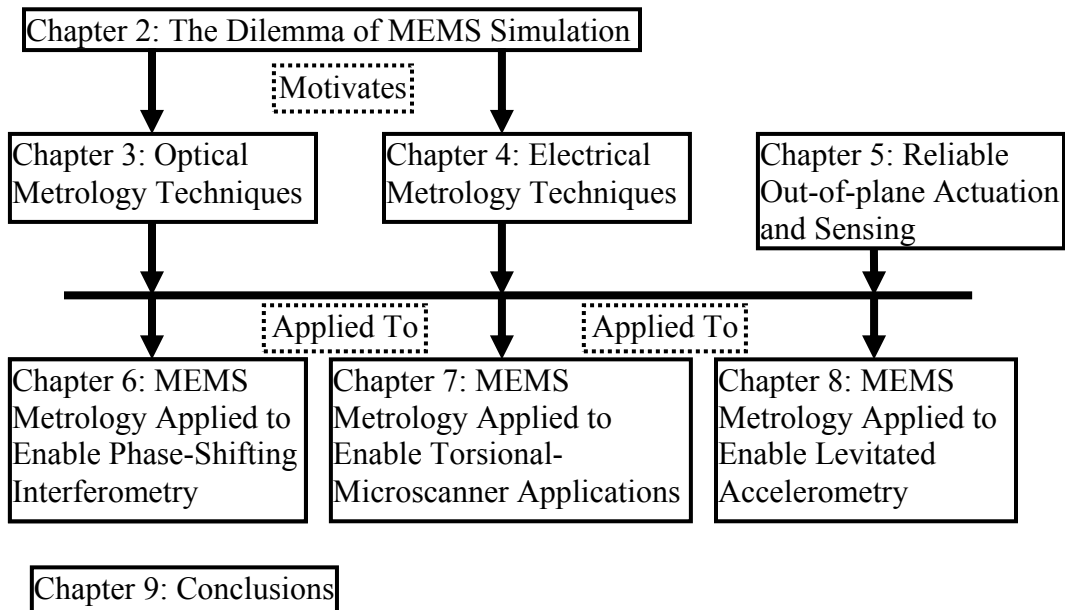
In addition to the core metrology developments, our invention of an entirely photolithographic process for creating vertically offset combs, described in later chapters, allows for structures that can be displaced and sensed out-of-plane to a high degree of accuracy. These advances usher in a new dimension in MEMS design. This extra dimension of design further necessitates adequate metrology and simulations to make use of the many possibilities that we describe here.

We organize the thesis into chapters that proceed from the motivation for metrology in a controls and simulation context to experimental work in the various application areas to which the research readily lends itself. Section 1.1 provides an outline of the thesis content.

## 1.1 Chapter Outlines and Key Contributions

The content of each chapter is briefly outlined and the key contributions are highlighted. Some of these contributions are qualitative in nature and can only be assessed subjectively. However, many of these contributions are quantitative improvements in terms of resolution, speed, or cost. The type of contribution, qualitative or quantitative, is also mentioned.

A flowchart showing the organization of the chapters follows for your convenience:



## **Chapter 2: The Dilemma of MEMS Simulation**

This chapter outlines the main simulation issues for MEMS, how simulation ties into the control and sensing of MEMS, and how metrology will solve some of the simulation issues that will, in turn, help improve the control and sensing of MEMS. Herein, we recommend a software decomposition that will provide a way to separate the complexity of the control algorithm from that of the simulation algorithm and that of the metrology tools.

### Contributions:

- (1) (Qualitative) Motivate metrology for MEMS in performing operational control enlarging on the conventional motivations such as process control and robustness.

## **Chapter 3: Optical Metrology Techniques**

This chapter covers work and advances using an optical microscope and laser interferometry for metrology. The highlights include a method to quickly match a microscope image of a device to its layout representation and then navigate to desired chip positions using an attached stage, a method to quickly unwrap phases in stroboscopic microscopic interferometry, and a method to perform dynamic deformation on the structure while matching this deformation to a simulation of the deformation.

### Contributions:

- (1) (Qualitative) Introduce fast algorithms for locating structures on chip, teleoperating experiments, and monitoring dynamic deformation of structures

- (2) (Quantitative) Develop breadth-first search phase-unwrapping algorithms in phase-shifting interferometry for (>100Hz) realtime processing of interferometric data
- (3) (Qualitative) Introduce new phase-unwrapping technique for reducing defects and improving accuracy of unwrapping

#### **Chapter 4: Electrical Metrology Techniques**

This chapter tells the background of metrology techniques that are purely electronic, discusses their limitations, and introduces theory and experiments that allow the extraction of process, material, and dynamic parameters for mechanical MEMS devices.

##### Contributions:

- (1) (Quantitative) Develop a structure and method of laterally and electrostatically positioning a stage to an accuracy of 1 angstrom. Current piezoelectric systems that can achieve a similar positioning resolution cost 100 times more.
- (2) (Quantitative/Qualitative) Develop a new kind of metrology structure and method that allow rapid determination of key parameters by purely electronic methods at a fast rate. Results exceed the reported resolutions of optical systems while the time to test an array of devices is smaller than conventional scanning electron microscope (SEM) or optical microscope measurements.

#### **Chapter 5: Reliable Out-of-plane Actuation and Sensing**

This chapter explores the characteristics and devices made possible in out-of-plane actuating systems. We introduce new methods of manufacturing the *vertically offset*

*comb-drive* for high-force actuators. We show that the creation of a staggered structure allows for large travel while maintaining a smooth force profile. Additionally, we show that out-of-plane actuating devices can bend surfaces for adaptive optics and focusing mirrors.

Contributions:

- (1) (Qualitative) Develop lithographically defined vertically offset combs and simulate a collection of devices that make use of out-of-plane actuation to achieve various effects.
- (2) (Qualitative) Introduce novel devices for generally extending the displacement allowed by out-of-plane actuating devices.
- (3) (Quantitative) Create the highest number (100,000) of comb-drives in a single MEMS actuator for an electrostatically adjustable mirror.

**Chapter 6: MEMS Metrology Applied to Enable Phase-Shifting Interferometry**

This chapter introduces a fast phase-shifting interferometer that can monitor the vertical displacement of surfaces at a resolution of less than 10 nanometers (nm) at a rate of 200Hz. It also shows how multiple wavelengths can be used to increase the dynamic range of the phase-shifting interferometer.

Contributions:

- (1) (Quantitative) Develop a fast phase-shifting interferometer and new adaptive method for processing that achieves camera frame-rate limited heightmaps. (100 times speedup over conventional phase-shifting interferometer)
- (2) (Quantitative) Develop a stepping control that lowers susceptibility to noise, allows for a lower-cost laser, and improves temporal and spatial resolutions.

## **Chapter 7: MEMS Metrology Applied to Enable Torsional-Microscanner Applications**

This chapter describes a set of mirrors that can reliably operate from 60 Hz to 22 kHz. We demonstrate with these mirrors a microscanning system that can ablate the surface of an eye in a precise manner achieving 0.1 $\mu$ m accuracy in laser placement.

### Contributions:

- (1) (Qualitative) Characterize dynamic deformation, torsional microscanner Q, and angle-of-deflection.
- (2) (Quantitative) Implement a novel method of mapping and calibration for use in corneal surgery. While achieving similar resolutions as present state-of-the-art systems, the cost of our new system is reduced by a factor of 100.

## **Chapter 8: MEMS Metrology Applied to Enable Levitated Accelerometry**

This chapter describes the use of diamagnetism in MEMS to achieve a measurement of 5 Hz accelerations with a resolution of 34 $\mu$ g<sup>1</sup> with electronic probing and 6 $\mu$ g with interferometric probing.

### Contributions:

- (1) (Qualitative) Develop and experimentally verified new simple formula to calculate diamagnetic levitation.
- (2) (Quantitative) Develop new low-cost method of achieving levitated accelerometry that has a lower noise floor than that of other electrostatically levitated accelerometers and can work in vacuum. (Achieved 6 $\mu$ g for seismic vibration levels of 5 Hz.)

---

<sup>1</sup>  $\mu$ g is a unit of acceleration,  $\mu$  means  $10^{-6}$ , and g means the acceleration due to Earth's gravity (9.8 m/s<sup>2</sup>)

## **Chapter 9: Conclusions**

Chapter 9 summarizes the findings of this research and develops perspectives on the impact of the results we have demonstrated on MEMS in the future.

## Chapter 2: The Dilemma of MEMS Simulation

This chapter details the problem of MEMS simulation and feedback control without metrology for time-sensitive and position-sensitive applications. Unlike prior motivations for metrology (Osterberg and Senturia 1997) (Gupta 2000) (Clark, Electro Micro-Metrology 2005) which focus on improving the MEMS fabrication process, this chapter motivates metrology for improving the robustness and responsiveness of MEMS in real-time feedback control for precision motion applications. Section 2.1 introduces the problem statement. Section 2.2 shows a simple problem that cannot be solved by traditional feedback control – how variations of parameters affect stepping a MEMS plate to precise locations. Section 2.3 summarizes how variations of parameters affect the governing system of equations, how rapidly parameters change, and how metrology will benefit precision motion control.

### 2.1 Problem Statement

The main challenge to create a “good” simulation of a device is to accurately correlate the simulation to actual behavior of the simulated device. A simulation is of value to the user only if the user can make critical decisions from this information. The simulated behavior should allow an automated system to make critical control decisions from it. Therefore, being able to simulate and model the device directly results in the controllability and ultimate utility of the engineered system.

Only recently, with the invention of fast digital processors, do we have the ability to produce realistic simulations of engineered structures that can be used to control those engineered structures in real time (requiring typically rates faster than 1 kHz). Traditional approaches to controlling devices without simultaneously simulating their behavior rely on feedback control (Stengel 1994) (Preumont 2002) where the controlled device must be designed to provide sensing of the current state of the device (also known as the reference of the device). In the case of MEMS, a reference is hard to produce because the reference itself is affected by variations in the process. Furthermore, without calibration of how input signals affect the resulting device, traditional feedback control is hampered by the time it takes to accurately estimate the model parameters. Traditional feedback control will fail to make MEMS operate satisfactorily for applications where parameters change more rapidly than the rate at which the devices need to be controlled. Even in the case of adaptive optics for astronomy, where arrays of MEMS components need to be operated at rates of 1 kHz, changes in temperature can fluctuate by more than 1% in 1 ms due to thermal fluctuations of ground-based systems and this instrumental thermal background is often the final limitation of the adaptive-optics system (Nakajima 2001). Section 2.2 explains how this fluctuation in temperature affects the performance of MEMS-based components.

To further compound the simulator's dilemma in the MEMS domain, our ability to model the micro- and nano-world is often limited. In macro-scale systems, variations in processing and manufacturing of devices are easily measured to within a tolerable accuracy that can be preloaded into the simulation system controlling the behavior of the

macro-scale device. Typically the simulation system is almost trivially simple, and is completely embedded into the control algorithm for the device. However, on the MEMS scale, variations of the engineered system have a considerable impact on MEMS performance and commercialization (Tadigadapa and Najafi 2003).

The significant variability and the effects of the variability on the MEMS operation necessitate a more complex simulation and control system that can correct itself for the variations present. We observe that this variability breaks the traditional methods of embedding the entire simulation system into the controlling algorithm. From an overall-design perspective, it makes sense to separate the simulation system from the controlling algorithm.

**Figure 1** illustrates the traditional feedback control loop (Stengel 1994) and also outlines the added components that this research examines – metrology and simulation.

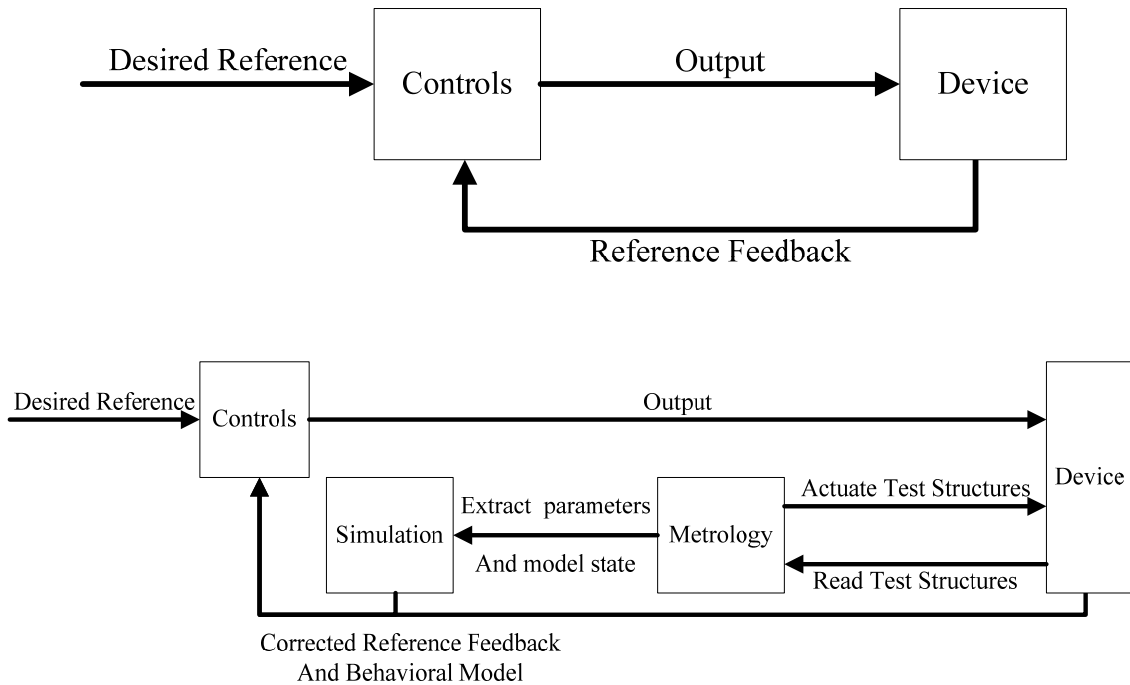


**Figure 1: Traditional control-feedback architecture (Stengel 1994) (top) and a componentized MEMS architecture broken down into the subsystems: Controls, Simulation, Metrology, and Device**

## 2.2 Example

By adding simulation and metrology components, precision applications of MEMS can be realized. To demonstrate our point, let us consider a simple problem. We would like to step a vertically actuated plate at various heights. For use in certain applications, like adaptive optics and interferometry, even a 1% variation of the step motion of this plate is detrimental. The present standard for an interferometer requires a positional resolution better than 1 nm, and a 1% variation in the step motion of the plate corresponds to more than a 2 nm variation in positional resolution, twice the standard accuracy achieved in interferometry using other more-expensive techniques (Hart, et al. 2000).

We consider this simple problem because generating a step function for a MEMS device is also the first step towards controllably generating many more-complicated MEMS driving functions that are not at the resonant frequency of the manufactured device. These devices are useful for optical attenuation (Isamoto, et al. May 2004), scan positioning (Carley, Ganger and Nagle 2000), and even sound generation (Diamond, Neumann and Gabriel June 2003).

The plate in our example is affected by three main process parameters: the Young's Modulus ( $E$ ) of the material, the gap variation ( $e$ ), and sidewall angle ( $\alpha$ ). Environmentally changing parameters that may also affect the performance of the stepping plate include temperature ( $T$ ) and humidity ( $H$ ) (pressure has relatively little effect on any of the parameters). For the demonstration of our ideas, we focus on gap variation ( $e$ ) and temperature ( $T$ ). The moving-plate system is chosen as an example because it is relatively simple device to actuate, to sense, and to model. However, processing and environmental variations can make it a difficult system to control.

The simple spring, mass, and damping system is typically modeled as (Thomson 1988)

$$F(t) = Ky(t) + D\dot{y}(t) + M\ddot{y}(t) \quad \text{Eq. 1}$$

where  $F$  represents the applied force,  $K$  is the stiffness of the system,  $D$  is the damping,  $M$  is the mass, and  $y$  is the vertical position. Variations in the sizes of the forcing function, stiffness, damping and mass of the system will perturb the system. The perturbed system may be written as

$$p_F(F(t), t) = p_K(K, t)y(t) + p_D(D, t)\dot{y}(t) + p_M(M, t)\ddot{y}(t). \quad \text{Eq. 2}$$

The perturbation function,  $p$ , could be a general perturbation. For the purpose of this example, we will use a linear perturbation that does not change over time:  $p_s(S, t) = S(1 + \Delta S)$ . Our desired step function for the plate's vertical position can be represented as a logistic function so as to produce a finite acceleration. Variations of the parameters (gap variation, temperature, etc...) result in two important problems: an incorrect step height,  $y_s$ , and oscillations that require a time,  $t_s$ , to subside below a tolerable amount (about 2 nm for our system). The desired step function and driving function to produce this step function are plotted in Figure 2. Figure 3 shows the type of suspension used to build this system. The system represents a spring with mass,  $M = 6 \times 10^{-9}$  kg, damping,  $D = 2.6 \times 10^{-6}$  kg/s, and stiffness,  $K = 0.02$  kg/s<sup>2</sup>. The Q factor of this system can be computed as  $Q = \sqrt{KM}/D$ . The Q factor represents the number of cycles it takes for the system to lose 0.9981% of its energy through damping (Crowell 2002). The natural resonant frequency of this system,  $f_r$ , can be computed as  $f_r = \frac{1}{2\pi} \sqrt{\frac{K}{M}}$ . Therefore, the settling time of the oscillating system,  $t_s$ , is proportional to  $Q/f_r$  or, by simplifying, proportional to  $M/D$ . For this system,  $Q \approx 4.29$  and  $f_r \approx 292$ . Ideally, reducing the mass or increasing the damping will shorten the settling time of the system. However, the mass is often limited by the area, wafer-thickness, and materials required for the device (especially in this case for a phase-shifting component). The damping is also bounded because the potential required to drive the device cannot exceed a certain amount. Due to the design limitations, controllability of the device then demands that we measure the physical parameters of the system. Therefore, a metrology component to the system is necessary.

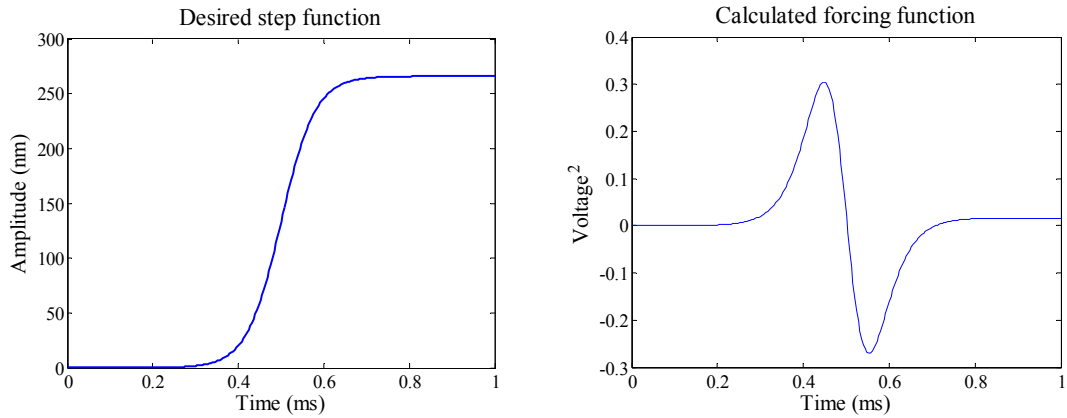


**Figure 2: Desired step function of the plate (left) and calculated forcing function (square of potential) applied to the comb drives (right)**

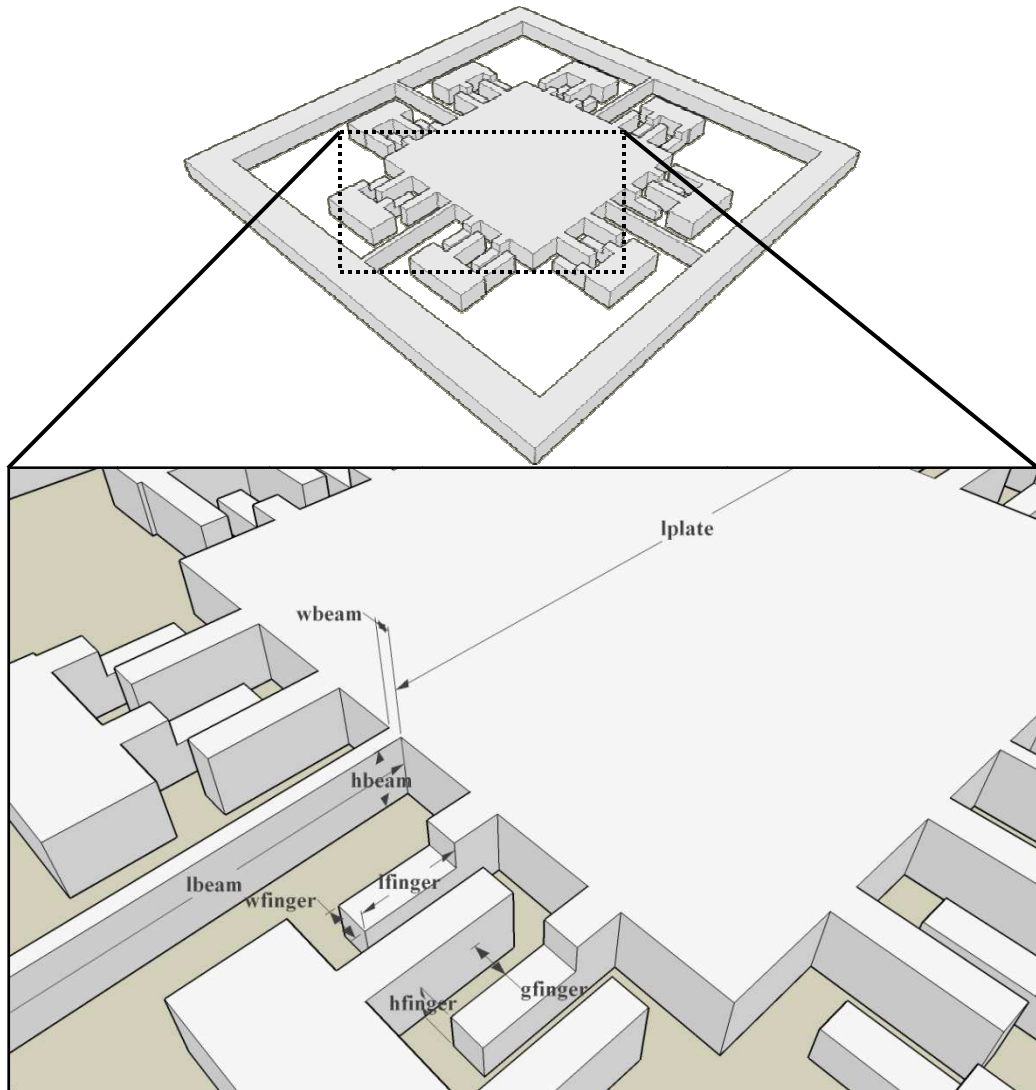


**Figure 3: This schematic shows the plate that is moved vertically (top) with appropriate measurements shown (bottom).**

If the parameters that control the motion of the plate ( $K$ ,  $D$ ,  $M$ , and  $F$  from Eq. 1) are inaccurate, the resulting motion of the plate driven by the ideal forcing function (right-side plot of **Figure 2**) will no longer follow the desired step function (left-side plot of **Figure 2**). Figure 4 shows the consequences of a  $\pm 1\%$  deviation of each parameter. In an interferometer, a 1% variation of plate position will lead to a 1% error in the measured displacement and will exceed the typical system error of 0.1% due to noise (Hart, et al. 2000).

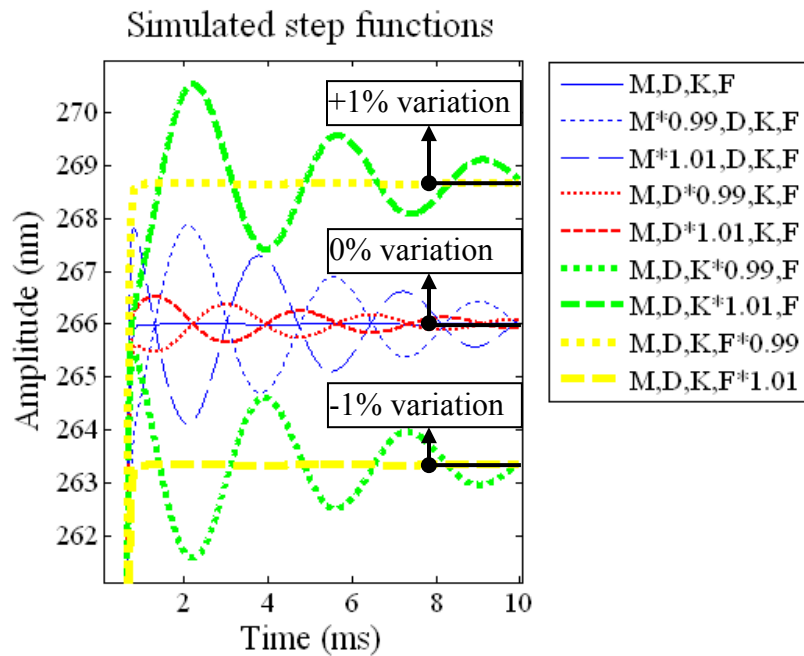


**Figure 4: Actual step response of the plate for a 1% error in each spring parameter assuming open-loop control and stepping from 0 nm to 266 nm.**

Each parameter is individually affected by the gap variation,  $\Delta g$ , (or negative of the beam width variation). We can write the stiffness, damping, and forcing functions in terms of the variables shown in **Figure 3**. For the beam stiffness, we use a cantilever beam that is fixed at both ends. For air damping, we only need to consider the Couette-Stokes damping across the comb-drive (Veijola and Turowski 2001). For this reason, out-of-

plane actuators have a higher Q than in-plane actuators. **Figure 4** is produced by using the following equations inserted into Eq. 2 with the forcing function shown in **Figure 2**.

$$K = 4 \cdot 2 \cdot E \left( \frac{h_{\text{beam}}}{l_{\text{beam}} + 2\Delta g} \right)^3 (w_{\text{beam}} - \Delta g) \quad \text{Eq. 3}$$

$$D = \eta_{\text{air}} \frac{N_{\text{gaps}} l_{\text{finger}} h_{\text{finger}}}{g_{\text{finger}} + \Delta g} \quad \text{Eq. 4}$$

$$M = \rho_{\text{silicon}} \left( N_{\text{gaps}} \frac{(h_{\text{beam}} + h_{\text{finger}})}{2} (l_{\text{finger}} + \Delta g) (w_{\text{finger}} - \Delta g) + h_{\text{beam}} (l_{\text{plate}} - \Delta g)^2 \right) \quad \text{Eq. 5}$$

$$F = \epsilon_0 \epsilon_{\text{air}} \frac{N_{\text{gaps}}}{2} \frac{l_{\text{finger}}}{g_{\text{finger}} + \Delta g} V^2 \quad \text{Eq. 6}$$

In Eq. 3 - Eq. 6, the variables are defined as follows:

- E Young's Modulus
- $h_{\text{beam}}$  Defined in **Figure 3**, height of suspension beam
- $l_{\text{beam}}$  Defined in **Figure 3**, length of suspension beam
- $w_{\text{beam}}$  Defined in **Figure 3**, width of suspension beam
- $g_{\text{finger}}$  Defined in **Figure 3**, gap between vertically offset comb fingers, also g
- $\Delta g$  Gap variation
- $\eta_{\text{air}}$  Viscosity of air
- $N_{\text{gaps}}$  Number of gaps used in the actuation of the plate
- $h_{\text{finger}}$  Defined in **Figure 3**, height of vertically offset comb finger
- $l_{\text{finger}}$  Defined in **Figure 3**, length of vertically offset comb finger
- $w_{\text{finger}}$  Defined in **Figure 3**, width of vertically offset comb finger
- V Applied potential difference across comb drive
- $\rho_{\text{silicon}}$  Density of silicon
- $\epsilon_{\text{air}}/\epsilon_0$  Permittivity of air / permittivity of free space

The effects of thermal fluctuations on the various operating parameters (K, M, D, and F) are now systematically considered. For simplicity, we consider that the thermal effects change all geometric dimensions of the device equally. However, if multiple layers are used in the construction of the MEMS device and the coefficients of thermal expansion are different for the material used in each layer, then there will be curvature changes to the structures in response to the residual strain gradient (Fang and Wickert 1996). Thermal effects cancel out in the determination of the actuation force, F. Thermal effects will not change the mass although they may change the mass distribution and should be taken into account for torsional structures. Thermal effects will change the stiffness by generally decreasing the Young's Modulus (in the case of Silicon) and increasing the beam width. The thermal effect on K as a function of temperature variation from room temperature,  $\Delta T$ , can be found by using the linear coefficient of thermal expansion for Silicon,  $3 \times 10^{-6}/^\circ\text{K}$ , and the linear coefficient of Young's Modulus change,  $-64 \times 10^{-6}/^\circ\text{K}$  (Jeong, et al. August 2003). Thus,

$$K(\Delta T) \approx K(1 + 3 \times 10^{-6}\Delta T)(1 - 64 \times 10^{-6}\Delta T) \approx K(1 - 61 \times 10^{-6}\Delta T). \quad \text{Eq. 7}$$

From Eq. 7, a 1% change in the stiffness of the suspension would require over  $150^\circ\text{K}$  change in temperature. However, damping of the suspension will be more directly affected by a change in temperature. The viscosity of air is directly proportional to the square root of temperature (in  $^\circ\text{K}$ ) (Williams 1926), but we can rewrite this relationship in terms of temperature variation from room temperature as well (see Eq. 8).

$$\eta_{\text{air}}(\Delta T) \approx \eta_{\text{air}} \left( \sqrt{1 + \Delta T/294} \right) \approx \eta_{\text{air}}(1 + 1701 \times 10^{-6}\Delta T). \quad \text{Eq. 8}$$

Therefore,

$$D(\Delta T) \approx D(1 + 1.7 \times 10^{-3}\Delta T)(1 + 3 \times 10^{-6}\Delta T) \approx D(1 + 1.7 \times 10^{-3}\Delta T). \quad \text{Eq. 9}$$

From Eq. 9, only a 10°K change in temperature is necessary for a 1 percent change in the damping coefficient of the spring system. Therefore, as we can see from **Figure 4**, thermal changes will mainly impact the damping coefficient changing the settling time of the plate in our example.

## 2.3 Summary

The stiffness, damping, and electrostatic position sensing and actuation forces are functions of process and environmental variations. Without metrology structures, robust control of MEMS is impossible for applications requiring precise positioning capabilities. Figure 5 summarizes how each of the governing terms of Eq. 1 is affected by variations of parameters. The issues described here are further amplified when multiple steps are involved. This amplification is especially true in high-Q devices where the energy of the noise inserted into the system cannot be quickly removed.

Each element of the table in **Figure 5** lists the “magnitude” of the effect where “magnitude” is defined by the relative change in the column 1 elements ( $\Delta K$ ,  $\Delta D$ , etc...) divided by the relative change in the parameters in row 1 ( $\Delta T$ ,  $\Delta E$ ,  $\Delta g$ ). Initial ambient conditions are assumed to be at standard (room) temperature and pressure (300°K, 1 atm). For example, a +1% change in E causes a -1% change in  $y_s$ .

	Temperature	E (Young's Modulus)	g
<b>K</b>	0.02	1.0	$-g/w_{\text{finger}}$
<b>D</b>	0.46	0.0	-1.0
<b>M</b>	0.0	0.0	$\approx 0.0$ ( $I_{\text{plate}} \gg g$ )
<b>F</b>	-0.001	0.0	-1.0
$f_r \propto \sqrt{(K/M)}$	0.01	0.5	$-g/(2 w_{\text{finger}})$
$t_s \propto M/D$	-0.46	0.0	1.0
$y_s = F/K$	-0.021	-1.0	$g/w_{\text{finger}} - 1.0$

**Figure 5: Table summarizing how much temperature, Young's Modulus, and gap changes affect the governing parameters (stiffness (K), damping (D), mass (M), and force (F)) and then the parameters of interest (resonant frequency,  $f_r$ , settling time,  $t_s$ , and stepping position,  $y_s$ ). Each entry is the relative change in the row 1 parameter divided by the relative change in the column 1 parameter.**

For MEMS commercialization, the need for metrology is clear and does not rely solely on the improvement of MEMS processing conditions. For reliable operation of MEMS, one must either control the environment in which the device operates, or else measure its ambient environment and use this information to control the device. Controlling the environment for MEMS is often costly, involving the encapsulation and removal of outgassing elements in the MEMS process (Candler, et al. August 2003). The added cost of these processes may make the use of MEMS impossible. As discussed in this chapter, if one has an accurate measurement of the operating MEMS device, one can build a system to make use of that information and maintain accurate control over that device in spite of the variability of the process and environmental conditions.

## Chapter 3: Optical Metrology Techniques

This chapter introduces optical metrology techniques to address some of the challenges posed in Chapter 2. Section 3.1 motivates the use of optical metrology as an inexpensive technique for measuring single MEMS devices. Section 3.2 focuses on in-plane optical metrology using white-light microscopy. Computer-vision algorithms are applied to allow the teleoperated testing of MEMS instead of intervention by a human operator. Section 3.3 focuses on out-of-plane optical metrology using a stroboscopic microscopic interferometry system (SMIS) developed at Berkeley (Hart, et al. 2000). Phase-unwrapping algorithms are created that allow for real-time processing of interferometric data and reduce defects in the unwrapped interferograms. Section 3.4 summarizes our key contributions in both vision algorithms used in in-plane optical metrology and in out-of-plane interferometric techniques.

### 3.1 Motivation for Optical Metrology

As mentioned in Chapter 1, measuring properties of the MEMS fabrication process and environmental conditions comes down to two main inexpensive approaches: electronically probed measurements (discussed in Chapter 4) and optical measurements (discussed here). Optical measurements can give detailed information on the deformation and operation of the actuated MEMS devices (Marshall 2001) (Hart, et al. 2000). Optical metrology has several advantages as a measurement technique. Photons are inexpensive and easy to generate and typically CMOS imagers provide a wealth of information from a

compact, easy-to-manufacture device (Yadid-Pecht December 2004). Furthermore, interesting information can be readily extracted from these data and used in layout verification (Baidya, Gupta and Mukherjee 2002). With algorithms introduced here, we show that functional testing and metrology of MEMS can be automated and teleoperated using computer-vision algorithms (Forsyth and Ponce 2002).

It is helpful to look from the business perspective to see why it is important to carry out such research in optical metrology techniques. Business growth relies on reducing cost. For a semiconductor business, the wafer is usually a fixed cost. To steadily decrease the cost per unit, a business must steadily decrease the sizes of the devices that accomplish the same task (Wright 2006). This reduction in size has the disadvantage of making it harder to identify and test devices on the processed wafer. A microscope allows a user to test such small devices and observe what device is being tested. If a human must carry out this placement and testing of devices, it is a very labor-intensive (expensive) and tedious job. Fortunately, a CCD can record the information that the microscope is viewing and allow a computer to automate the testing procedure. However, the reduction in sizes of devices also has the disadvantage of increasing the area density of devices over the wafer making it hard to identify where on the wafer the microscope is viewing. Therefore, automated optical testing requires the development of advanced algorithms to take the place of a human tester in locating and aligning the device under test (DUT). These algorithms are presented in Section 3.2.

While optical measurements are currently an inexpensive type of measurement to make for measuring a single device, electronically obtained measurements are less expensive for arrays of devices in terms of labor and may currently be done *in situ* rather than in a laboratory. Electronically obtained measurements will be introduced and described in Chapter 4. While this contrast is necessary to understand the present state-of-the-art, it is important to note that optical measurements may eventually be able to catch up with electronically obtained measurements in controlling individual devices because CMOS imagers can in some cases be integrated into the MEMS process (Afghahi 2004).

### 3.2 In-plane Optical Metrology

Microscopy is one of the most inexpensive approaches to spatially viewing single or small numbers of microscale devices. Unfortunately, many tasks remain in making it easy to understand and measure devices through microscopy. We approach this problem by employing techniques in computer vision. First, we automate the task of bringing MEMS structures into focus in the CCD camera which before would require human labor. Next, we calibrate the viewed motion of the stage to sub-micron accuracy regardless of the configuration of the stages by extracting and monitoring features from the image while the stages are operated. Before, it would require the system operator to precisely configure the stages used and calibrate each stage individually, and even then it would be hard to exceed 1  $\mu\text{m}$  in positioning accuracy. In contrast, our system can automate this process, remove the manual calibration stage, and dynamically recalibrate the stage control to within 1  $\mu\text{m}$  positioning accuracy (as the motion control drifts over time).

Then, we reconstruct the structures that are in the view of the microscope. Finally, we produce correspondence between devices defined in the mask layout for the chip and the current view of the manufactured structures. This correspondence is important because it allows the user to click on a view of the device layout, and then the system automatically positions the desired device into the view of the microscope. The result is that the system provides an interface that allows teleoperated and automated control and testing of MEMS devices.

This section is based in part on our publication in *Optical MEMS* (Garmire, Muller and Demmel, Vision-based Teleoperation of a Stroboscopic Microscopic Interferometric System for Remote Dynamic MEMS Testing August 2005). The system hardware configuration is shown in **Figure 6**. To summarize the operation of this system, the designer provides the layout of the MEMS chip specified in a CIF-formatted computer file (Hon and Sequin 1980). The system finds the best matches of the CCD image with the chip-layout. As necessary, the system operator manipulates the user interface to resolve ambiguities arising from duplicate MEMS devices. As a consequence, when the operator selects a device to view on the CIF plot, the system moves the stage directly to the corresponding structure on the specimen stage. Testing and characterization can then be performed. We demonstrate teleoperation of this system from a remote site, locating and aligning a torsional scanning mirror. We then carry out a dynamic-deformation experiment using the stroboscopic microscopic interferometer system (SMIS) (Hart, et al. 2000).

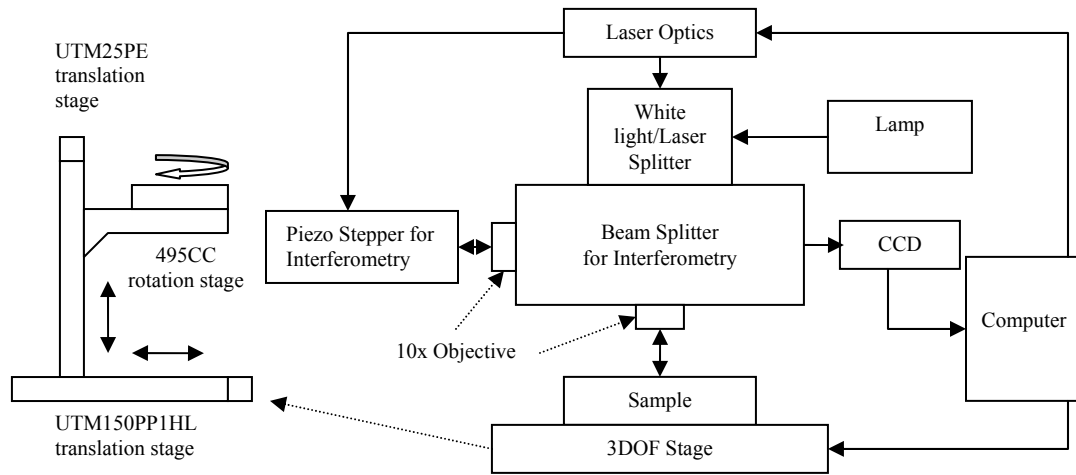


**Figure 6: Teleoperated experimental setup derives from a Stroboscopic Microscopic Interferometer System (SMIS). The addition of the lamp allows the system to function as a microscope as well as an interferometer.**

First, the MEMS device is brought into focus in the optical microscope. This task is accomplished by using a Laplacian function to measure the degree-of-focus of the system (McKeogh, Sharpe and Johnson 1995). The larger the Laplacian, the sharper is the appearance of the edges. To obtain a single measurement of the degree-of-focus, the Laplacian is summed over all pixels (infinity norm of the individual per-pixel Laplacian). Note that the Laplacian is also used by a Canny edge detector (Canny 1986) to locate edges, so this focusing stage is important for good edge detection. Because different MEMS layers are separated by not more than a few microns, it is possible to focus on most of the structures using this technique. However if resolving multiple layers independently is desired, then each layer can separately be brought into focus (also dependent on the magnification used for the objective). We will assume that a globally chosen  $z$ -axis position is adequate for having all of the necessary structures in focus. The result of automatically focusing on a torsional scanner is shown in **Figure 7**.

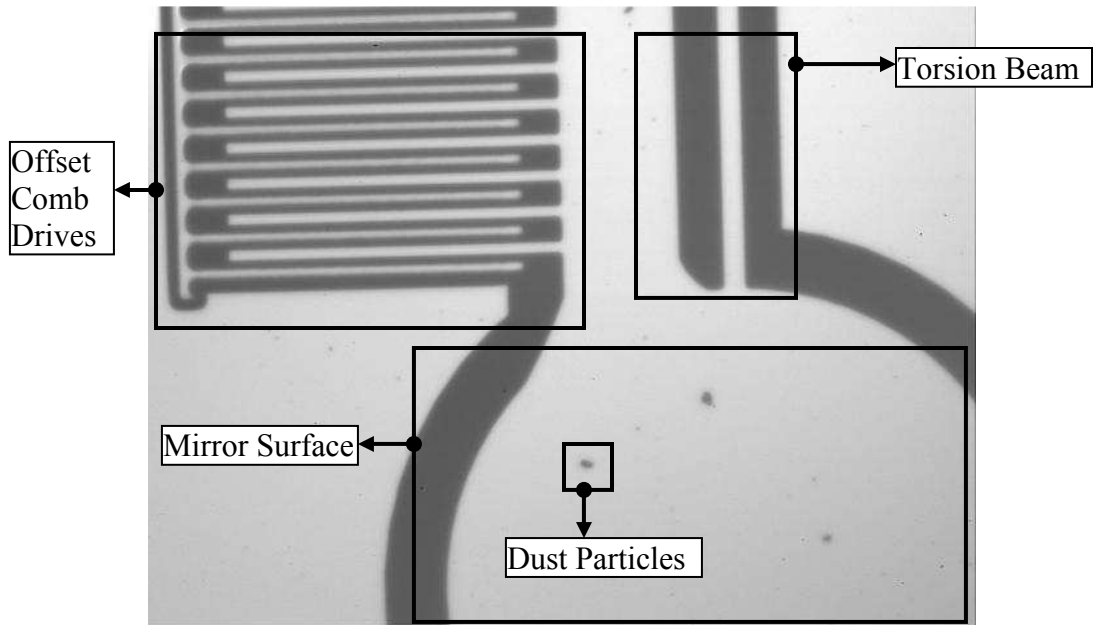
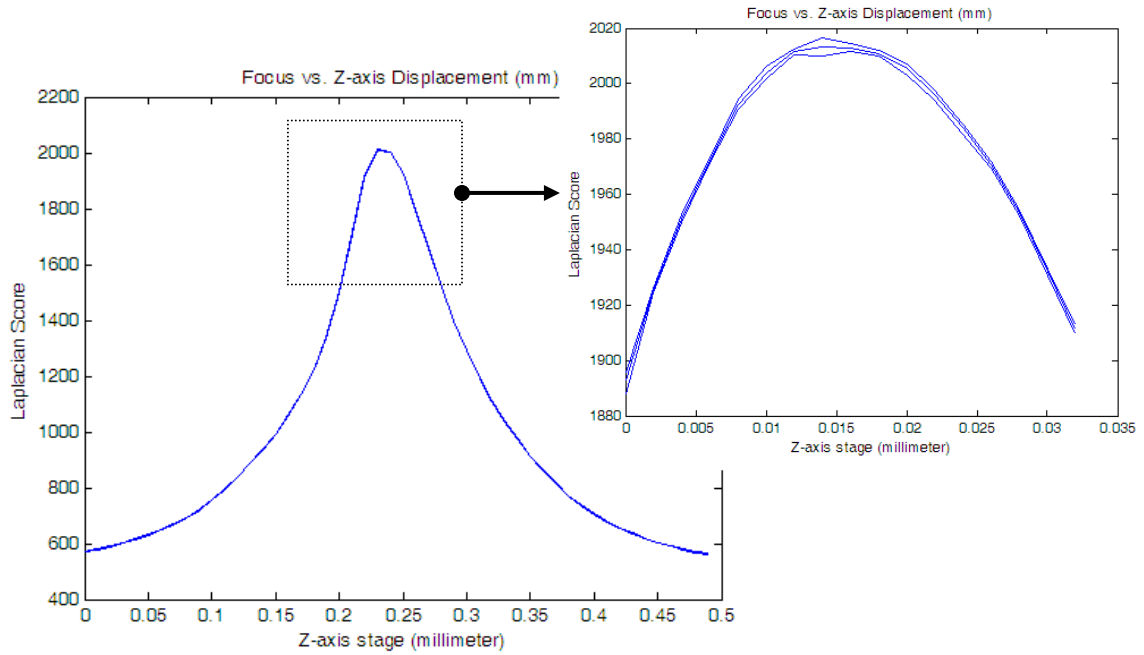


**Figure 7: Automatic focus control is conducted on the torsional mirror. Focus as a function of z-axis displacement is plotted over 6 sample images and the minimum, maximum, and average focus scores are plotted (top). The resulting focus on a torsional scanner is shown at the bottom.**

An excellent feature of MEMS is that the layers are relatively smooth and device structures are outlined by sharp shadows. This fact allows the outline of each structure to be readily detected by applying a Canny edge detector (Canny 1986). In order to remove broken edges in the edge-detection data, hysteresis is used.

An alternate approach to using a Canny edge-detector is to use an interpolation technique. This technique works by considering the image as a union of quadratic functions. Because the light intensity from a single light source incident on a planar surface can be represented as a quadratic function, representing the planar processed MEMS structures as a set of quadratic functions appears to make sense and would allow for a technique for separating the different layers. However, we have found that solving this interpolation problem is slower than the Canny edge-detector technique for locating edge pixels.

Once the edge pixels are determined via the Canny edge-detector, the next task is to determine the structure of the device from those pixels. A similar process of successive approximation is used. Groups of pixels that form lines and circles are continually fitted. The better fitting lines are merged together until there are no pairs of lines that can be merged without exceeding a prespecified tolerance. When two pairs of line segments or arc segments intersect, the resulting intersection point is labeled as a corner. Pseudocode summarizing the software implementation of this procedure to extract structure from the set of edge pixels is shown in **Figure 8**. The full implementation is located at <http://www.cs.berkeley.edu/~strive>. Example results are shown in **Figure 9**.

```

Procedure Canny(P: array of m by n pixels)
    Returns set of edge pixels, E // use (Canny 1986)

Procedure Structure(P: array of m by n pixels)
    Returns F, a set of structures (lines and arcs)
    fit from P
E = Canny(P)
Initialize fits, F = ()
For each edge pixel, p1
    For each neighboring edge pixel of p1, p2
        F = F U (Line between p1 and p2)
While there are still potential fits to merge
    For each fit, F1 ∈ F
        BestMerge = null
        BestMergeScore = Inf
        For each neighboring fit of F1, F2
            If (std(fit(F1, F2)) <= BestMergeScore)
                BestMerge = F2
                BestMergeScore = std(fit(F1,F2))
        End For
        If BestMergeScore is a low enough error
            Remove F1 from F
            Remove BestMerge from F
            F = F U fit(F1, BestMerge)
            Merge neighbors of F1 and BestMerge
    End For
Return F

```

**Figure 8: Pseudocode representing the iterative best-approximation algorithm. Note that a fit can be a line or an arc depending on which returns the lowest standard deviation (std). A fit also stores all of the pixels associated with that fit.**

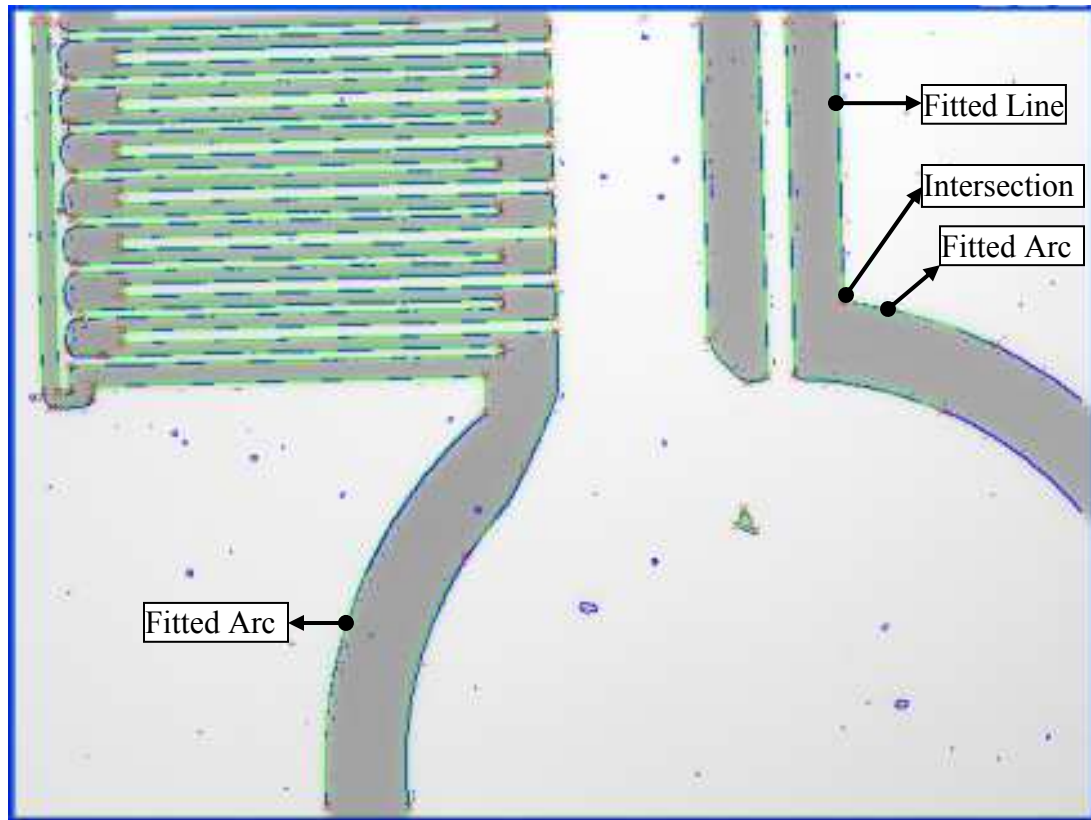


**Figure 9: Extracted structural information is shown. Blue pixels are edge pixels returned by the Canny edge detector. Green pixels show the line and arc fits of the edge pixels. Red x's show the end points (or corners) of the fits.**

Next, structural information must be extracted from the lines and arcs and their intersection points. The extraction process is facilitated by the observation that a microscope view of a microstructure is Euclidean. This observation means that angles and ratio of line segment lengths will be invariant under rotation and scaling that happens in microscopy. The first step of the extraction process is then to form identifiable chains of segments. The angle and ratio of lengths of these line segments are stored in a hash table. It is very easy to produce a similar hash structure from parts stored in a CIF file.

A correspondence between the two structural views (the extracted structure from the camera view, and the structure from the CIF file) can then be produced by a standard

pose-consistency technique. To measure the pose-consistency, we count the number of corner points that fall within some distance of each other. This is an ideal, easily calculated quantity. A point-matching technique can be used to speed up counting the number of points that match. Further refinement to this matching can be accomplished by also matching the line and arc connections. These procedures are summarized by the pseudocode listed in **Figure 10**.

```

Procedure Strings(Ch: a chain)
    Returns: Str, A string representing Ch
    Divide all lengths by the longest length in Ch
    Fit, F = beginning fit of Ch
    Str = concat(" ", length(F))
    For F1 = fit adjacent to F
        Str = concat(Str, angle(F1, F))
        Str = concat(Str, length(F1))
        F = F1
    Return Str

Procedure ChainHash(F: a set of structural fits)
    Returns: H, a hashtable of chains
    Initialize set of corner points, Corners = ()
    For each fit, F1 ∈ F
        For each neighbor fit, F2 ∈ N(F1)
            Corners = Corners ∪ intersect(F1, F2)
    Initialize hashtable of chains, H() = ()
    For each corner, C ∈ Corners
        For all chains, Ch, connected to C
            H(Strings(Ch)) = Ch // insert in hash
    Return H

Procedure PoseConsistency(F1, F2 : structural fits)
    // F1 is of microscope image, F2 is of CAD file
    Returns BestTransform, the best correspondence
    H1 = ChainHash(F1)
    H2 = ChainHash(F2)
    BestScore = Inf
    BestTransform = null
    For each chain, C1, in H1
        Lookup C2 = H2(C1)
        If C2 exists

```

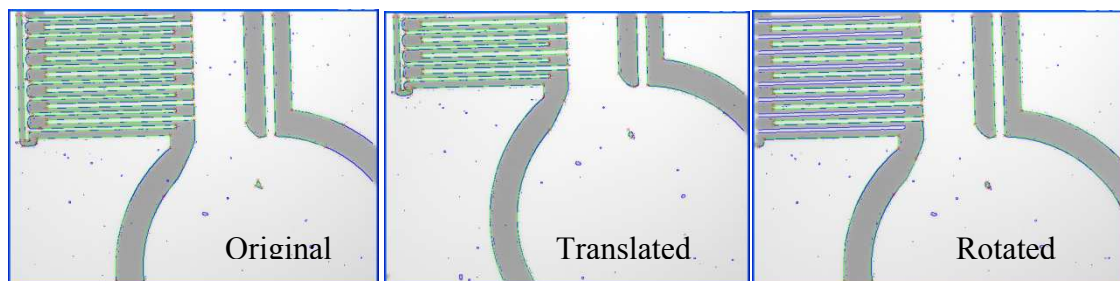
```

Calculate transform, T, such that  $T(C1) = C2$ 
Score = Sum(Distance between corners in
            T(C1) and C2)
If Score < BestScore
    BestScore = Score
    BestTransform = T
End For
Return BestTransform

```

**Figure 10: Pseudocode representing the pose consistency algorithm for establishing correspondence: Note that an optimization is to not include all chains, but just the “best” chains (which can be the longest chains so that their lengths and angles are known the best).**

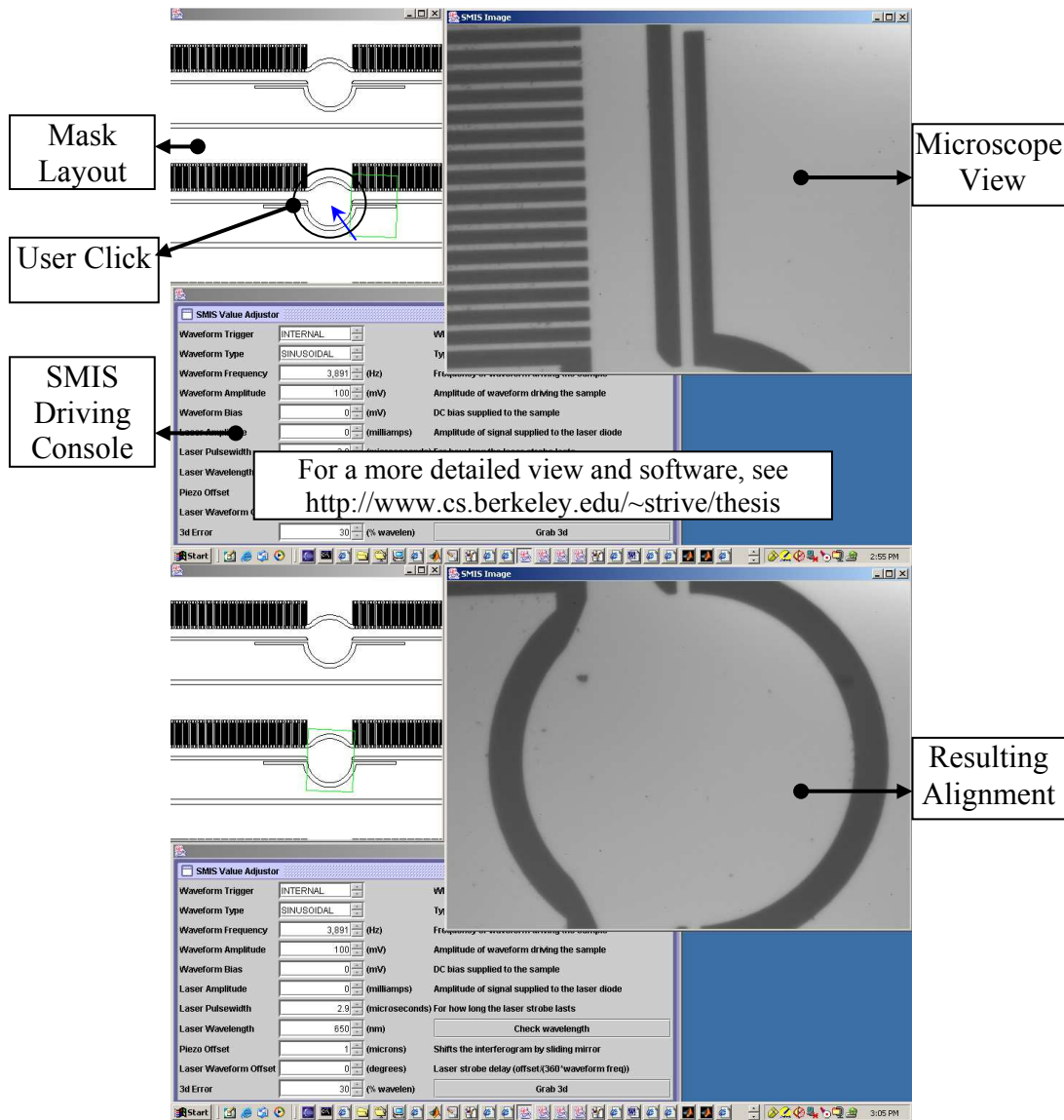
Calibration of the stage is then carried out by translating and rotating the stage and determining how far the structures in view were translated and rotated (see **Figure 11**). The extracted stage parameters then relate the position and rotation of the stage to the image location.

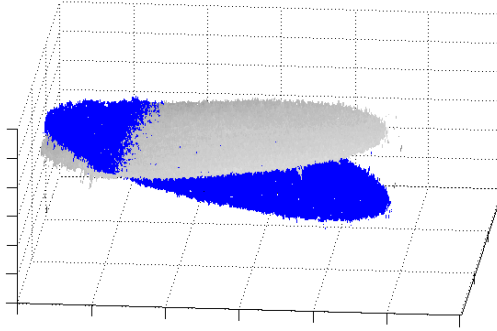


**Figure 11: Extracted structural information is shown (left). The system calibrates the lateral motion of the stage by translating (center) and rotating (right) the sample and measuring the displacement of the image. Matching structural edges improves calibration speed.**

Finally, these defined steps allow us to implement the end system. The structural information from the CAD file (in our specific example, a CIF file) is first analyzed and stored. Then the user places the fabricated chip under the microscope. The current view is focused and the structural information is extracted. The stage parameters are calibrated. A

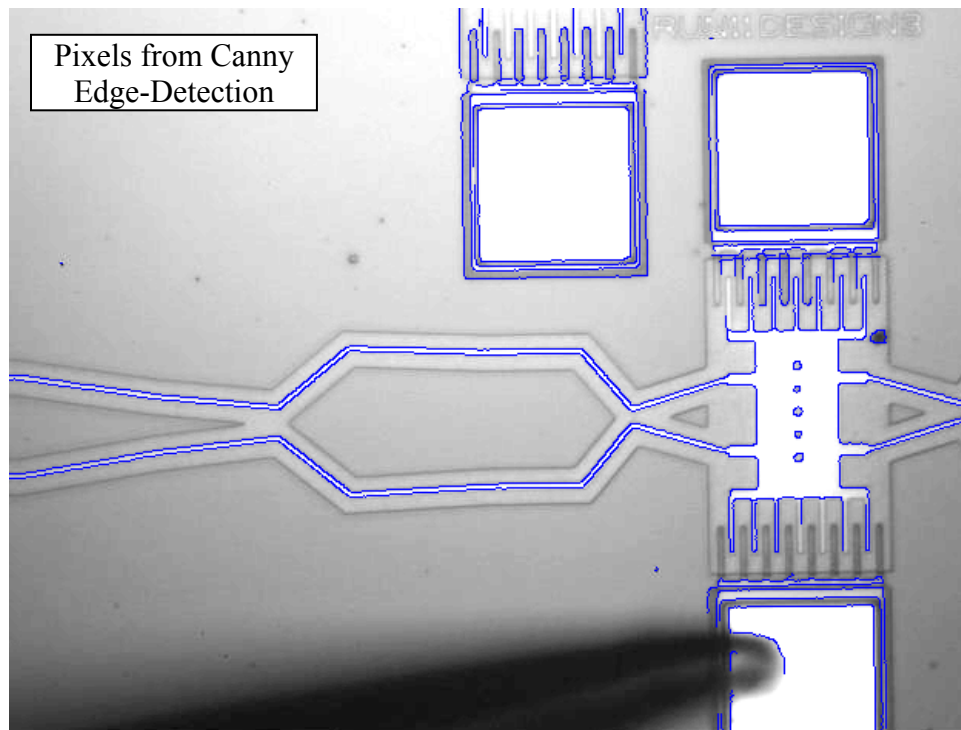
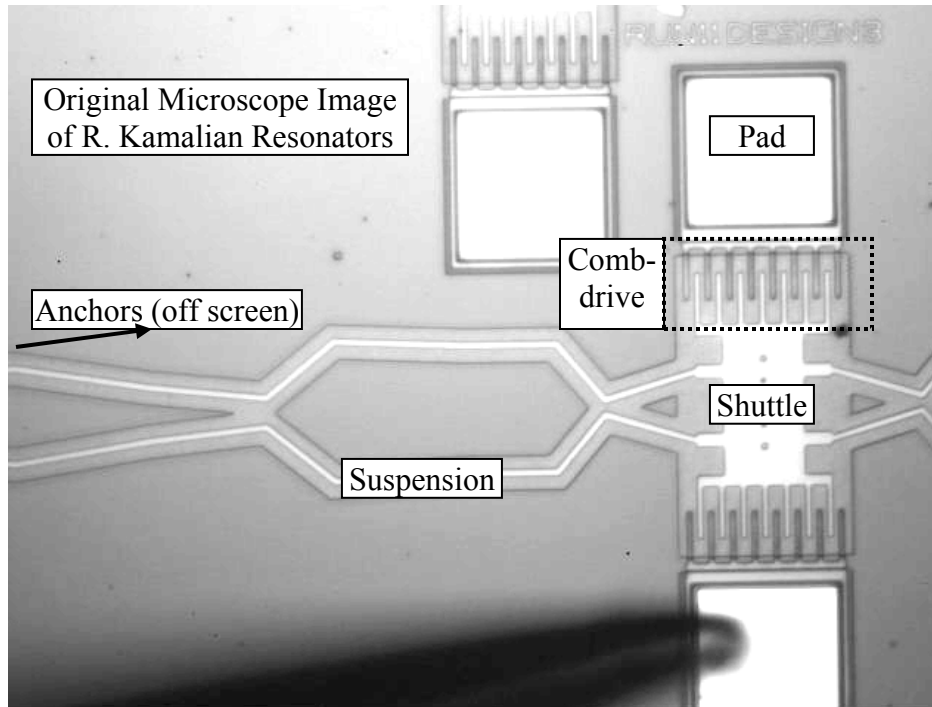
user can click on the CIF view and the system will move the microscope to view the desired device. The device may then be actuated and measured. These steps are shown in **Figure 12** which also shows our user interface.





**Figure 12: The screen for the user at the remote terminal: The user centers the micromirror by a mouse click on the mask layout (top) and the system automatically centers the chosen mirror in the microscope view (middle). In a following experiment, dynamic deformation measurements are performed (bottom).**

Now that a correspondence is established, dynamic deformation of MEMS may also be observed. In the next example, we deform a suspension with a probe-tip and relate the deformation back to a simulation of the suspension done in SUGAR (Clark, Zhou, et al. 2000). The suspension was a produced through a genetic algorithm in previous research (Kamalian, Takagi and Agogino 2004). This deformation allows a rough measurement of how well simulation of the device matches reality. Using our algorithms, we find that there is less than a micron difference between the deformation of the fabricated device and a simulation of the deformation using SUGAR.



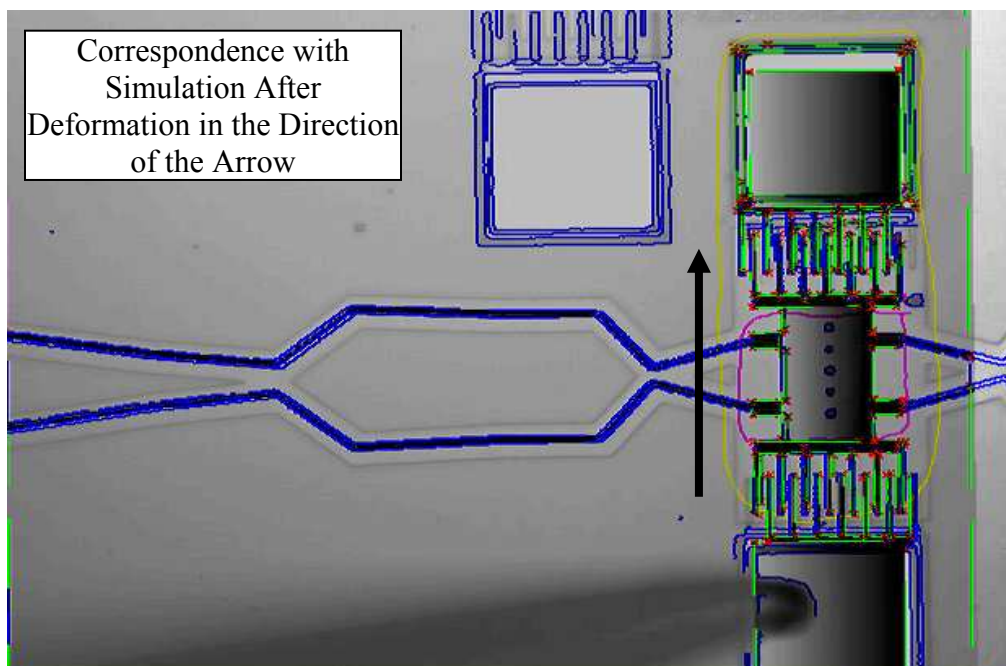
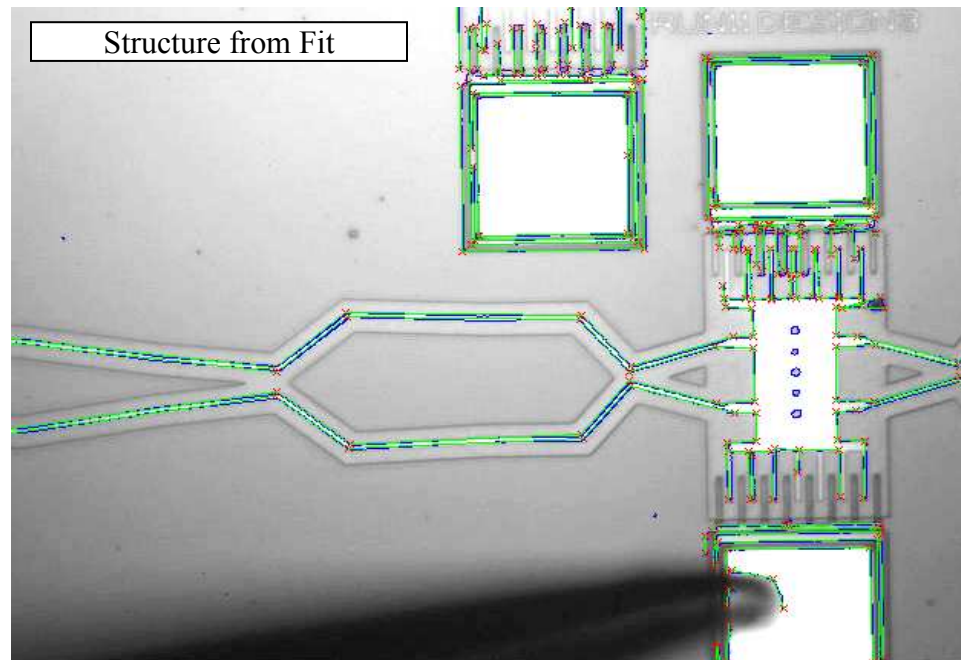


**Figure 13:** This sequence of figures shows the correspondence algorithm applied to a simulated suspension and a fabricated suspension when undergoing deformation produced from a probe tip (off-screen).

This research presents a new convenient technique to build an automated, teleoperated, computer-controlled stage that enables optical examination of extremely tiny microsystems.

### 3.3 Out-of-plane optical metrology

This section will discuss the limitations of the interferometers in measuring MEMS and our developments in stroboscopic interferometry for time-resolving down to 1 nanometer motion of MEMS devices in the out-of-plane direction. Specifically, our contribution is in creating an algorithm to unwrap interferograms in real time at rates faster than 20 Hz (or under 5 milliseconds (ms) per interferogram) while maintaining a high quality of unwrapping. These results are useful in fast phase-shifting interferometry that is discussed in further detail in Chapter 6.

Measuring out-of-plane motion is important for out-of-plane actuation systems. The resolution of out-of-plane measurement is far superior to the in-plane resolution limits because it is not diffraction limited. A well-made interferometer can easily attain a resolution of 1 nm on a flat surface. Coupling the in-plane and out-of-plane resolution limits yields an angular resolution better than 0.2 arcseconds for a 1mm flat plate.

Phase-shifting interferometry is achieved by splitting a laser through a beam splitter, reflecting the two paths that the laser takes off of the sample as well as a reference plate, recombining the two paths and measuring the interference off of a CCD (see Figure 14).

Height changes across the surface of the Device Under Test (DUT) will result in brighter or darker images depending on whether the difference in the path lengths leads to constructive or destructive interference (respectively).

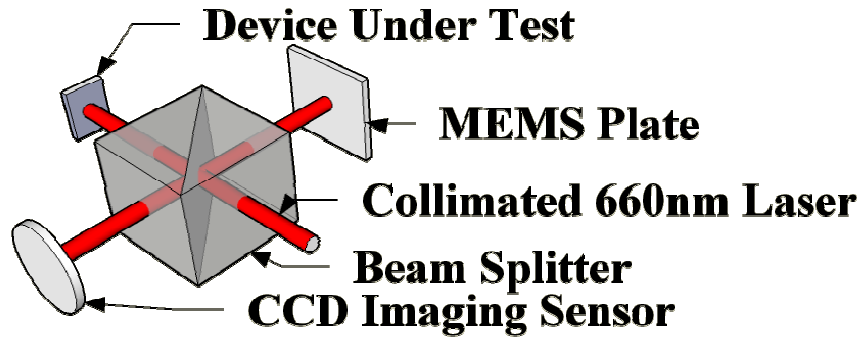


**Figure 14: Phase-shifting interferometry using a Twyman-Green configuration** (Malacara 1992).

The brightness turns out to be a sinusoidal function of the phase difference between the two path lengths of the light reaching a single pixel (this intriguing result is due to the fact that light travels with a sinusoidally-varying electric field). The formula for the intensity of each pixel is shown Eq. 10, where  $I(x, y, t)$  represents the intensity of pixel  $(x,y)$  at time  $t$ ,  $\varphi_{\text{surf}}$  is the phase offset of the surface being examined,  $\varphi_{\text{mirror}}$  is the phase-offset of the reference mirror,  $A$  is a parameter representing the intensity value, and  $B$  is a parameter representing the contrast value.

$$I(x, y, t) = A + B\cos(\varphi_{\text{surf}}(x, y, t) - \varphi_{\text{mirror}}(x, y, t)) \quad \text{Eq. 10}$$

We need to solve for the  $A$  and  $B$  values as well as the phase-offset of the surface,  $\varphi_{\text{surf}}$ , to determine the height of the pixels. In order to do so, we can shift the mirror by four  $\pi/2$  offsets, measure the intensity, and solve for the phase (see Eq. 11). All of the phases will be accurate modulo  $2\pi$  and can therefore resolve heights modulo the wavelength of laser-light divided by 2 (in the Twyman-Green configuration (Malacara 1992)). For

reconstructing the final surface, the  $2\pi$  jumps in pixel values need to be correctly accounted for (“unwrapped”). For surface jumps that are larger than  $2\pi$ , there is no way to reconstruct the surface with a single laser wavelength.

$$\begin{aligned}
 I_1 &= A + B\cos(\varphi_{\text{surf}}) \\
 I_2 &= A + B\cos(\varphi_{\text{surf}} + \pi/2) \\
 I_3 &= A + B\cos(\varphi_{\text{surf}} + \pi) \\
 I_4 &= A + B\cos(\varphi_{\text{surf}} + 3\pi/2)
 \end{aligned}
 \tag{Eq. 11}$$

$$\varphi_{\text{surf}} \equiv \text{atan}(I_4 - I_2, I_1 - I_3) \pmod{2\pi}$$

There are a few algorithms for unwrapping the phases that trade off speed for quality. An obvious fast technique is to simply iterate through each row of pixels and then make a determination of how many  $2\pi$  jumps there are between that pixel and the previously unwrapped point (Pritt 1996). This approach unfortunately results in many slivers that are incorrectly mapped due to surface roughness. Once a single incorrect offset is made, the error propagates along the entire row. Another approach that we introduce is to use a breadth-first search approach which reduces the occurrence of slivers, but does not reduce their size when they occur. The breadth-first search approach is simply accomplished by having a queue of pixels that are “connected” in that they are considered not to have significant jumps in intensity between them. While there are neighboring pixels that are not connected, put them on the queue. Continue until there are no more pixels to be connected for this connected group. Repeat these processes until the entire set of pixels belong to a connected group and are unwrapped. The pseudocode is shown in **Figure 15**. On a 656 by 491 pixel image on a 3.6 GHz Pentium Dual-core processor, the algorithm runs in 3.9 ms. The runtime and memory consumption is linear with respect

to the number of pixels,  $O(p)$ . The algorithm is very simple to implement however several artifacts do exist. Results on an example PolyMUMPS device are shown in **Figure 20**. The breadth-first search algorithm yields far fewer defects than running simple linear scans which has many obvious mismatches.

```

Procedure findnearestB(A : double, B : double)
    Returns A + chk, the value of  $B+n*2*\pi$  closest to
    A, where n is an integer
chk = (B-A) mod (2* $\pi$ )
If chk >  $\pi$ , then chk = chk - 2* $\pi$ 
Return A + chk

Procedure GetConnected(A : array of pixels,
    Visited : array telling if pixel visited or not,
    (x, y) : a start position)
    Returns nothing (operates on A)
Init. Queue, Q = (element of array A at location x, y)
While Q is not empty
    Get next pixel to examine, P = pop(Q)
    For each neighbor, N of P
        If !visited(N.x, N.y) &&
            |findnearestB(P.value, N.value)-P.value|<0.1
            N.value = findnearestB(P.value, N.val)
            push(N, Q)
    End For
End While

// unwrapping then is simple and follows
Forall x and y, Visited(x,y) = 0
Forall x and y,
    if !Visited(x, y) GetConnected(A, x, y)

```

**Figure 15: Pseudocode representing the unwrapping of interferograms using breadth-first search.**

To limit the size of artifacts and further optimize the process, we introduce a spatial decomposition approach. The idea is to decompose the space by subdividing rectangles (cut each rectangle in half along the largest dimension), to unwrap each sub-rectangle,

and then merge the two solutions to unwrap the larger rectangle (merge operation shown in **Figure 17**). This approach does not require any queue, but it does require the ability to merge two connected groups from each subrectangle. This merge operation can be done through path compression which will result in a runtime of  $O(p \log \log p)$  (Tarjan 1979). However, it is usually simpler to individually propagate the match to all of the connected pixels of one group resulting in a runtime of  $O(p \log p)$ . This approach is also more robust at handling noise because when a decision is made to merge two groups, it can use more information (all of the adjacent pixels along the cut) to make a decision.

To summarize and illustrate our contributions, consider **Figure 18** – **Figure 21**. Of the procedures that can run in real time, breadth-first search and our hierarchical approach produce better results in terms of number and size of fragments (or slivers). These procedures have been optimized to run at 20 Hz. Code is available online at:

<http://www.cs.berkeley.edu/~strive>.

```

Procedure Merge(P1, P2: two strips of pixels bordering
each other)
  Returns nothing (updates the associated array)
For  each subset of pixels, p1∈P1 and P2∈P2,
neighboring each other, all elements of p1
belonging to the same group, g1, and all elements
of p2 belonging to the same group, g2
  If  $\sum_i (|p1(i) - \text{findnearest}(p1(i), p2(i))|) < \text{maxerr}$ 
    Merge groups g1 and g2 into a new group, g3
    Add offset to all of g1 so border matches

Procedure DoRectangle(starti, startj, endi, endj)
  Returns nothing (updates the associated array)
If(starti == endi && startj == endj) return
If(endj - startj > endi - starti)
  midj = (startj+endj)/2
  DoRectangle(starti, startj, endi, midj)

```

```

DoRectangle(starti, midj+1, endi, endj)
Merge on boundary pixels
Else
midi = (starti+endi)/2
DoRectangle(starti, startj, midi, endj)
DoRectangle(midi+1, startj, endi, endj)
Merge on boundary pixels

```

**Figure 16: Pseudocode representing the unwrapping of interferograms using hierarchical breakdown. Initially, DoRectangle can be called on the full array of pixels in the interferogram.**

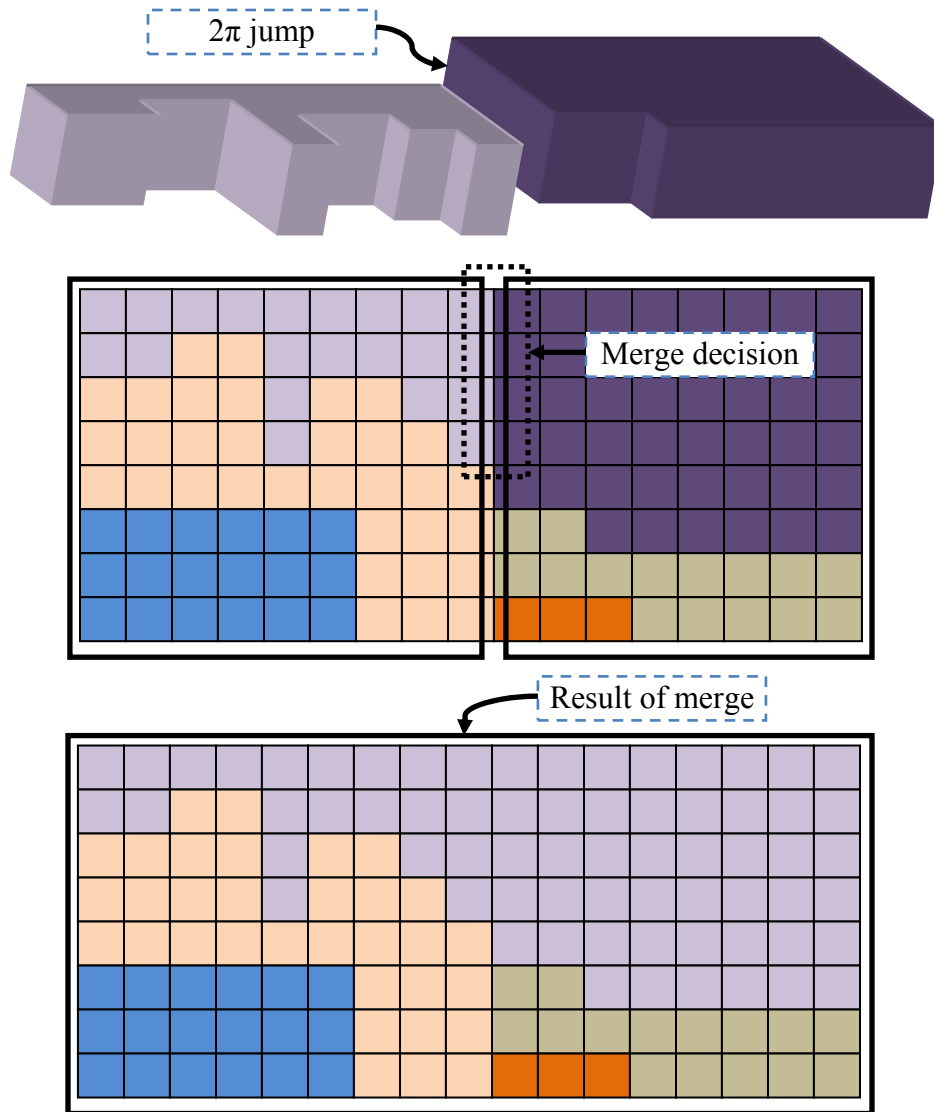


**Figure 17: Merge operation on subrectangle sets of pixels merging groups (shown in different colors) whose boundaries along the cut have a jump in values that is a multiple of  $2\pi$  indicating that the surface should be smooth along that boundary.**

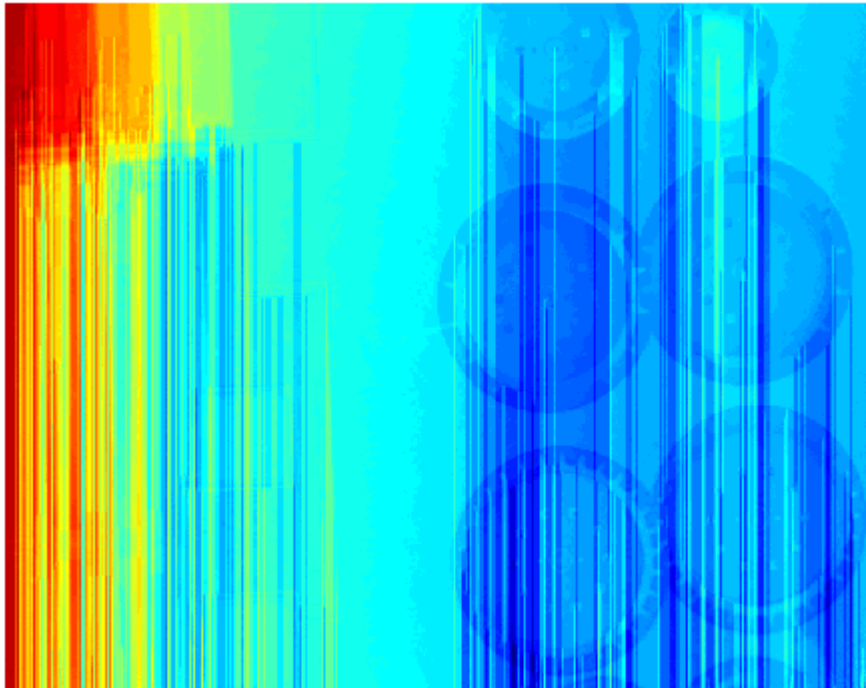


**Figure 18: (prior art) Unwrapping interferograms by sweeping and using best previous row match.**

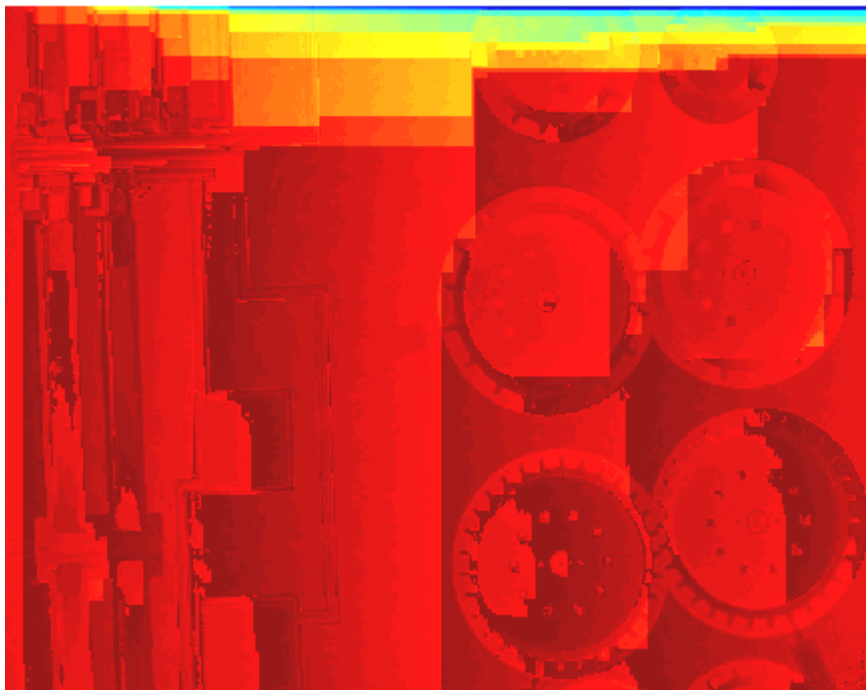


**Figure 19: (prior art) Unwrapping interferograms by sweeping and using the best of the previous column match and the previous row match.**

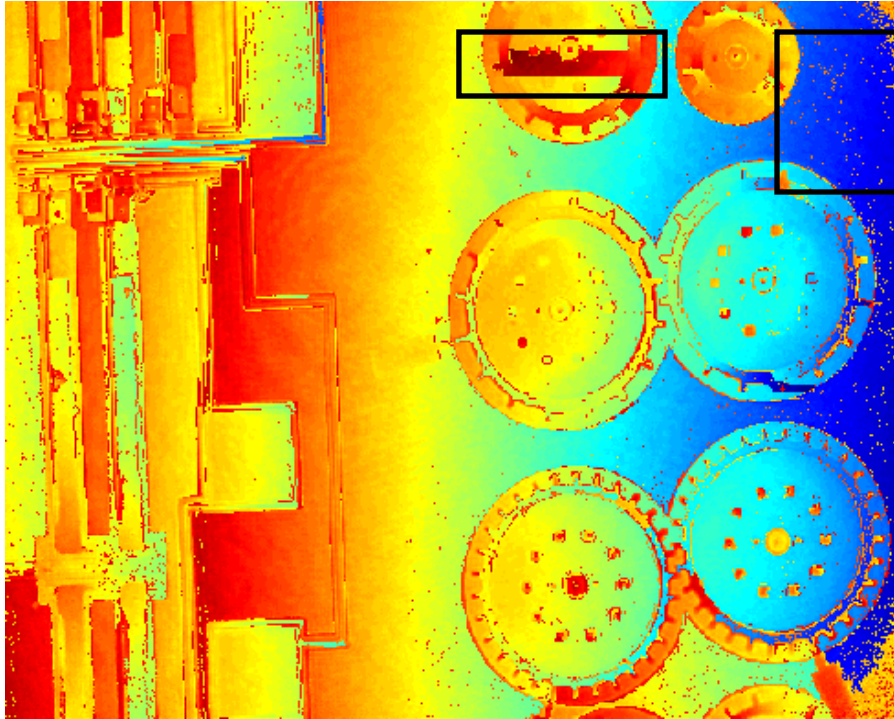


**Figure 20: (our work) Unwrapping interferograms using breadth-first search. The boxes illustrate slivers and pixilated noise.**

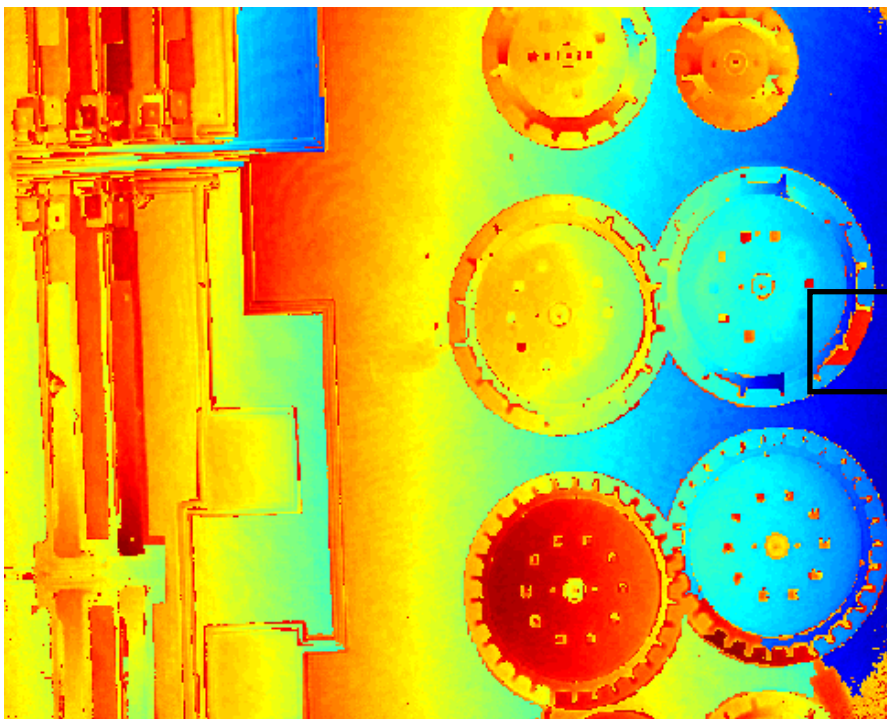


**Figure 21: (our work) Unwrapping interferograms using hierarchical merging. There are still slivers, but not as large.**

The next challenge in interferometry is time-resolving motion of the MEMS structures. This challenge is addressed in Chapter 6 but discussed briefly here. Previously, researchers have shown that it is possible to measure the resonant motion of MEMS structures stroboscopically. This method works by repeatedly pulsing a laser at precise phase offsets along an oscillating driving function. This technique works well on highly repeatable resonant motion ranging from 1 kHz to 100 kHz. For lower resonant frequencies, each laser pulse becomes spaced further and further apart, so the time integration over each frame becomes long enough for vibrational noise to blur the image. For higher resonant frequencies, more rapidly pulsing lasers and driving electronics are required.

Each resulting unwrapped pixel is a value modulo the wavelength of laser light used. To reconstruct the full image is somewhat difficult because it is hard to determine the stepsize of discontinuous jumps. Several techniques for unwrapping these pixels have been proposed including multigrid and FFT-based methods (Pritt 1996). However, the more sophisticated algorithms take minutes to complete unwrapping for a single phase map. We have found a good compromise between speed and accuracy of unwrapping is accomplished using a breadth-first search algorithm coupled with a priority queue for weighting the measurement quality of each pixel as well as connectedness.

For small vertical displacements and relatively smooth flat surfaces, it is easy to determine relative height changes. Because a majority of MEMS devices are made with flat surfaces and use relatively small actuation distances, interferometric methods will

continue to gain popularity and usefulness in MEMS metrology. Interferometry can be applied in two configurations: reflective, known as a Twyman-Green configuration (**Figure 14**) as well as transmissive, known as a Mach-Zehnder configuration (Malacara 1992). These two configurations allow the study of interfaces as well as flat surfaces allowing fast phase-shifting interferometry to find a growing use in microfluidic MEMS (Markov, et al. 2004) as well as biological applications (Choo, Kant, et al., MEMS-Based, Phase-Shifting Interferometer 2006).

### 3.4 Summary of Optical Metrology

The highlights of this chapter include a method to quickly match a microscope image of a device to its layout representation and then navigate to desired chip positions using an attached stage, a method to quickly unwrap phases in stroboscopic microscopic interferometry, and a method to perform dynamic deformation on the structure while matching this deformation to a simulation of the deformation. Our contributions to the area of optical metrology include the introduction of fast algorithms for locating structures on chip, teleoperating experiments, and monitoring dynamic deformation of structures. Such a system will help in teleoperating experiments for researchers especially when the instruments they need to use for the tests are in a remote location. We have also developed breadth-first search phase-unwrapping algorithms in phase-shifting interferometry for (>100Hz) realtime processing of interferometric data. Introduce new phase-unwrapping technique for reducing defects and improving accuracy of unwrapping.

## Chapter 4: Electrical Metrology Techniques

This chapter details the layout, circuits, and procedures for characterizing gap variation, effective Young's Modulus, and comb-drive forces using purely capacitive and voltage measurement techniques coupled with a device that we will call a *complementary comb-drive*. This device can be completely integrated and probed continuously with CMOS circuitry, requires only a single device layer and isolation layer to work in any process that supports the creation of comb-drives, fits in an area under 1 mm by 1.5 mm and produces characterizations that have a better resolution than optical methods. The motivation for the creation of such a device and methods are described in section 4.1. The components and theory of the characterization device are examined in section 4.2. The device configuration and measurement circuit are detailed in section 4.3. The measurement procedures are further explained in section 4.4. Section 4.5 reports the results for an SOI process. This chapter mainly is based on our publication (Garmire et al., MEMS Process Characterization with an on-Chip Device 2006). Details are also included from our patent application (Garmire et al., Integrated MEMS Metrology Device using Complementary Measuring Combs 2006).

### 4.1 Motivation

The main advantage of using *in situ* electrical metrology over optical metrology is the cost to do the metrology on arrays of devices. Electrically probing a structure requires only a few off-the-shelf components or easily integrated CMOS circuits. The probing can

be done on a large scale switching over arrays of metrology devices, and the metrology methods can be automated with the on-chip logic and circuitry without the requirement of alignment or cpu processing as is required in optical metrology.

Three standard approaches have been used in non-optical metrology for MEMS. First, researchers have used scanning electron microscopy (and other variants) which was perhaps the earliest method used for MEMS metrology and the most popular in MEMS publications (Novak 2005). A major limitation of scanning microscopy for determining overetch is the charging effect around the edges of silicon beams. This effect can limit the resolution of scanning electron microscopy to the resolution of optical microscopy. Second, researchers have used atomic force microscopy for determining small forces that are possible from MEMS actuators. Finally, researchers have also used nano-indentation techniques for determining Young's Modulus of various MEMS materials (Saha and Nix 2002). This method of determining Young's Modulus yields variable results and is difficult to calibrate (Clark, Electro Micro-Metrology 2005).

The expense of the testing setup is a major limitation of all of these techniques. Each device must be individually positioned and tested inside a complicated and expensive testing rig. Labor cost is required for the repositioning and retesting of each device and so it becomes infeasible to do cross-wafer and cross-chip testing. Ultimately a method is lacking for doing such detailed analysis of the MEMS process, but such a method is required if current MEMS manufacturing capabilities can meet the expectation.

A new methodology is needed that allows for the direct fabrication of a metrology device on the layers that need to be characterized. The device should be made sufficiently small so as not to consume valuable chip real-estate.

Two approaches have been considered: resistive and capacitive techniques. Resistive techniques require the fabrication of another layer in the MEMS process (Cao, et al. 2000) whereas capacitive information gives knowledge about gaps as well as deflection of beams. We decided to follow the capacitive measurement technique for this reason.

We report on the development of an on-chip micro-device for characterizing material, operational, and process properties, targeting specifically measurements of cut error, effective Young's Modulus, and comb-drive forces. These three properties are especially important because they can vary significantly between process runs as well as even within an individual wafer (Clark, Garmire, et al. 2004). For these reasons, it is worthwhile to design and integrate test structures to measure the three properties and to make the test structures small and to locate them close to the operating MEMS structures.

MEMS engineers use the above-mentioned three properties extensively to evaluate processed-part behaviors such as resonant frequencies, tolerances, and deformation as well as many other important properties (Clark, Electro Micro-Metrology 2005). Therefore, accurately characterizing MEMS process properties is important for understanding device behavior and calibrating system performance (Gupta 2000).

One of the main impediments to commercializing MEMS devices is fluctuations in their performance due to the variations caused by the manufacturing of the wafer material, fabrication processing, and post-packaging of the devices (Tadigadapa and Najafi 2003). An on-chip characterization device not requiring any external test rigs can help expose sources of process variations between wafers and even within individual wafers. This may result in a standard method to improve process quality control.

In addition, understanding force and motion characteristics of devices is useful for many different measurement applications. In biology and biomedical research, stimulation of cells using MEMS devices can be aided by understanding the precise forces and motions exerted on the cell. Similarly, precise positioning allows for the accurate contact of microelectrodes in brain tissue (Muthuswamy, et al. 2005). Also, if a material is deposited on a calibrated cantilever structure, one can determine the stiffness and thickness of the deposited material, thus providing a sensor for that material. Moreover, having a localized device for measuring these properties may aid in calibrating and tuning MEMS devices during operation in the field.

Oftentimes process parameters are measured using expensive off-chip equipment. The three NIST standards (ASTM E 2244-6) that exist for MEMS use interferometry to determine beam length, strain, and strain gradient (Marshall 2001). For measuring Young's Modulus, nanoindentation tools are used for applying very precise loads and accurately measuring displacement (Li, et al. 2003). For measuring in-plane cut error, an SEM image is often used, and for measuring layer thickness, ellipsometry is typically

used (Gupta 2000). While these approaches can be effective to some degree, they may be difficult to implement for large numbers of chips.

A few on-chip approaches exist for measurement of MEMS material properties. One approach uses out-of-plane beam bending (Chan, Garikipati and Dutton 1999). However, it is difficult to characterize fringing fields which change as the plate actuates. The resolution is also limited by the pull-in distance of the cantilevers. Other approaches use large arrays of devices and destructive testing (Guckel 1992) (Osterberg and Senturia 1997). A drawback to these approaches is that a large area of the chip must be used for property measurements, and the devices cannot be reused after testing.

## 4.2 Capacitance Sensing Theory

We show how to measure the comb-drive force ( $F$ ), cut error ( $e$ ), and then effective Young's Modulus ( $E$ ) using only capacitance and voltage measurements. We assume the layer thickness ( $h$ ) is known or measured using other in-situ devices (Chan, Garikipati and Dutton 1999).

An advantageous feature of a comb-drive (or any tunable capacitor) is that the force exerted on its moving surface in the direction of motion ( $F$ ) can be computed directly from the potential ( $V$ ) used to achieve the actuation, the change in the capacitance ( $dC$ ), and the distance of the motion ( $x$ ) (Eq. 12) (Johnson and Warne 1995). Use of Eq. 12 requires the accurate measurement of  $x$ , which we achieve using the concept of a complementary comb-drive.

$$F = \frac{V^2 dC}{2x} \quad \text{Eq. 12}$$

To determine the cut error ( $e$ ), the comb-drive force is related to the number of fingers ( $N$ ) of one side of the comb-drive (the side with the fewer number of comb fingers), finger gap ( $g$ ) (for simplicity, let  $g_e = g - e$ ), finger width ( $w$ ), layer thickness ( $h$ ), and fringing field factor ( $\alpha$ ) as shown in Eq. 13 (see **Figure 22**).  $\alpha$  may be calculated analytically from the device geometry (Johnson and Warne 1995).

$$F = \frac{\alpha N \epsilon_0 \epsilon_{\text{air}} h V^2}{g_e} \quad \text{Eq. 13}$$

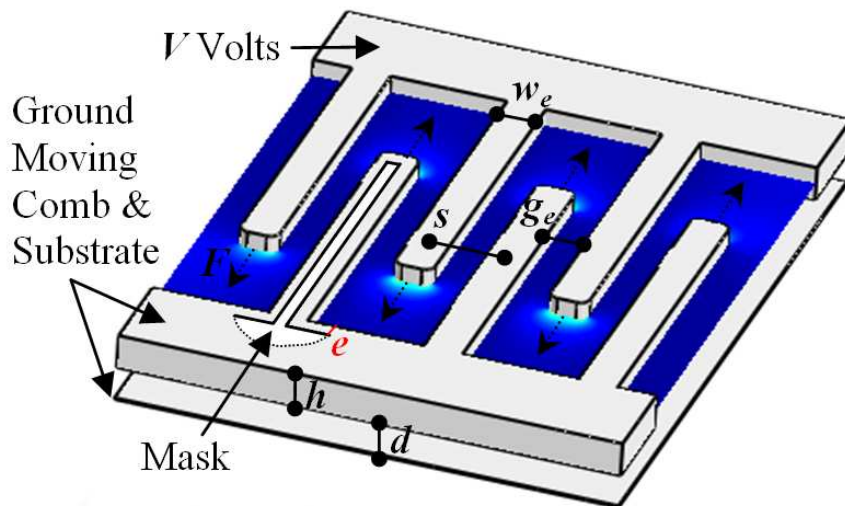


**Figure 22: Slice of a comb-drive with the  $y$ -component of the electric field superimposed**

Assuming  $\alpha$  and  $e$  remain nearly constant, we can use two different comb-drive sets with varying layout gaps,  $g_1$  and  $g_2$ , and number of fingers,  $N_1$  and  $N_2$ . Using Eq. 14, we find the voltages,  $V_1$  and  $V_2$ , for which their exerted forces are the same. The point at which the exerted forces are the same are precisely when the suspension has deflected by the

same amount because the same suspension is used in both cases. Finally,  $e$  is computed in Eq. 14 by equating the two expressions for  $F$  given by Eq. 13.

$$e = \frac{N_1 V_1^2 g_2 - N_2 V_2^2 g_1}{N_2 V_2^2 - N_1 V_1^2} \quad \text{Eq. 14}$$

We choose a guided parallel cantilever structure (see **Figure 23**) for the suspension. Knowledge of the suspension allows us to extract the effective Young's Modulus ( $E$ ) of the material. For a parallel guided suspension, the effective Young's Modulus ( $E$ ) can be computed from  $F$ ,  $e$ ,  $x$ , the layer thickness ( $h$ ), and cantilever beam layout width ( $w$ ,  $w_e=w+e$ ) and length ( $l$ ,  $l_e=l+e$ ) using Eq. 15. We assume nearly vertical sidewalls.

$$E = \frac{F(l_e)^3}{2xh(w_e)^3} \quad \text{Eq. 15}$$

In (Clark, Garmire, et al. 2004), we determined cut error by creating multiple suspensions with varying suspension beam widths and solving a cubic equation. Here, we reduce space consumption and make the process simpler by using multiple comb-drive sets with different finger gaps and widths on the same suspension. This approach also permits the study of the variation of cut error for differing layout widths and gaps that may result from the type of process used.

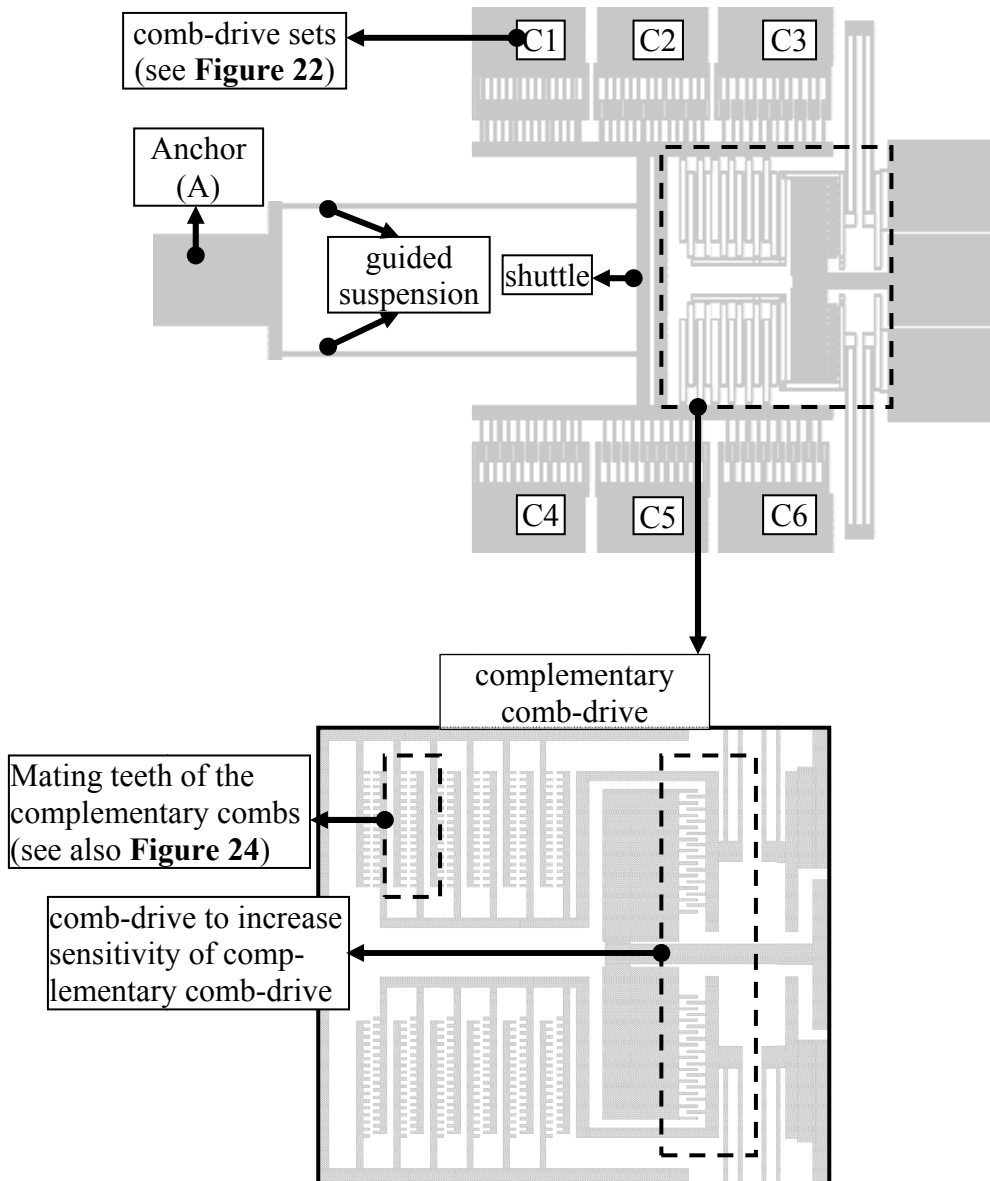


**Figure 23: Metrology device schematic (top) and blow-up of the complementary comb-drive (bottom)**

The main challenge is to accurately determine the lateral distance of motion ( $|x|$  in Eq. 12) of the shuttle when a potential is applied to the comb-drive sets (see **Figure 23**). To overcome this challenge, we introduce a complementary comb-drive, similar to an

engineering Vernier scale, except that in our complementary comb-drive, the ends of a fixed set of comb teeth are spaced equilaterally from the ends of a mating moving set of comb teeth that translates parallel to the fixed comb (see **Figure 23**). The capacitance between the fixed and moving combs in the measuring-comb structure varies as the moving-comb fingers are successively positioned in-and-out of alignment; correcting for global effects, it is at a maximum when the fingers are in registration and a minimum when the fingers of one comb align with spaces in the other. The maxima and minima are typically detectable even for very small signals and motions. Furthermore, spacings between the maxima and minima are not affected by variations in structural cut rates. Moreover, a spring suspension allows the measuring combs to be pushed closer to each other thereby increasing the capacitance sensitivity to lateral motion and is used for obtaining a difference of capacitance change that eliminates global lateral motion effects. There are two such complementary comb structures on the two sides of the shuttle, one initially completely out of alignment and the other in alignment, to allow for differential capacitance measurements (**Figure 24**). Differential capacitance measurements are preferred to single-sided capacitance measurements as they eliminate noise in the sensing circuitry.

We first examine the effectiveness of this approach in measuring lateral motion by simulating a few comb teeth to obtain an idea of the sensitivity of the device and the analysis necessary to determine the displacement (**Figure 25**). The simulations are carried out in COMSOL Multiphysics (<http://www.comsol.com/>) on the electrostatics problem using Lagrange quadratic elements and solving for the electric potential at each

element. Then the capacitance is determined by integrating the electric energy density to determine the electric energy,  $U$ , and using the equation for the energy stored in a capacitor:  $C = \frac{2U}{V^2}$ . Approximately, the differential capacitance scales proportionally with the layer thickness of the material and the number of complementary comb teeth, and inversely with the square of the separation distance.

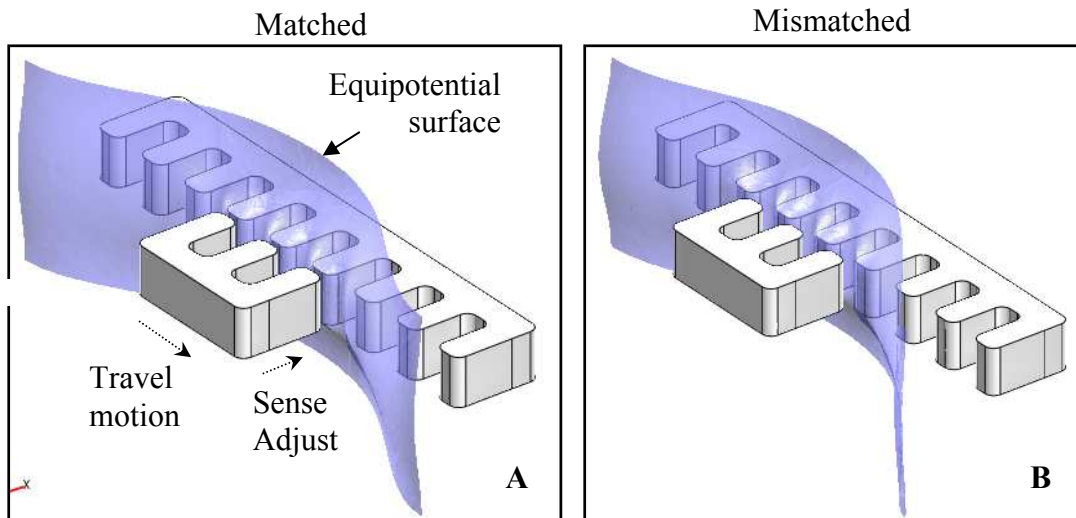


**Figure 24: Simulation of complementary comb-drive – an equipotential surface is superimposed. Capacitances of A and B are subtracted over the motion of travel. Note that although the equipotential surfaces are similar, in A the electric field is larger as the two mating combs are closer to each other than in B.**

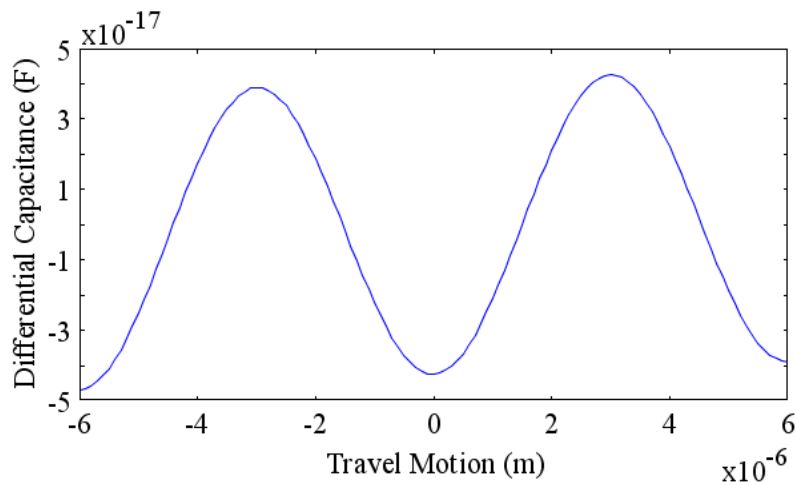


**Figure 25: Simulated results for complementary comb-drive – capacitance of B minus capacitance of A (blue) ( $h = 5 \mu\text{m}$ ,  $g = w = 3 \mu\text{m}$ , separation = 500 nm).**

The important result is that these peaks are consistently spaced a photolithographically-defined distance apart regardless of whether there is overetch, sidewall-angle variation, and even footing (Wang, et al. 2007) or anisotropic effects. Therefore, we can use the measured capacitance to accurately measure  $|x|$  in Eq. 12 regardless of the fabrication process.

We use a differential amplifier in a charge-integrator configuration to measure the capacitance changes of the actuated device (**Figure 26**). This circuit is capable of measuring very small (below 1 attofarad) capacitive differences (Boser 1997). We calibrate this device by measuring a change of RMS voltage through the circuit for fixed changes of capacitance and comparing those values against an HP4284A<sup>2</sup> LCR measurement of those same capacitances. For obtaining the experimental data, the output voltages to drive the device are controlled by an NI-PCI-6733<sup>3</sup> board and the differential capacitance signal is sensed by an NI-PCI-MIO-E<sup>4</sup> board.

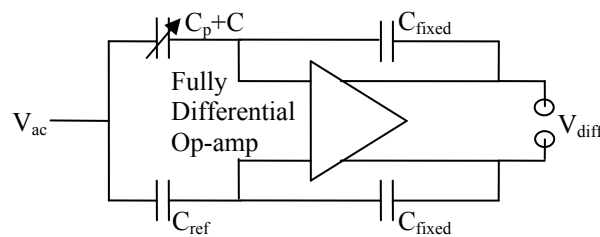


**Figure 26: Simplified view of the measurement circuit**

### 4.3 Capacitance Sensing Procedures and Details

<sup>2</sup> <http://www.agilent.com>

<sup>3</sup> <http://www.ni.com>

<sup>4</sup> <http://www.ni.com>

Our method is superior to other methods which rely on resonant motion of the MEMS device due to the long electronic integration times that can be used for fixed deflection measurements and the decoupling from damping that is a large source of error due to its strong temperature dependence. The long integration times also helps to limit the effects of drift in the measurement.

The design is shown in **Figure 27** which is an abstraction of the design shown in **Figure 23** (each letter corresponds to a labeled part in the diagram):

- A. an anchored guided suspension with cantilever width,  $cw$ , and cantilever length,  $cl$ ,
- B. a shuttle that joins the suspension and the driving and sensing apparatus,
- C. a set of driving and sensing comb-drives,
- D. a complementary comb-drive to sense displacement of the shuttle, and
- E. an optional gap-closing sense array for further assessing cut-error.



In the design of the shuttle (B), it should be kept as stiff as possible while still being releasable. The shuttle can be made a stiff beam but yet can be released from the substrate by using etch holes.

For improved sensitivity and simplicity, driving and sensing comb-drives (C) should be matched on both sides of the shuttle. To measure gap variation for different geometries, it may be more economical to use differing comb-drive dimensions on either side of the comb-drives.

The design of the complementary comb-drive (D) is shown in **Figure 28** (see corresponding letters on the diagram):

- F. one set of matched teeth,
- G. one set of mismatched teeth,
- H. suspensions that allow the teeth sets to be moved towards each other, and
- I. comb-drives to actuate the suspensions.

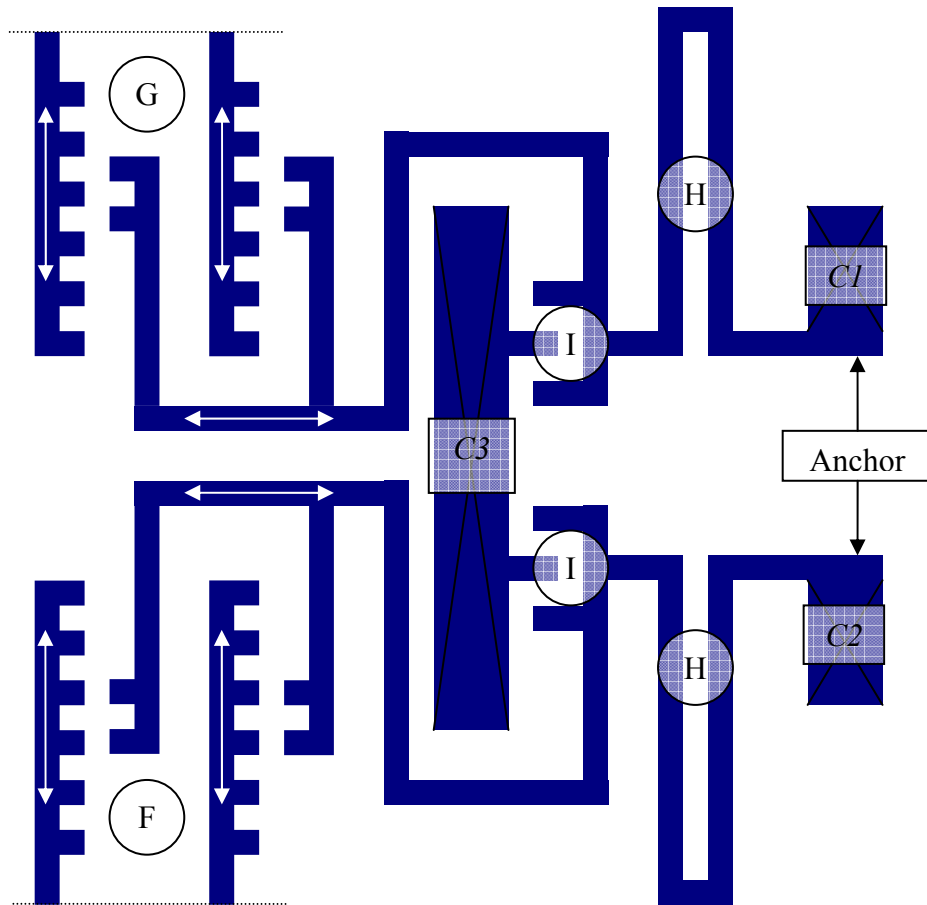


**Figure 28: Complementary comb-drive schematic (abstraction of the schematic shown at the bottom of Figure 23) (this figure is a blow-up of the orange rectangle surrounding D in Figure 27).**

The set of matched teeth (G) and mismatched teeth (F) should have equal spacing with one another (each tooth should be separated by the same distance,  $x$ , from Eq. 12). Bias is applied to C3 to bring the complementary comb-drives (F and G) closer together. C3 may be joined (as shown above) or separated to allow for independent actuation of F and G depending on whether more simplicity or flexibility is needed.

In an alternative configuration, four teeth sets may be used, two sets shifted by a quarter of the distance between adjacent comb teeth as shown in **Figure 29**. The sinusoidal-like capacitance function is then shifted by 90 degrees, and a Hariharan-type algorithm (Hart,

et al. 2000) may be applied to find the displacement. Note that this procedure may have slight phase errors due to the asymmetry of quarter shifted comb-teeth and also the size requirements are increased.

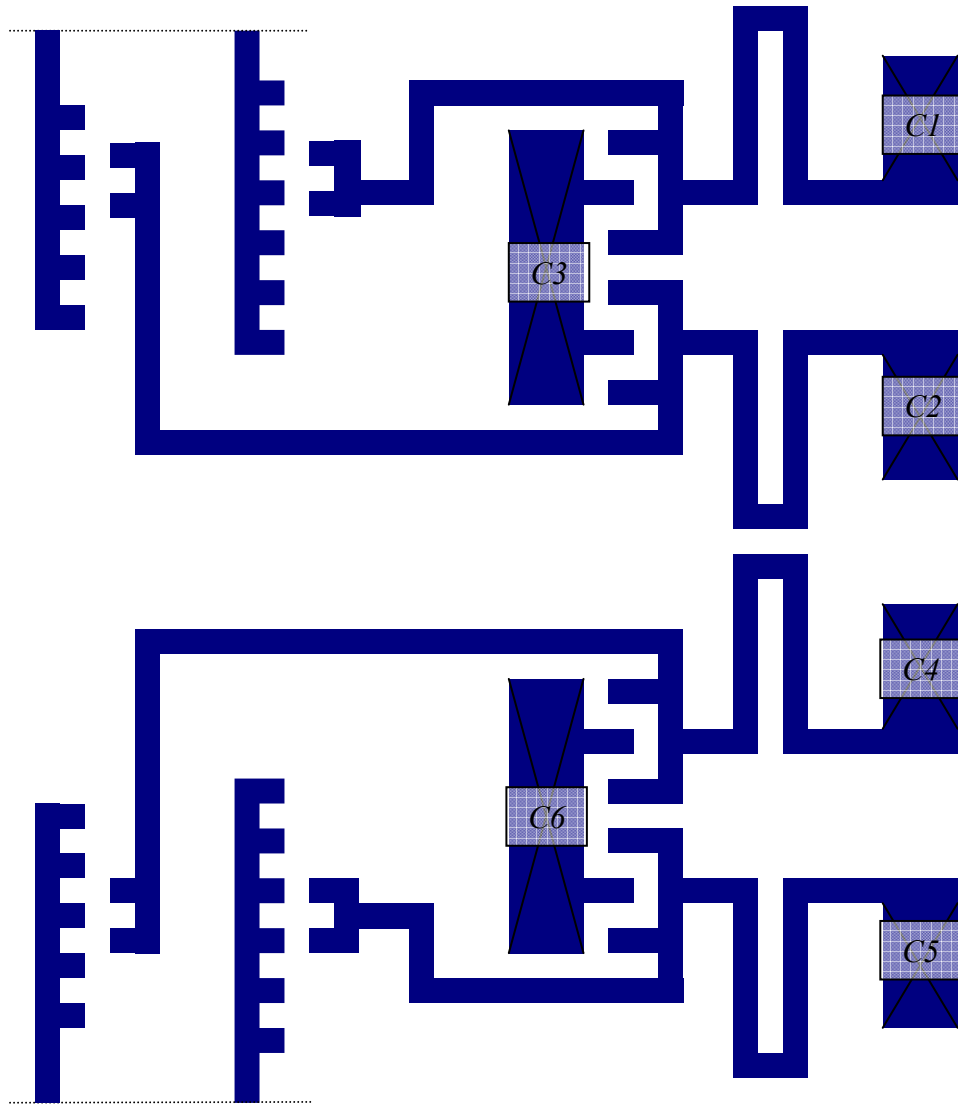


**Figure 29: Complementary comb-drive schematic (alternative)**

Sensing the change in capacitance across a parallel gap as it is closed can be more sensitive for small motions than sensing the capacitance change across a comb-drive as it is closed. An optional gap-closing sense array may be used to further refine the

measurements of cut-error and also measure layer thickness (**Figure 30**). Each gap-closing sensor consists of two fixed gaps, each defined by two parallel beams. The second set of beams should be offset by a distance,  $dw$ .

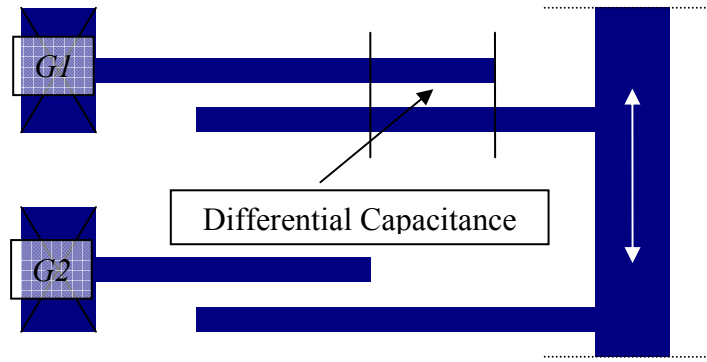


**Figure 30: Gap-closing sense schematic**

$G1$  and  $G2$  must be tied to  $A1$  if gap-closing sensing is not used (to avoid charging effects). In general,  $A1$ 's DC offset (if used) should also be applied to  $G1$  and  $G2$ .

In a balanced configuration, the drive and sense comb-drives each consist of comb-drives on both sides of a shuttle (A) one of which will be driven while the differential capacitance is sensed between them. The comb-drive sets will each have different finger widths,  $w$ , and gap spacings,  $g$ , between fingers. The finger overlap should be kept small to reduce levitation effects. An optional set of comb-drives (B) on the opposite side of the shuttle with fewer comb-fingers but more overlap may be used to reduce tilt. (**Figure 31**)

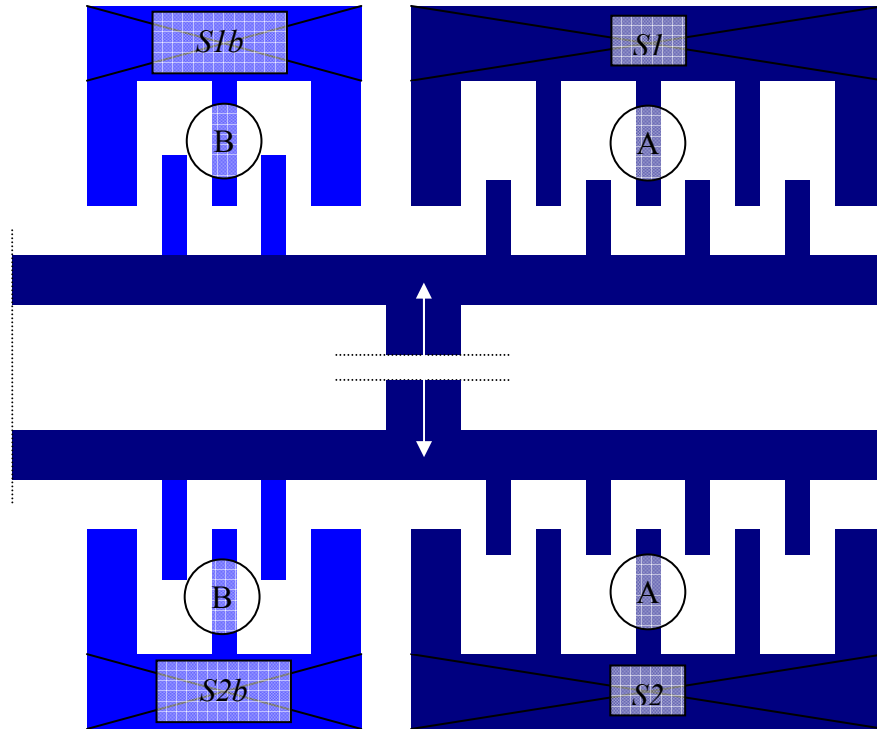


**Figure 31: Drive / Sense comb-drive schematic**

In order for the characterization procedures to be applied in practice, sensitive differential-capacitance measurements (with a resolution around or below 10 aF) need to be made while a voltage sweep is supplied to the driving comb-set. There are two approaches to measuring the differential capacitance – to use a charge-integrator scheme or to use a differentiation scheme; both of these methods can be used by simply interchanging capacitors and resistors. In **Figure 32**, resistor values are denoted with an “R”. Capacitor values are denoted with a “C”.

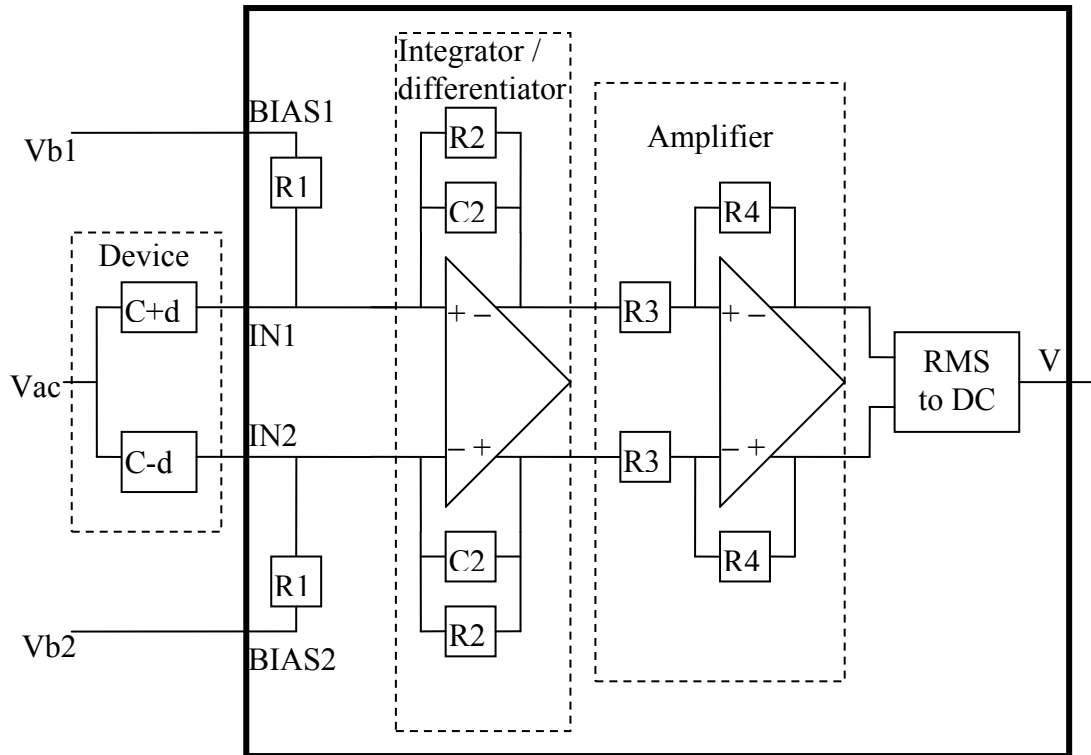


**Figure 32: Differential sense circuit schematic (does not include capacitive bypassing of the power supply)**

The signal from the DC biasing ( $V_{b1}$  and  $V_{b2}$ ) is low-pass filtered through resistor  $R1$ , and capacitor  $C1$  (large). If an integrator is desired,  $C2$  is set to a small capacitive value and  $R2$  is set to a large resistive value. The gain ( $V/|V_{ac}|$ ) is roughly  $2*d/C2$ , where  $2d$  is the difference in capacitance. If a differentiator is desired,  $C2$  is not used, and  $R2$  is set to around a 100Kohm level. The gain ( $V/|V_{ac}|$ ) is roughly  $2*d*R2*\omega$  (where  $\omega$  is the frequency of  $V_{ac}$ ). The second stage amplifier can further be used to amplify the signal. The gain is roughly  $R4/R3$ . Finally, the alternating signal can be converted to a DC signal through an RMS to DC converter.

The final setup, using the terminal notation from the previous figures, is illustrated in **Figure 33**. Assume that terminals not shown are grounded.  $V_{ac}$  is an alternating signal ( $>200\text{kHz}$ ) applied to the suspension and  $V_{dc}$  is a bias applied to the suspension (and other components) to correct for the levitation effect.

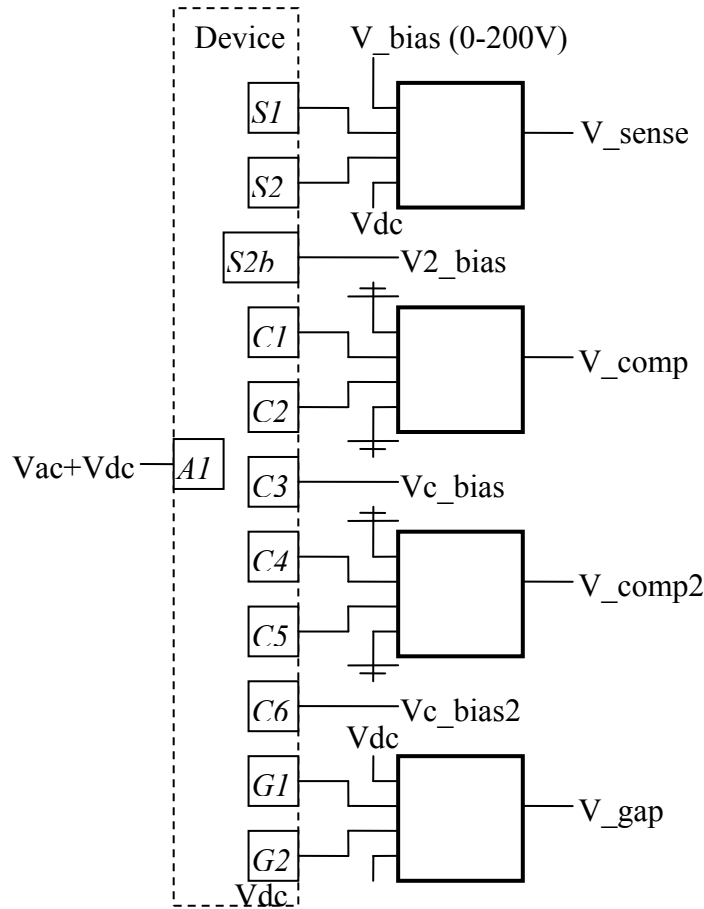


**Figure 33: Overall circuit schematic with device terminals**

### 4.3.1 Measurements

First, we discuss the main approach and then we discuss variations to use to counteract the levitation effect (Tang, Lim and Howe 1992) that we will explain, refine the

complementary comb-drive measurements, and refine the measurement of cut error. I show how to measure the comb-drive force  $F$ , cut error  $e$ , and then effective Young's Modulus  $E$  using only capacitance and voltage measurements and assuming the layer thickness  $h$  is known.

The steps to determine the parameters are given as follows. First, we calibrate the differential sense circuit shown in Figure 32 so that the differential capacitance,  $d$ , is known from a measurement of  $V$  (note that there is a factor of 2). An LCR meter (an instrument that measures inductance, capacitance, and resistance) such as an HP4824A can be used for this purpose. Next, we move the suspension sweeping  $V_{bias}$  and measuring  $V_{comp}$  as well as  $V_{sense}$ . We find the  $V_{bias}$  and  $V_{sense}$  values associated with the first peak of  $V_{comp}$  (either a max or min value) (it is most accurate to do this measurement by curve-fitting). Corrections may have to be made if the output is shifted (due to imperfectly matched capacitances). The values for  $V_{comp}$  may be shifted such that the max and min are equidistant from the origin. We adjust  $V_{c\_bias}$  until the location of the maxima and minima are known to the desired accuracy. Then we can move the shuttle a distance of half the distance ( $x$ ) between successive complementary-comb teeth. The change of capacitance ( $dC$ ) can then be determined from the calibration data and  $V_{sense}$ . The force ( $F$ ) exerted on the suspension is then  $V_{bias}^2 dC / (2 * x)$ . A model of the comb-drive force ( $F$ ) allows the determination of the cut error ( $e$ ) from two different comb-drive sets.  $F$  is related to the number of fingers ( $N$ ) of the comb-drive side with fewer comb fingers, finger gap ( $g$ ) (for simplicity, let  $g_e = g - e$ ), finger width ( $w$ ), layer thickness ( $h$ ), and fringing field factor ( $\alpha$ ) as  $F = \alpha N \epsilon_0 \epsilon_{air} h V^2 / g_e$ . Assuming  $\alpha$  and  $e$

remain nearly constant, we can use two different comb-drive sets with varying layout gaps,  $g_1$  and  $g_2$ , and number of fingers,  $N_1$  and  $N_2$ . Using step B, we find the  $V\_bias$  bias voltages,  $V_1$  and  $V_2$ , for the two sets that generate the same force (same displacement).

Cut error is computed as  $e = \frac{N_1 V_1^2 g_2 - N_2 V_2^2 g_1}{N_2 V_2^2 - N_1 V_1^2}$  (Eq. 13). Finally, the effective Young's

Modulus may be computed as  $E = \frac{F(1+e)^3}{2xh(w-e)^3}$  (Eq. 14) where  $l$  is the cantilever length, and

$w$  is the cantilever width.

If the complementary teeth are tightly packed in the configuration in **Figure 28**, then set  $Vc\_bias = 0$  and measure the complementary-comb signal,  $V\_comp0$ , as  $V\_bias$  is swept. As  $Vc\_bias$  is adjusted, subtract the sweep data from the original sweep (this subtraction will remove global effects),  $(V\_comp - V\_comp0)$ .

To measure the actual Young's Modulus, two separate suspensions are needed, one with a differing cantilever width. The stiffness due to beam-anchor compliance and webbing effects can then be determined using the fact that the total stiffness is the sum of the web compliance stiffness and the stiffness of the suspension.

#### 4.3.2. Levitation Effect

To correct for the levitation effect (Tang, Lim and Howe 1992), the optional comb-sets (B in **Figure 31**) must be used. The levitation effect is a vertical force experienced by both sides of a comb-drive (as a potential is applied across them) due to the ground plane. The levitation force pushes the two sides of the comb-drive away from the ground plane.

For each biasing voltage,  $V_{bias}$ , the following steps should be taken to remove the levitation effect.

- A. Apply bias to  $V2_{bias}$  until  $|V_{comp}|$  is maximized.
- B. Apply bias to  $Vdc$  until  $|V_{comp}|$  is maximized.

### 4.3.3. Cut-error Refinement

The cut error for differing geometries may be more accurately measured using a gap-closing actuator shown in **Figure 30** (definitions from **Figure 33** still apply).

- A. As  $V_{bias}$  is swept, measure  $V_{gap}$ .
- B. Use the calibration data to convert  $V_{gap}$  to capacitance,  $C_{gap}$ .
- C. Use the complementary-comb data to convert  $V_{bias}$  to the translation,  $x$ .
- D. Fit the data to  $C_{gap} = \alpha \epsilon_0 \epsilon_{air} A / (g_{model} - x)$ . ( $\alpha \epsilon_0 \epsilon_{air} A$  is constant)
- E. Cut error is then  $g_{model} - g$ .
- F. A short set (3-5 microns in length) of gap-closing sensors may be used as gap stops to allow the determination of the sidewall angle. The cut-error determined in step E is near the midpoint of the layer. Actuate the shuttle until the gap is reached. Measure the displacement,  $g_{bottom}$ , using the  $V_{sense}$  data. The sidewall angle is approximately  $(g_{bottom} - g_{model}) / (h/2)$ .
- G. Similarly, as the gap is closed, the fringing-field effect is reduced. At the point where the fringing-field effect is sufficiently reduced, the layer thickness,  $h$ , may be measured by finding the area  $A$  (from step D) and dividing by the layout protruding length (it is not affected by cut error).

If the alternative approach shown in **Figure 29** is taken, then refinements can be made to the comb-drive sensing device.  $V_{comp}$  and  $V_{comp2}$  will be periodic functions (of displacement which is proportional to  $V_{bias}^2$ ). They will also be 90 degrees out of phase with one another. The minima and maxima can be found when the function  $\text{atan}(V_{comp2}/V_{comp})$  crosses multiples of  $\pi$ . Near these regions, the data can be linearly fit to determine this crossing value precisely. Note that the atan function must be unwrapped – when values cross  $\pi$ , they jump to  $-\pi$ , so  $2\pi$  must be added to the results to make them continuous.

## 4.4 Results

We have fabricated our device in a silicon-SOI process. An SEM shows the fabricated device in an SOI process (**Figure 34**). As we actuate comb-drive set 1, we measure the differential capacitance through the complementary comb-drive. We then shorten the separation distance between the matched and unmatched combs and remeasure the differential capacitance. We then subtract these measurements to remove global effects and plot the result (**Figure 35**). The standard deviation of the peak positions are 6 angstroms.

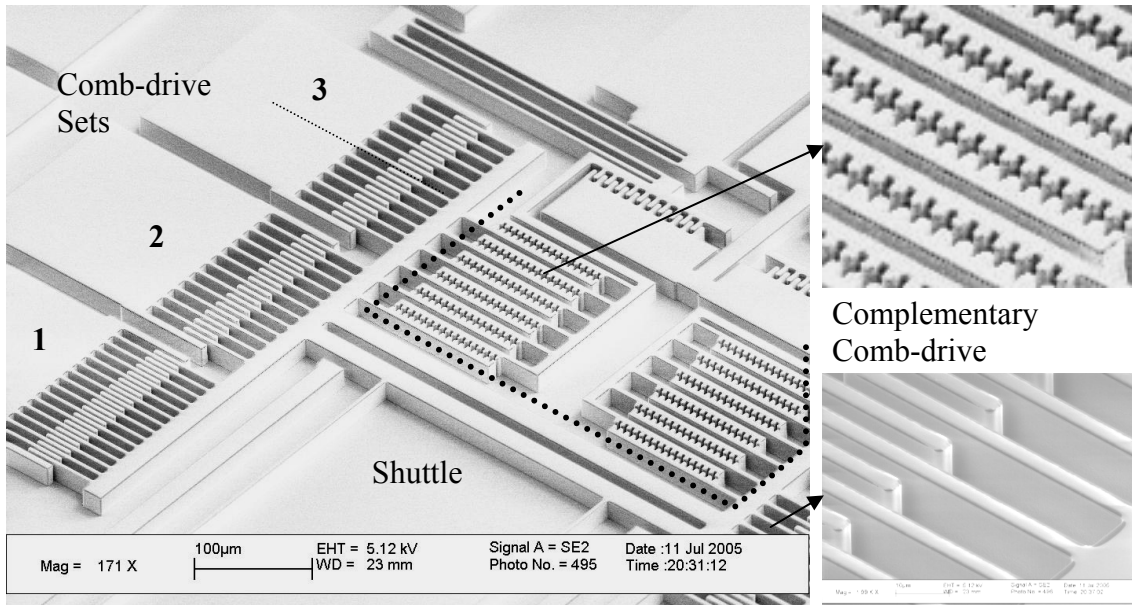


**Figure 34: SEM of fabricated device (left) with blow-up of complementary combs (top right) and fingers of a comb-drive set (bottom right)**

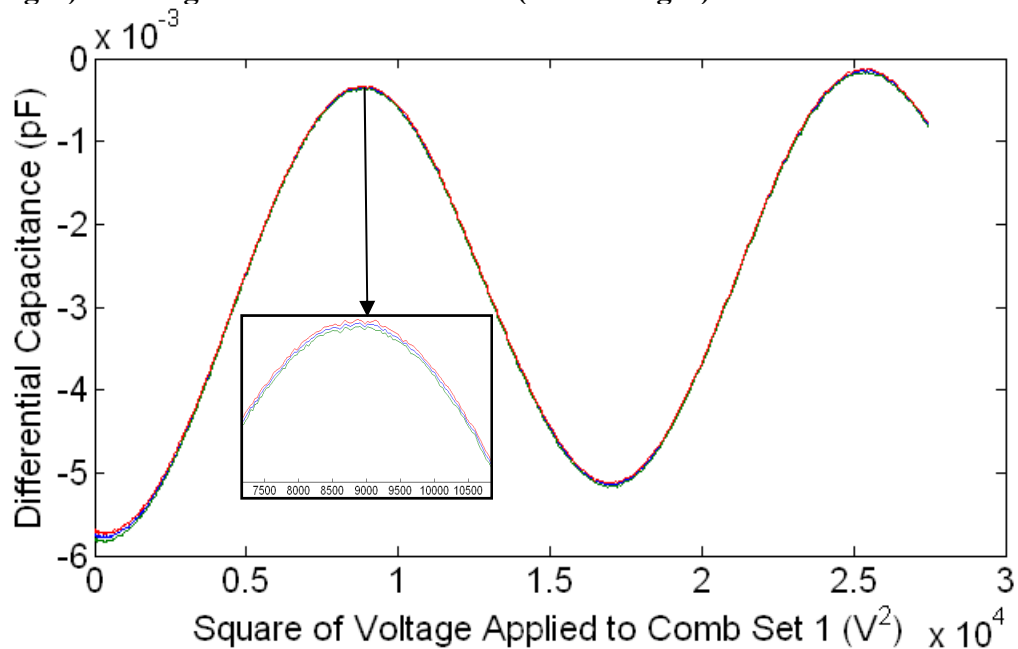


**Figure 35: Differential capacitance measurement from an SOI complementary comb-drive as comb-drive set 1 is actuated with a voltage. The 95% confidence interval is shown in the inset (red and green).**

Following our approach, we obtain measurements for the desired quantities (Table 1) – mean cut error  $e$ , optical verification of  $e$  (reported in  $\mu\text{m}$ ), effective Young’s Modulus  $E$ , and the mean fringing field factor  $\alpha$  as a representation of the force (Eq. 17).

### Results obtained for an SOI process

	$e$ ( $\mu\text{m}$ )	Optical $e$ ( $\mu\text{m}$ )	E(GPa)	Mean $\alpha$
SOI 1 <sup>5</sup>	0.16 $\pm$ 0.05	0.1 $\pm$ 0.1	156 $\pm$ 4GPa	1.39 $\pm$ 0.06

These measured values for Young's Modulus compare favorably with nanoindentation results for measuring the Young's Modulus of Silicon. The published data are variable averaging between 150 and 160 GPa (Clark, Electro Micro-Metrology 2005). Validating the gap variation results with another method is difficult due to the limitation of optical and SEM techniques (Gupta 2000). Our results agree with the optical measurement; however, it was found that an SEM measurement will be inaccurate due to curvature and roughness of the sidewalls. Even if cleaving a beam is used to obtain a better view of the profile, the cleave angle cannot be accurately controlled. Interferometric methods were also found to be inaccurate in determining gap variation. The main reason for this difficulty with interferometric methods is that gap variations are larger than half of a wavelength of typical visible laser light so it is impossible to determine the actual step height between the two surfaces. Therefore, of the inexpensive techniques, our electrical metrology method compares favorably with optical metrology methods.

## 4.5 Conclusions

On-chip electrical metrology holds the promise of providing MEMS with a low-cost solution to process characterization and robust control in the face of process variation and environmental changes. A key challenge has been to mitigate process variation in the

---

<sup>5</sup> H. Choo ( $h = 50 \mu\text{m}$ ,  $g_1 = 3 \mu\text{m}$ ,  $g_2 = 3.5 \mu\text{m}$ )

measurement of critical parameters like gap variation and Young's Modulus and to do all of these mechanical measurements with electrical signals. Our complementary comb-drive provides the first chance to meet these demands by creating a method that allows a photolithographically defined distance of travel to be measured accurately with purely capacitive measurements and voltage control regardless of most process variations. We have fabricated and tested this device and method in an SOI process, and it agrees with optical metrology methods for gap variation and nanoindentation results for Young's Modulus determination of bulk Silicon.

## Chapter 5: Reliable Out-of-plane Actuation and Sensing

This chapter introduces a novel method for creating vertically offset comb-drives in a single sequence of CMOS-compatible processes whereas before the creation of these comb-drives require a labor-intensive wafer-alignment step. Section 5.1 first discusses the current state-of-the-art for out-of-plane actuators and sensors and why there is a need for this research. Section 5.2 discusses the theory of electrostatically actuated and sensed vertically offset comb-drives. Section 5.3 details the fabrication process steps. Section 5.4 then explores the space of applications enabled by this process development including novel inventions for electrostatically deformed parabolic mirrors and torsional twist-up structures that theoretically extend the vertical travel of out-of-plane actuators while still providing the same force continuously over the motion of travel. Finally, Section 5.5 summarizes the work. This chapter is based in part on our process patent, (Choo et al., CMOS-Compatible High-Performance Microscanners, Including Structures, High-Yield Simplified Fabrication Methods and Applications 2005).

### 5.1 Motivation for Vertically Offset Comb-Drives

We have developed a process for building out-of-plane actuating and sensing devices by creating one-sided vertically offset combs that are completely self-aligned, or, in other words, aligned simply by the mask definition of the photolithography. The motivation behind building these devices is that out-of-plane actuators have been traditionally limited in their range of operation by the use of gap-closing actuation or the use of the

levitation effect. The levitation effect can only supply a small amount of force for the out-of-plane actuation (Tang, Lim and Howe, *Electrostatic Comb Drive Levitation and Control Method* 1992). Gap-closing actuation schemes provide much more force, but are limited in travel distance (Lu and Fedder 2004). Others have used bimorph layers to achieve the same effect but these devices generally suffer from unpredictable behavior and hysteresis (Jain, et al. 2005). Another approach described earlier to achieve vertical actuation for microscanners has been the use of a two-wafer process, whereby comb-drives are etched in each wafer separately and then the wafers are aligned to a very high accuracy to create offset comb structures (Ko, et al. January 2005).

In response to these difficulties, we have developed a process that can create vertically offset combs through purely CMOS-compatible steps and without any wafer alignment. This process allows for reducing the gap spacing, and increasing the overall force and sensing capability of vertical offset combs (see Section 5.2). We discuss the dynamics, processing, and applications of such actuators and sensor. Then, we explore the applications that this type of inexpensive process provides including a staged twist-up structure that extends the controllable travel of out-of-plane actuation and a deformable parabolic mirror that can be used as a focusing element for lasers and adaptive-optics systems.

Prior art, details and advantages of our process, and devices enabled by our process for optical components are further explained and examined in the PhD thesis (Choo 2007) and review article (Choo and Muller 2007).

## 5.2 Dynamics of Vertically Offset Comb-Drives

Vertically offset combs are illustrated in **Figure 36**. The vertical force density exerted from a change in potential between the offset comb and the unoffset combs is given by Eq. 16. For example, 2 micron widths and gaps with a 5 volt CMOS-compatible supply would yield a pressure of 13.75 Pa. For comparison, a gap-closing actuator with a 2 micron gap would yield an out-of-plane pressure of 27.66 Pa, only about twice the out-of-plane force but sacrificing linearity and limiting the stable travel of the driven structure to 1/3<sup>rd</sup> the gap unless more complicated circuitry is employed (Hung and Senturia 1999). The capacitance change per unit area for a small displacement,  $x$ , is shown in Eq. 17. An amazing result of this computation is that for a 100 micron by 100 micron vertically offset comb-drive array, it is possible to electrostatically sense the translation of the combs to a resolution of 0.1 nm if the differential capacitance measurement is capable of 1 aF resolution which is possible (Boser 1997).

$$\frac{F}{\text{Area}} = \frac{\epsilon_0 \epsilon_{\text{air}}}{2g_{\text{finger}}(w_{\text{finger}} + g_{\text{finger}})} V^2, \quad \text{Eq. 16}$$

$$\frac{\Delta C}{\text{Area}} = \frac{\epsilon_0 \epsilon_{\text{air}} x}{g_{\text{finger}}(w_{\text{finger}} + g_{\text{finger}})}, \quad \text{Eq. 17}$$

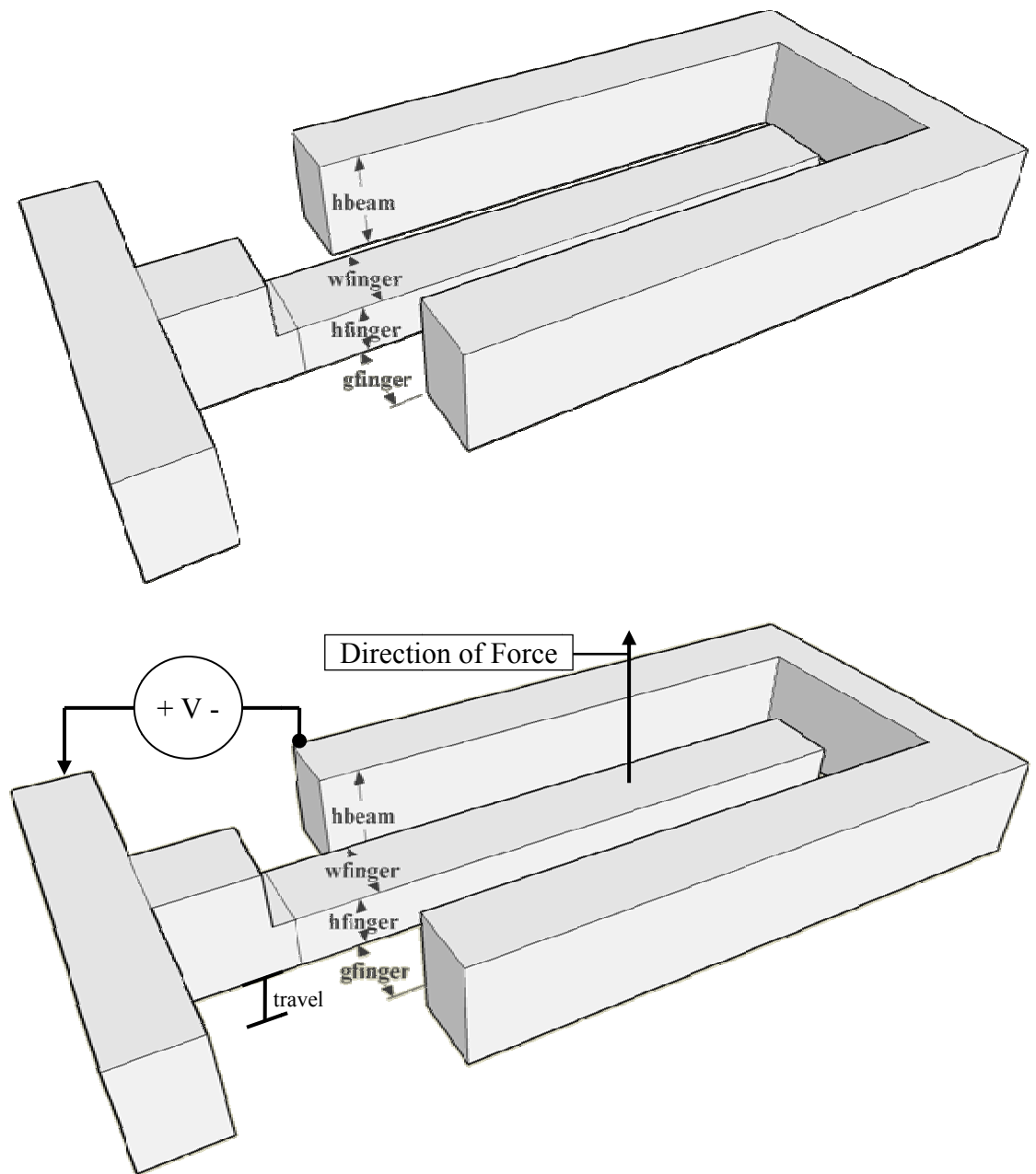
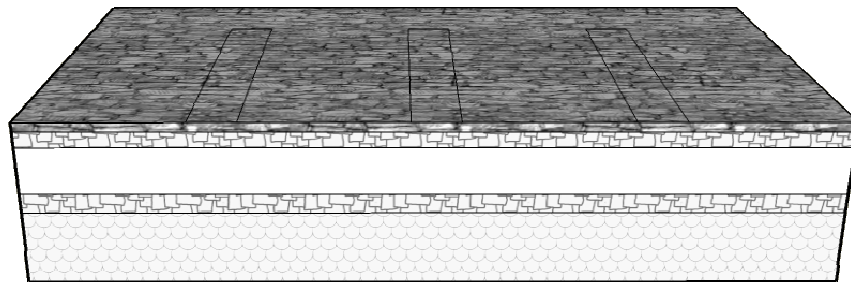
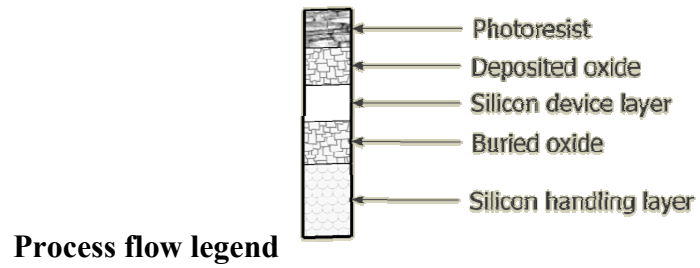


**Figure 36: Vertical offset combs close-up; unactuated device (top), actuated device (bottom)**

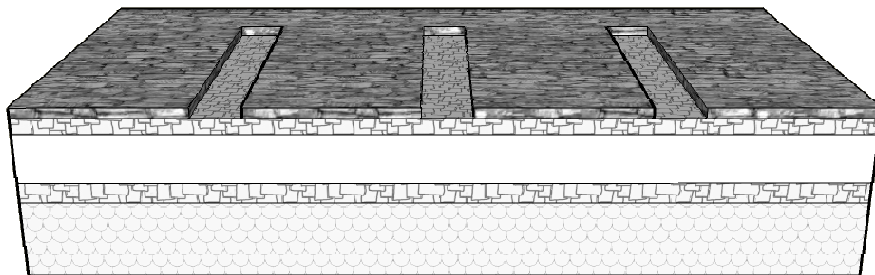
### 5.3 Fabrication of Vertically Offset Comb-Drives

Processing of vertically offset comb-drives is accomplished through the use of protective oxide caps to allow for the timed deep reactive ion etching (DRIE) of the offset combs.

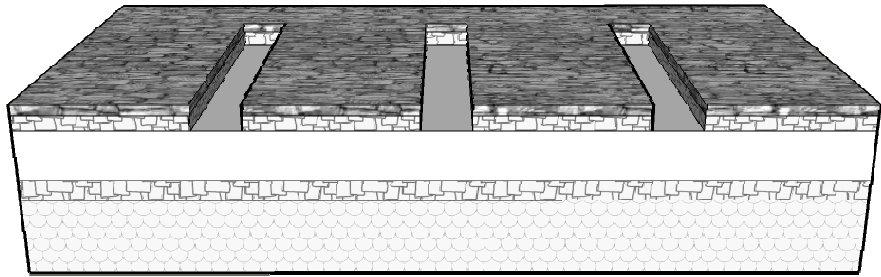
The process can be done on any material for the structural layer; however, we used silicon-on-insulator (SOI) wafers due to their compliance with industry standards and the mirror-quality surface of the single-crystal-silicon (SCS) device layer. **Figure 37** shows the process steps.



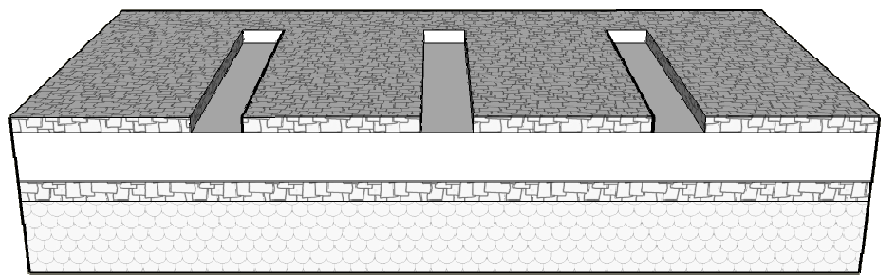
**a. Pattern photoresist for the vertically offset combs.**



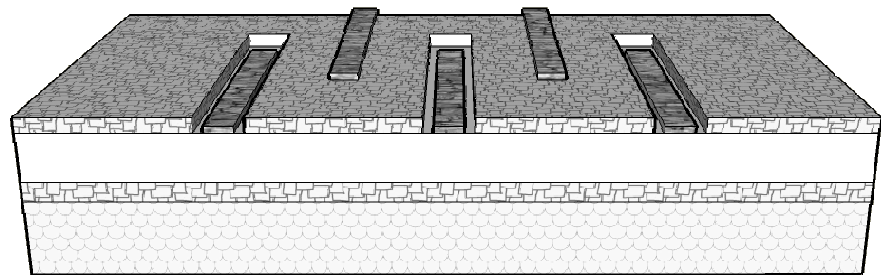
**b. Expose and develop photoresist for the vertically offset combs.**



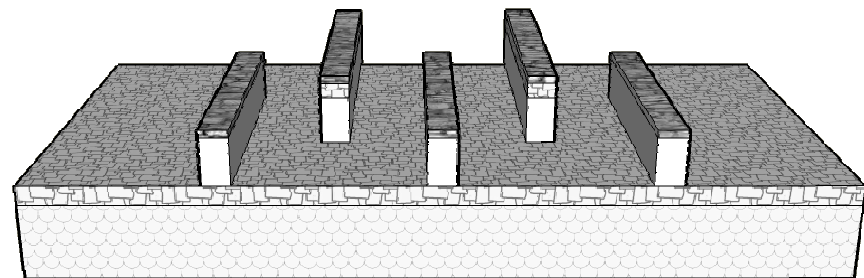
**c. Etch the deposited oxide layer.**



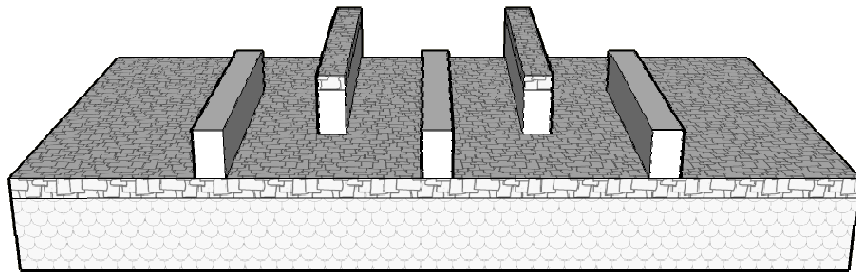
**d. Remove photoresist.**



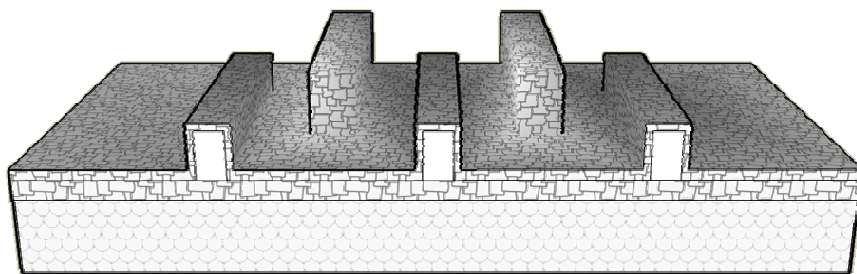
**e. Pattern photoresist to define structures.**



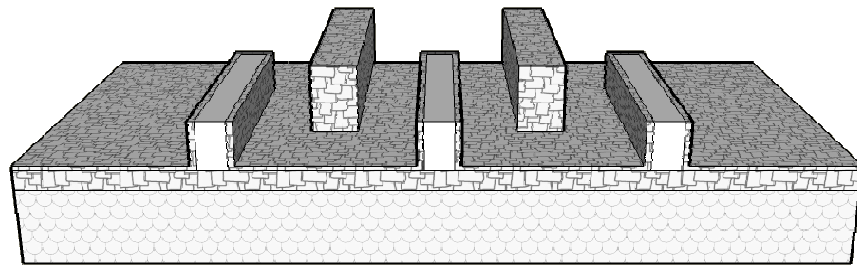
**f. Etch structures.**



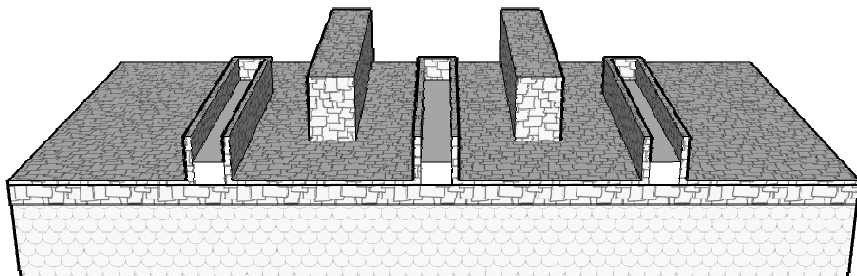
**g. Remove photoresist.**



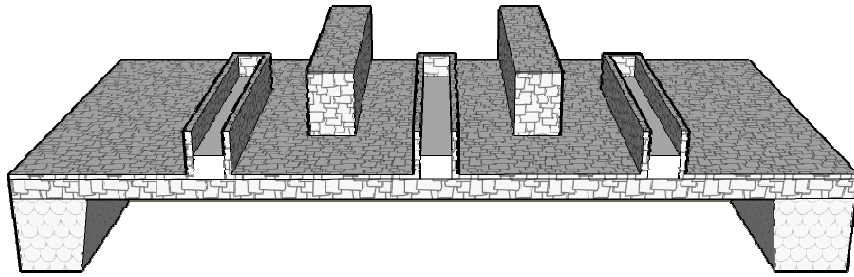
**h. Deposit another oxide layer to protect sidewalls.**



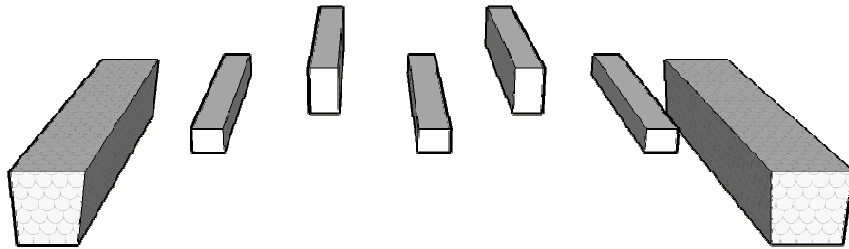
**i. Etch oxide layer to expose vertically offset combs for DRIE.**



**j. Etch Silicon with a timed deep reactive ion etch (DRIE).**



**k. Backside etch**



**l. Released structures**

**Figure 37: Brief view of the process used to fabricate vertically offset combs.**

It is important to note that the sidewall will become uneven during the anisotropic silicon etch without an oxide protective layer (step j in **Figure 37**). This unevenness will result in concentration of charges along the edges of the vertical actuators and reduce symmetry that could unbalance the scanner and reduce its performance.

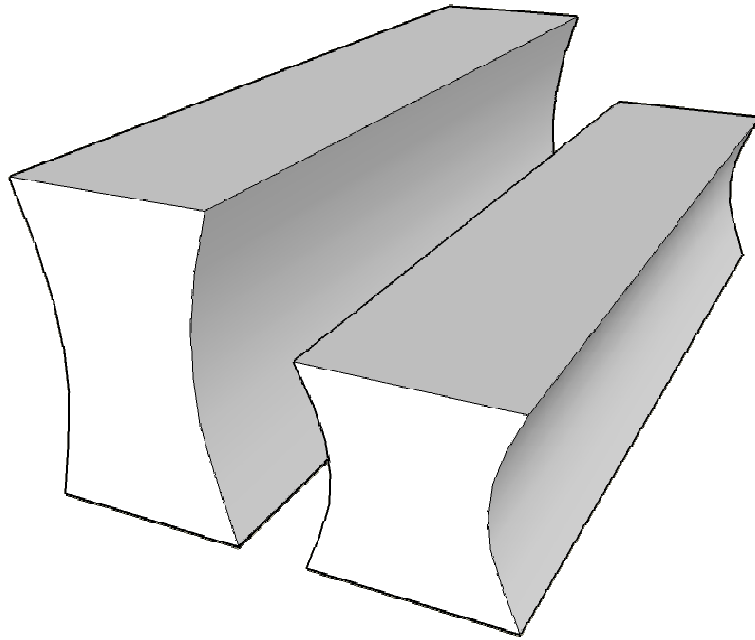


**Figure 38: Uneven sidewalls as a result of the anisotropic silicon etch.**

The protective layer of silicon dioxide protects the sidewalls just as it prevents the structural layers from being vertically etched during the timed-isotropic silicon etch (step j in **Figure 37**). An SEM shows the fabrication of the scanning mirrors at this stage (**Figure 39**). The waviness of the oxide shell around the vertically offset combs is due to compressive stress in the SiO<sub>2</sub> layer.

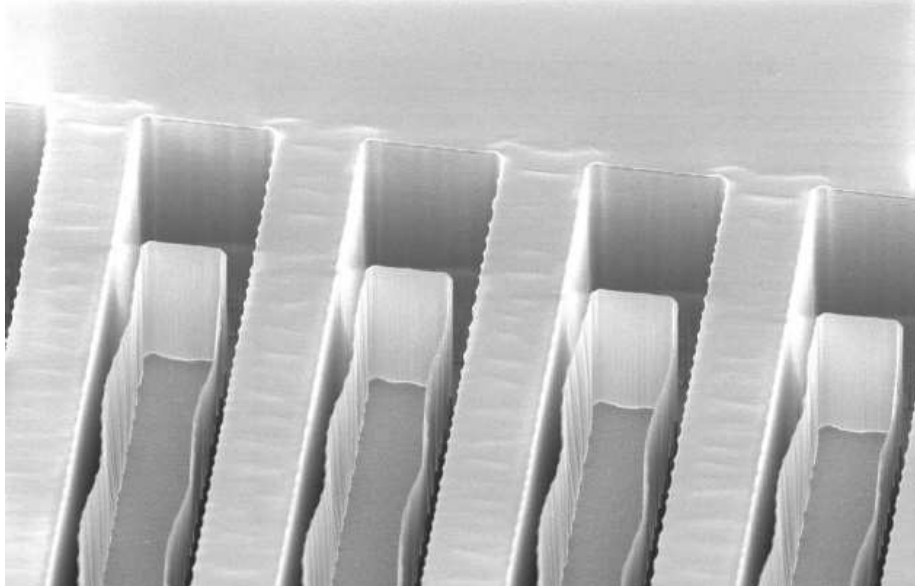


**Figure 39:** SEM image close-up shows the 25  $\mu\text{m}$  offset height on the combs for a 50  $\mu\text{m}$  thick device layer. The protective silicon dioxide layer is visible.

When this oxide layer is released through HF vapor or CPD (critical point drying), the corners and edges are well defined. An SEM shows the released combs that are vertically offset as well as not offset (**Figure 40**). There is little chance of electrical instabilities in the resulting comb-drives during actuation because the edges of the comb fingers are sharply defined. The radii of curvature of the edges are under 250 nm as is visible from the SEM in **Figure 40**.

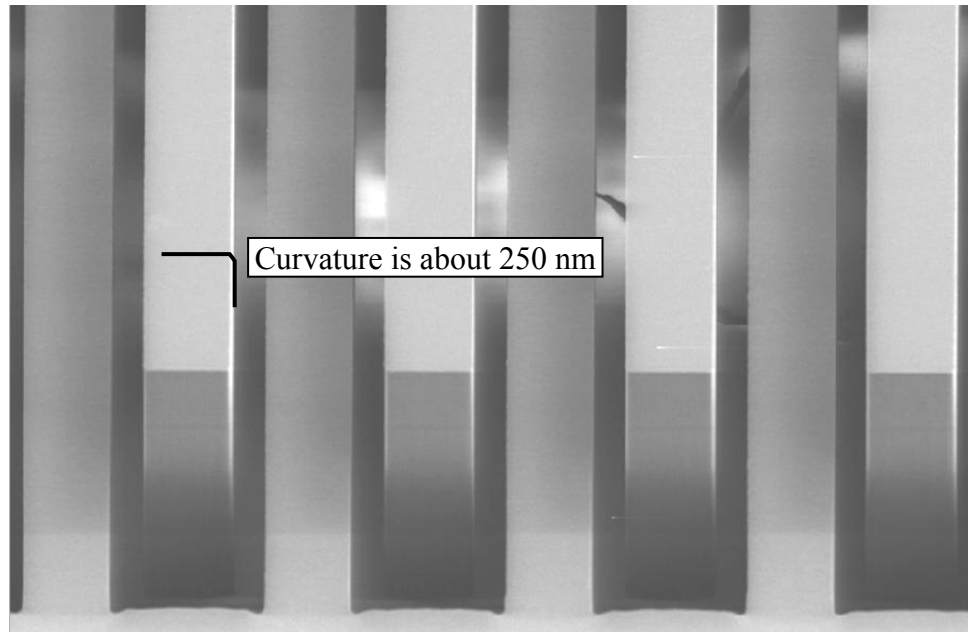


**Figure 40: SEM image close-up of the released vertically offset combs showing the clearly defined sidewalls and sharp edges (labeled).**

The variations of the vertically offset surface heights were obtained using a WYKO NT3300 Optical Surface Profiler<sup>6</sup>. The fluctuations were typically 0.5 to 2 microns for a 50 micron device layer (similar to the thickness fluctuations for the actual device layer as specified).

## 5.4 Potential Applications of Vertically Offset Comb-Drives

Having a well-calibrated force over a large translational distance is an invaluable tool for designing out-of-plane actuating MEMS structures. It has been shown that such structures can be used to measure vertical acceleration accurately. Here, we also envision it can be useful in pressure sensing application, vertical stage positioning, and providing very

---

<sup>6</sup> <http://microlab.berkeley.edu/labmanual/chap8/8.13.html>

accurate forces to biological material. A proposed method of manipulating cells would use a MEMS chip to supply the mechanical stimulus that is typically provided by neighboring cells – accurately controlling this supplied stimulus would allow for the study of cell mechanical signaling and differentiation.

Because the backside of these devices is removed, stiction effects are minimized as the only surfaces that get close to each other are between the comb fingers. Provided that the device suspension is stiff enough, we have demonstrated that these devices can be dipped in water, taken out, dried off, and they are not mechanically stuck together. Minimizing the interacting surface area also helps to improve the Q-factor of an out-of-plane resonator by reducing the damping (see Eq. 4).

By and large, the majority of applications explored consist of photonics devices. In Chapters 6 and 7, we explore more deeply two types of actuators: torsional microscanners and phase-shifting interferometers. A torsional microscanner is a resonator that oscillates about a torsional beam and a phase-shifting interferometer is essentially a vertically resonating plate.

#### 5.4.1 Metrology for Characterizing Out-of-Plane Actuation and Sensing

To calibrate these out-of-plane structures, we can apply the methods of Chapter 4 to determine the effective Young's Modulus, beam dimensions, gaps, and in-plane comb-drive forces for the structures. A remaining parameter is to determine the out-of-plane force exerted by the comb-drive. This parameter can be determined in an optical fashion

by measuring the displacement with an interferometer,  $x$ , of a suspended structure while also measuring the capacitance change across the driving combs,  $\Delta C$ , and using the relationship  $F = \frac{V^2 \Delta C}{x}$ , where  $V$  is the driving voltage. The parameter can also be determined mathematically by using the other extracted parameters and analytically solving for the fringing-field effect. However, a probed measurement of force is difficult to make because a well-calibrated distance must be traveled. Fortunately, the ground plane can be made to exist and the thickness,  $x=x_t$ , is usually known of the oxide layer upon which the devices sit. This fact saves us because we can actuate a suspension so that the device layer makes contact with the ground layer and monitor for this event by monitoring the resistance between the ground layer and the device layer. We must be careful however to make sure the contact region between the device layer and ground layer is small so as to prevent stiction and have the proximity forces (rarefaction, Casimir) as the plates move close together distort the measurement of force.

#### 5.4.2 Torsional Twist-Up Structures using Staggered Comb-drive Arrays

It can be noted that non-resonant vertical actuation is still limited to a few microns. To extend the translational distance of out-of-plane actuators, we introduce the idea of staggering the comb structures. This type of structure is formed by staggering the bendable part of the suspension so that the combs maintain their position and provide a continuous force over the entire length of the beam as the beam twists. A visual representation is shown in **Figure 41**. A simulation of the structure in SUGAR is shown in **Figure 42**.

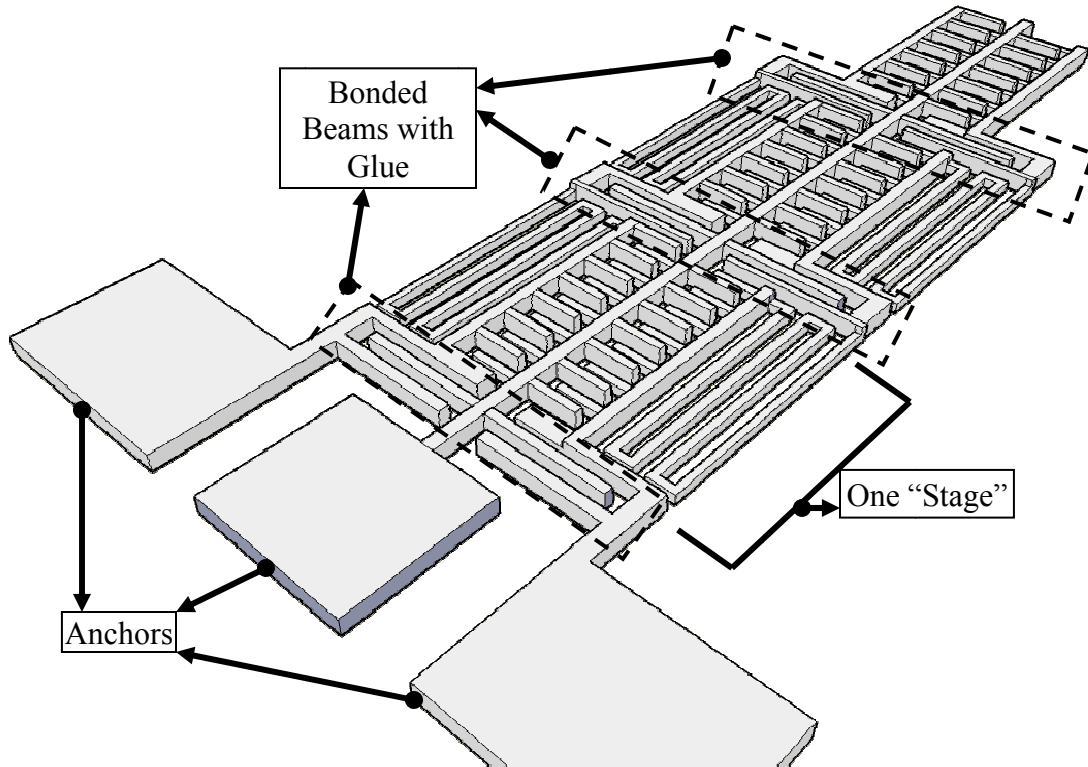


**Figure 41: Balanced twist-up structure.** The three main bars along the shaft must be glued to the outer suspensions with insulative glue (epoxy) (Choo and Muller, 2003).

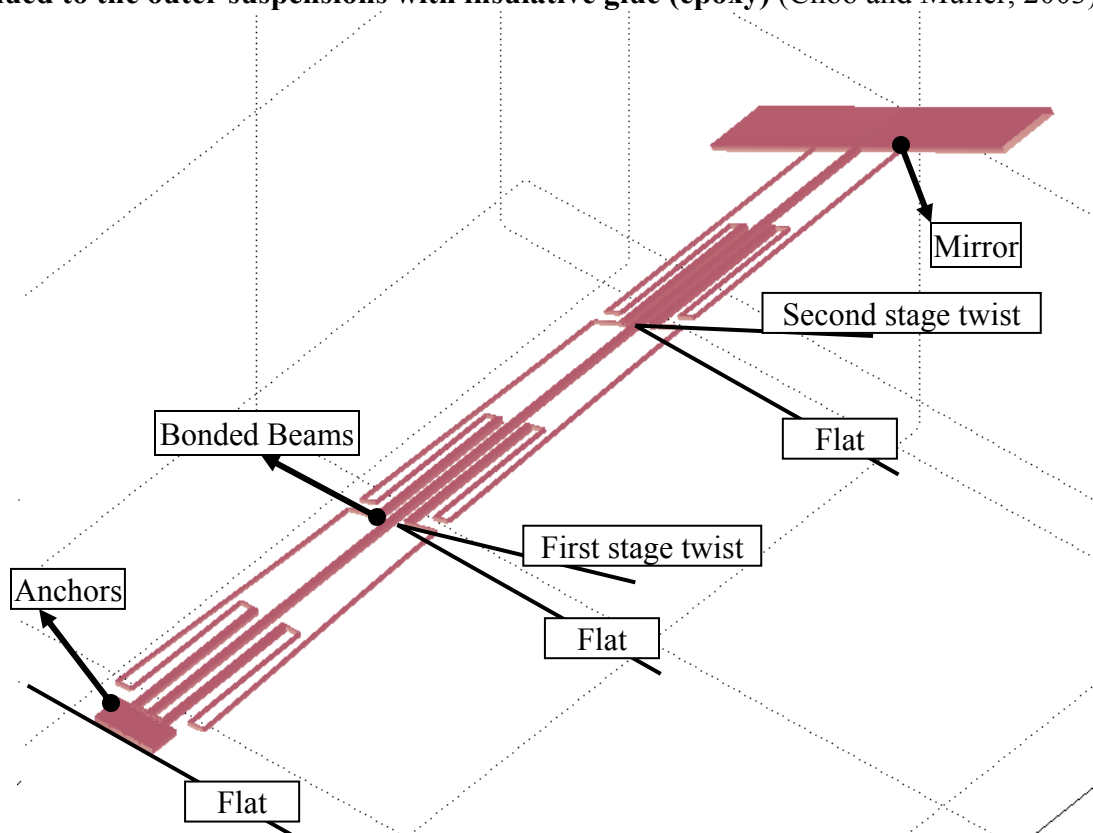


**Figure 42: Sugar model of the twist-up.** Note that the combs will always be aligned.

As more stages are added, the structure can twist further. Therefore with this approach, it becomes possible to make scanning mirrors that will operate over 360 degrees or translating plates that bend more than 1 mm out-of-plane while still maintaining fine control over the displacement.

### 5.4.3 Deformable Parabolic Mirrors

The strength of the out-of-plane force is sufficient to bend plates. To create a focusable element, the structure is shown in **Figure 43**. The central part is supported by an anchor and in an SOI process, the backside must be released. We modeled a CAD structure (**Figure 44**) that contained near 100,000 vertically offset combs in COMSOL Multiphysics (**Figure 45**). This deformable mirror could be used for a focusing element on a display system where the incoming laser light is collimated and the outgoing light needs to be focused and possibly recollimated quickly (Gerbe and Migozzi 1995). Another use for this device is in focusing incoming light onto an imaging plan for an auto-focusing system as in the case of a parabolic mirror for imaging in confocal microscopy (Lieb and Meixner 2001).

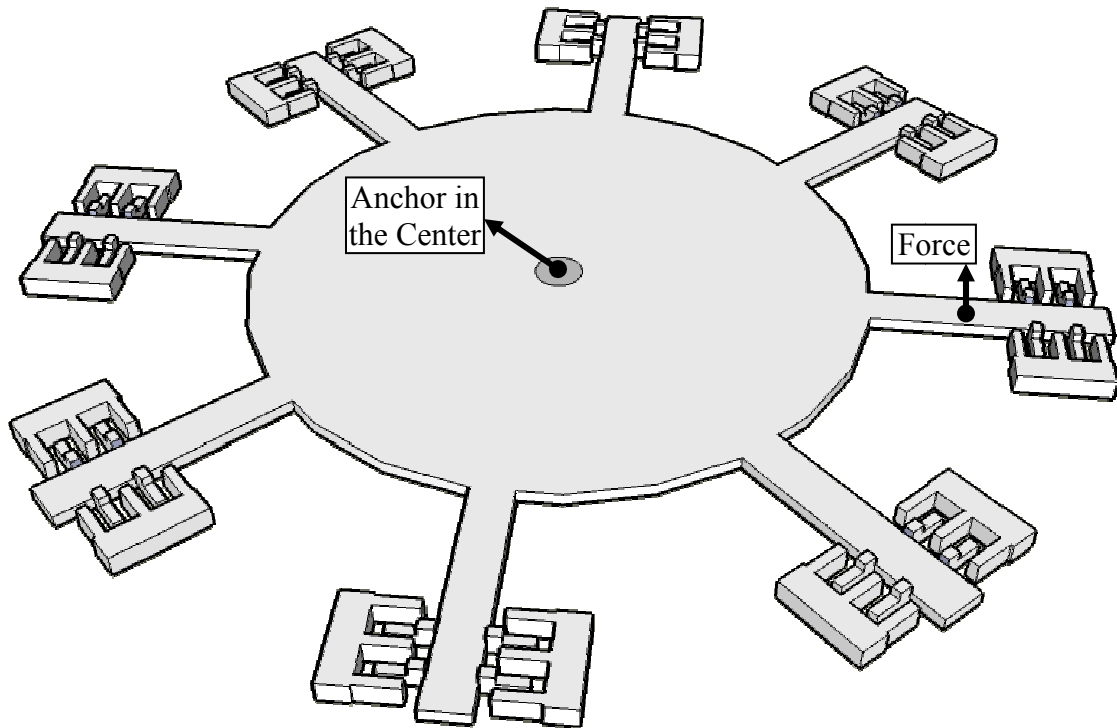


Figure 43: Mirror element made with vertical offset combs.

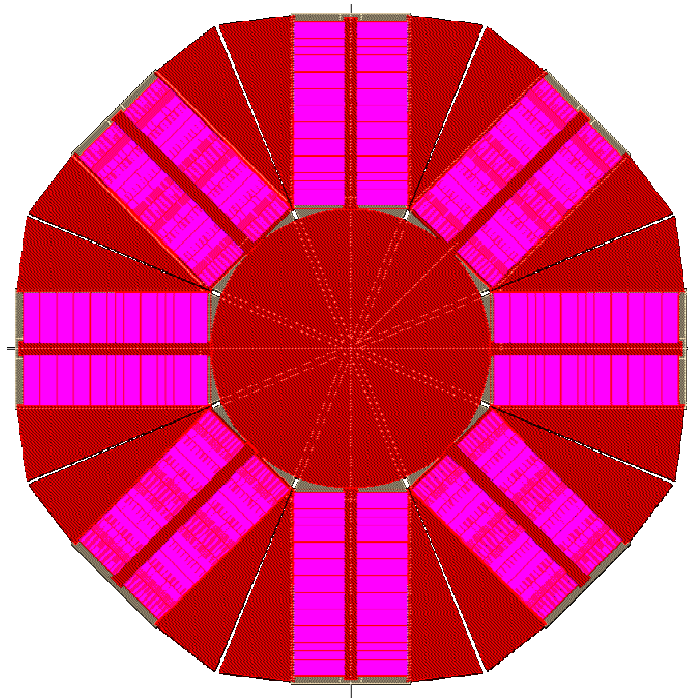
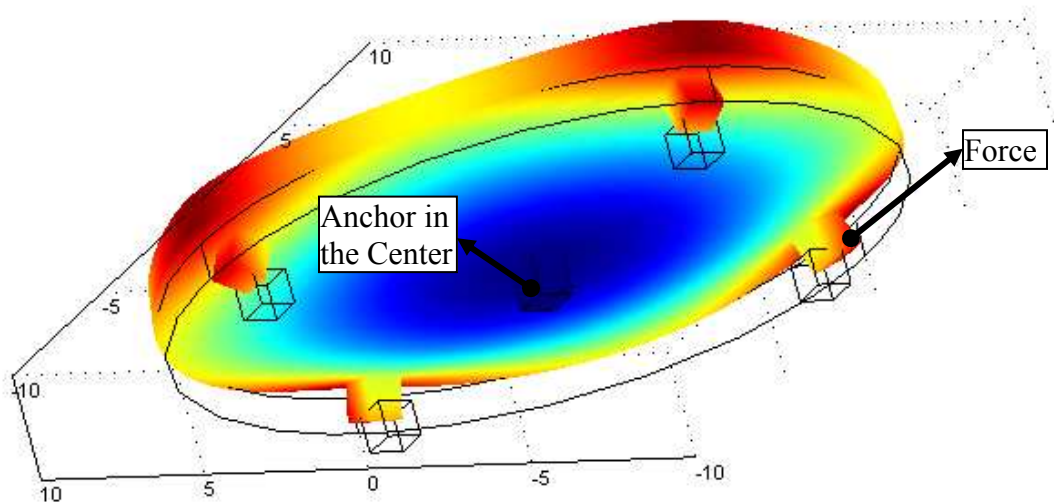


Figure 44: Mirror layout on a 1 cm by 1 cm chip that contains about 100K vertically offset comb fingers. Red (dark) represents the device layer, and purple (light) represents the offset-combs.



**Figure 45: Deformation of a mirror (radius = 10 mm, thickness = 2 mm) anchored in the center with uniform forces supplied at the 4 outer points. The deformation near the center is approximately parabolic.**

## 5.5 Summary

We have developed a novel process for inexpensively adding another dimension of motion to MEMS structures. The process is compatible with industry standards for developing CMOS, and as such, can be integrated with circuits. Furthermore, because there is no wafer-bonding involved, the process is highly reliable and produces high yield. This fact allows these devices to be arrayed together. Arraying vertical actuators together allows one to make many useful systems such as adaptive optics for telescopes and telecommunication systems. Optical and electronic metrology can be employed for such structures to ensure reliable operation for applications requiring high precision. We have explored the types of devices possible with this process, including fast refocusable mirrors and extended-range torsional actuation.

## Chapter 6: MEMS Metrology Applied to Enable Phase-Shifting Interferometry

This chapter uses the process and design developments of Chapter 5 in making a MEMS-based fast phase-shifting interferometer (MBPSI) that improves the speed of phase shifting interferometry, one of the most precise methods of interferometry, by a factor of more than 100 while reducing the cost by a factor of 100. This type of interferometry is made possible by the fact that the motion of electrostatically actuated mirrors is very precisely controllable (as discussed in Chapter 2). Section 6.1 motivates this chapter's work on the development of metrology techniques for sensing and characterizing MBPSI. Section 6.2 addresses the key challenge of improving the study of fast-moving phenomena (e.g. structures under the view of the microscope that move more than 100 nm between camera frames). Section 6.3 explains how the phase-shifting is achieved through a resonant MEMS phase-shifting plate. Section 6.3 also addresses lowering the cost of the laser from a pulsed laser diode to a continuous laser in interferometry systems using a phase-plate stepping approach and also lowering the noise level by allowing higher amplitude laser pulses. Section 6.4 provides the fabrication steps and results as well as the characterization data for the MBPSI and some phase-shifting results. This chapter contains parts from our papers, (Choo et al., Fast, MEMS-based Phase-Shifting Interferometer 2006) and (Choo et al., MEMS-Based, Phase-Shifting Interferometer 2006), and our patent (Choo et al. 2006).

## 6.1 Motivation for MEMS-based Phase-Shifting Interferometry

The ability to precisely control the vertical position of a mirror leads to a new type of interferometry – MEMS-based, phase-shifting interferometry (MBPSI). MBPSI is distinguished from regular phase-shifting interferometry in that it focuses on measuring sub-second transient phenomena. We have demonstrated up to 300 height-maps per second with an rms noise of 2nm. Conventional phase-shifting interferometry (PSI) typically uses piezoelectric actuators instead of electrostatic MEMS actuators. Piezoelectric actuators cannot operate as fast as MEMS actuators, suffer from hysteresis, and cost more to make and drive accurately. Other methods for achieving PSI include stroboscopic interferometry (Hart, et al. 2000) which requires periodic motion of the sample, Zeeman-split two-frequency laser control (Burgwald and Kruger 1970) which is expensive, modulating laser-diode drive currents (Suzuki, Sasaki and Maruyama, Phase Locked Laser Diode Interferometry for Surface Profile Measurement 1989) (Suzuki et al. 1991) which suffers from thermal instabilities, and polarization of four separate light sources (Nakadate and Yamaguchi n.d.) (Onuma, Tsukamoto and Nakadate 1993) with different phase-offsets and specially made CMOS imagers that filter the polarized light to produce the four phasemaps which reduces the spatial resolution of the result by a factor of 4. Our MBPSI approach is ideal in achieving a low-cost and highly reproducible phase-shifting component.

## 6.2 Time-domain Limitations

This section introduces a new method for improving phase-shifting interferometry (PSI) in resolving motional changes of the sample being viewed. In PSI, we are attempting to solve a system of equations as introduced in Section 3.3 and rewritten in Eq. 18. As surface changes become rapid (approaching 10's of nanometers of motion in the time between frame-captures), we reach a difficult point where the surface does not stay fixed in a sequence of 4 interferometer captures.

Using the standard 4 frame capture technique, the per-pixel error is roughly linear with respect to the motion between frames for small inter-frame displacements (Eq. 18). Recall from Eq. 11 in Section 3.3 that  $A$  represents the intensity (different for each pixel),  $B$  represents the contrast,  $\varphi$  represents the phase-offset of the surface (for which we are attempting to solve), and  $I_1, I_2, I_3,$  and  $I_4$  represent the pixel intensity for each of the four frames captured. Here we introduce the variable,  $e$ , which represents the error in the last phase captured because the sample moved quickly at that pixel location and changed the observed phase.

$$\begin{aligned} I_1 &= A + B\cos(\varphi) \\ I_2 &= A - B\sin(\varphi) \\ I_3 &= A - B\cos(\varphi) \\ I_4 &= A + B\sin(\varphi + e) \end{aligned} \quad , \quad \text{atan}(I_4 - I_2, I_1 - I_3) \approx \varphi + \frac{\cos^2(\varphi)}{2} e + O(e^2) \quad \text{Eq. 18}$$

However, using a predictor-corrector method, we can eliminate most of this error. We employ a 2-step process to first predict the phase,  $\varphi'_4$ , from previous values for  $A$  and  $B$ , ( $A_{\text{old}}$  and  $B_{\text{old}}$ ) and then solve for new values for  $A$  and  $B$ , ( $A_{\text{new}}$  and  $B_{\text{new}}$ ) and use these values to then correct the phase value (Eq. 19). Note that the  $+\cos$ ,  $-\sin$ ,  $-\cos$ , and  $+\sin$

terms must be cycled incrementally – we only show one of the four cases here. For this case, we also obtain an estimate on the phase error,  $\frac{|I_4 - (A_{\text{new}} + B_{\text{new}} \sin(\varphi_4))|}{B_{\text{new}}}$ , which may be similarly obtained for the other three cycled cases as well.

$$\varphi'_4 = \text{asin} \left( \frac{I_4 - A_{\text{old}}}{B_{\text{old}}} \right) \rightarrow \begin{cases} I_1 = A_{\text{new}} + B_{\text{new}} \cos(\varphi_1) \\ I_2 = A_{\text{new}} - B_{\text{new}} \sin(\varphi_2) \\ I_3 = A_{\text{new}} - B_{\text{new}} \cos(\varphi_3) \\ I_4 = A_{\text{new}} + B_{\text{new}} \sin(\varphi_4) \end{cases} \rightarrow \varphi_4 = \text{asin} \left( \frac{I_4 - A_{\text{new}}}{B_{\text{new}}} \right) \quad \text{Eq. 19}$$

We run several simulated trials on the two approaches for tracking an individual pixel's phase and show the error in both approaches (**Figure 46**). The error in the second approach is mainly dependent on the variation in the A and B terms.

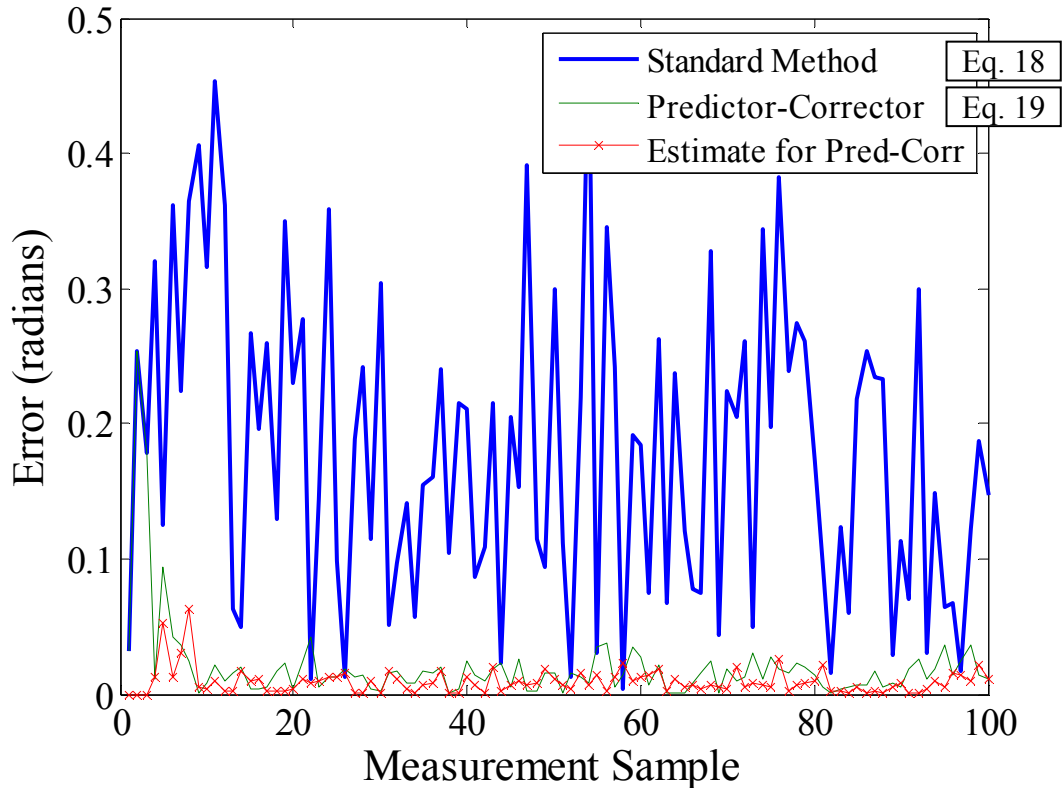


**Figure 46: Error for each measurement using the standard and predictor-corrector methods along with the predictor-corrector estimated error. The contrast, B, and intensity, A, values were given 1% uniform random noise, and the average relative measured phase error using the predictor-corrector method was 1%.**

### 6.3 Phase-shifting Procedures

One approach to creating the 4 offset phases is by resonating the phase-shifting plate and pulsing the laser so that a frame is captured with the precise phase-offset (see **Figure 47**). This method is simple and reliable. However, it does rely more heavily on the timing of the laser pulses, on the ability of the laser to pulse (which increases the cost of the laser), and as the desired capture time becomes shorter, the laser pulse amplitude must be increased. Another method is to step the plate. However, as described in Chapter 1, this method is difficult to implement and relies on the metrology described in Chapters 2 and 3 to provide suitable stable operation. Both of these approaches are illustrated in **Figure 48**.

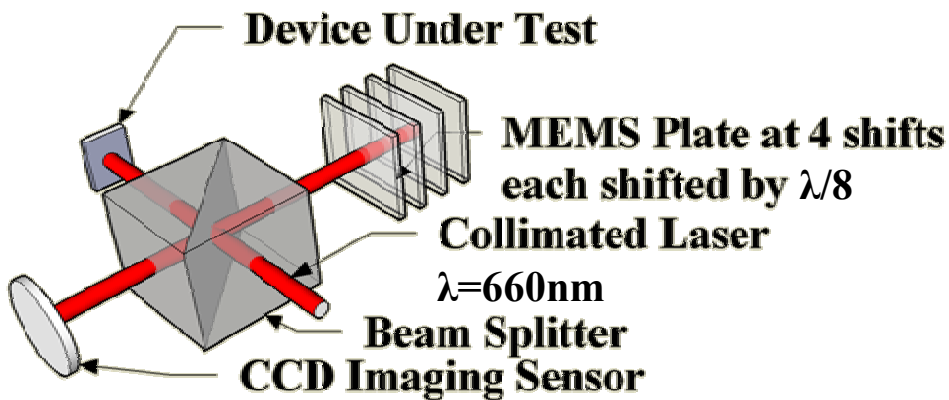


**Figure 47:** Phase-shifting setup showing the collimated laser entering a beam splitter, one path reflecting off of the device under test (DUT), and the other path reflecting off of the MEMS plate which is shifted by  $\lambda/8$  for each of the 4 phase-shifts. A CCD records the interference between the two paths.

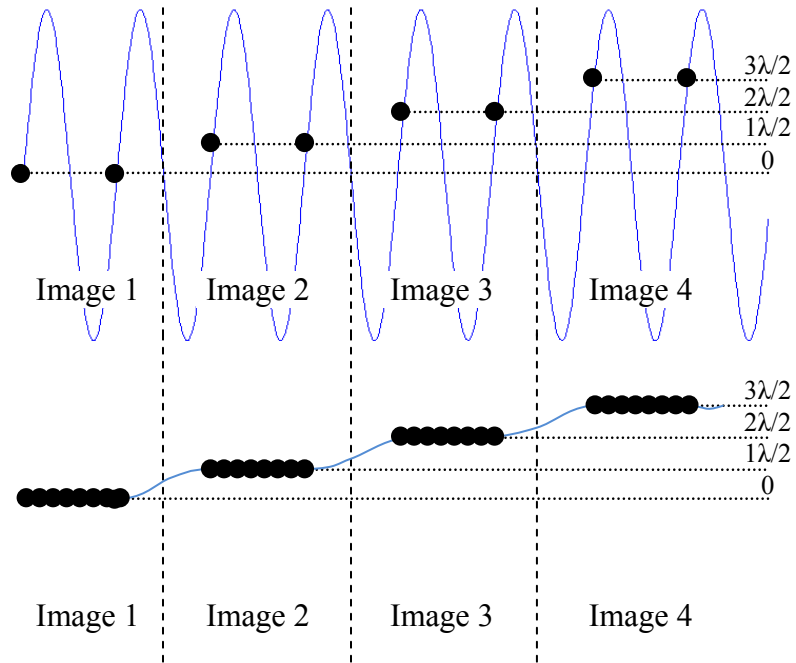


**Figure 48: Phase-shifting by resonating the plate (top) and by stepping the plate (bottom). The blue (solid) curves show the plate motion over time, and the black dots show the time and shift of each laser pulse.**

Once the four phases are produced, the wrapped interferogram may be produced through Eq. 18 in the case of a static sample or Eq. 19 in the case of a rapidly moving sample. The unwrapping procedures described in Chapter 3 may then be applied to reconstruct the final surfaces of the sample. The results of each of these steps are shown in **Figure 49** for an actual device.

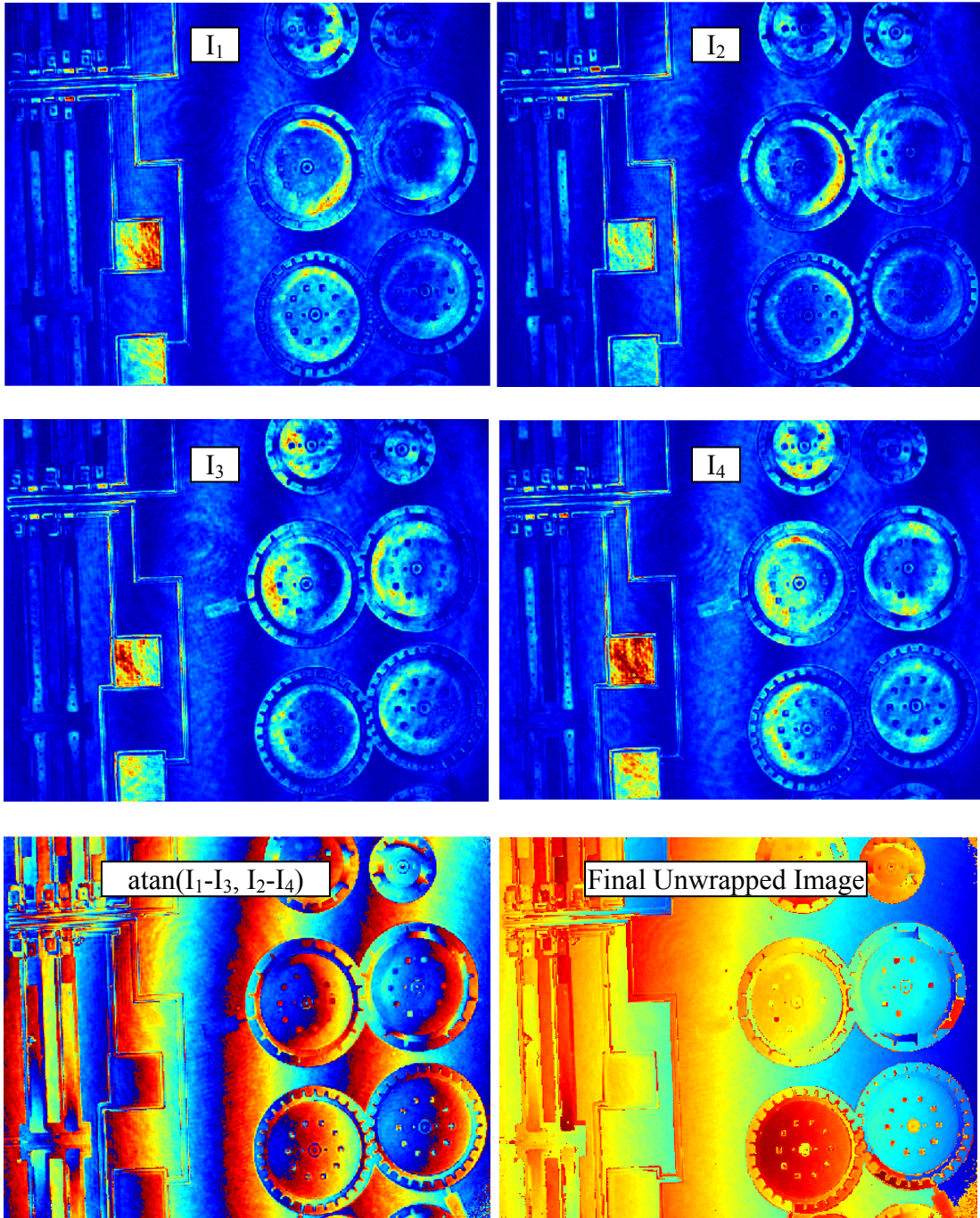


**Figure 49:** All stages of phase shifting interferometry are shown. First, image 1, 2, 3, 4 with necessary phase offsets are shown. Second, the wrapped image is produced (bottom left). Finally, the image is unwrapped (bottom right).

## 6.4 Fabrication and Characterization

We fabricated 25 chips with designs for discrete stepping and 25 chips with designs for resonant stepping. The specific fabrication steps for creating the phase-shifting plates are detailed in Chapter 5. To review, the process consists of growing 0.5- $\mu\text{m}$  of thermal or low-temperature oxide (LTO), using one mask to pattern and remove the thermal oxide for the fixed combs, using another mask to create patterns for the combs, flexures, and micromirror surface, use deep-reactive-ion-etch (DRIE) to define the micromirror in the device layer, remove the photoresist layer and deposit a very thin layer ( $\sim 0.2 \mu\text{m}$ ) of LTO, use timed-anisotropic-plasma etch to remove 0.2- $\mu\text{m}$  thick LTO, use timed-isotropic silicon-etch to create a set of vertically thinned combs, and finally pattern and open the backside of the micromirror. Release is done using an HF vapor process, although a wet release is also fine. Here we show the WYKO and SEM images of a resonant stepping plate (**Figure 50**).

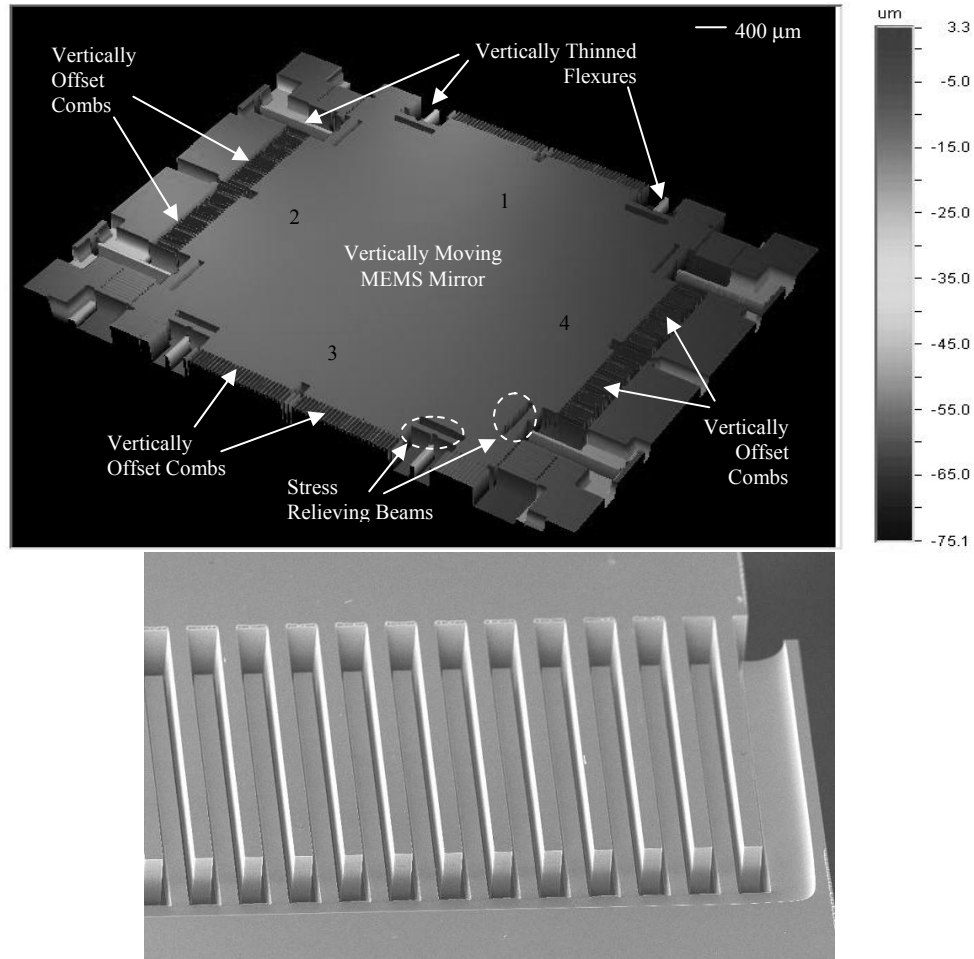


**Figure 50: WYKO of MBPSI plate (top) and SEM of combs (bottom).**

The design process for MEMS phase-shifting mirrors is straightforward. The fabrication of the device is to be done on SOI wafers. The physical sizes of the reflective areas of the MEMS phase-shifting mirrors are determined by considering their uses in specific interferometric configurations. Since our planned interferometric setups are the Twyman-Green and Mach-Zehnder configurations, areas of approximately less than or equal to 5mm-by-5mm rectangles will suffice our needs.

The resonant frequencies of the MEMS phase-shifting plates can be calculated using Eq. 20.

$$f_r = \frac{1}{2\pi} \sqrt{\frac{k}{m}} \quad \text{Eq. 20}$$

$m$  is the mass of the moving structure. The vertical stiffness  $k$  is given by (Ugural 1991)

$$k = 8 \times (24EI l_f^3) \text{ where } I = \frac{1}{12} h^3 w_f. \quad \text{Eq. 21}$$

In Eq. 21,  $h$  is the thickness of the device layer,  $l_f$  is the length of each suspension beam, and  $w_f$  is the width of each suspension beam. The requirement on the precision of resonant frequencies for MEMS phase-shifting micromirrors is very lenient. The important design criterion to keep in mind is that the resonant frequencies of the MEMS phase-shifting micromirrors must be higher than the frame rate of the CCD or CMOS imagers, so that each image frame will capture at least one or more pulses. As a result, we designed our MEMS phase-shifting micromirrors to resonate in a kHz range.

The offset height is 24.9  $\mu\text{m}$  and shows excellent uniformity (less than or equal to  $\pm 1.5\%$  peak-to-peak deviation from the average value) across the wafer.

We have measured the surface profile of a representative micromirror (of 18 that we have produced) using a white-light interferometer WYKO NT3300 (**Figure 50**) and determined that its radius of curvature exceeds 20 m, and its surface-roughness values do not exceed 20 nm. All the fabricated micromirrors had the radius of curvature exceeding 10 m.

In order to time the laser pulses precisely, the mirror resonance has been analyzed using a piezo-based, calibrated stroboscopic interferometer (Hart, et al. 2000), and the results are shown in **Figure 51**. The mirror's relative position at the four corners and at the center is separately recorded over one period of motion of the mirror using the stroboscopic interferometer. The stroboscopic interferometer has an rms measurement accuracy of 5 nm. The measured resonant frequency and mechanical quality factor of the mirror are 3.55 kHz and 63, respectively. When the mirror achieves a resonant amplitude of 1.5  $\mu\text{m}$ , the micromirror passes the phase-shifting positions ( $0$ ,  $\lambda/4$ ,  $\lambda/2$ , and  $3\lambda/4$ , where  $\lambda = 660$  nm) at intervals of 0, 10, 20, and 30  $\mu\text{sec}$ , and using these intervals as delay times, we can achieve precise timings for the laser pulses of 1- $\mu\text{sec}$  duration. The resonant amplitude of 1.5  $\mu\text{m}$  is relatively small for a micromirror with a vertical offset height of 24.9  $\mu\text{m}$ , and this small amplitude requirement keeps the actuation voltage for the micromirror low at 18  $V_{\text{ac}_p\text{-to-}p}$ . The small magnitude of resonant amplitude and the use of stress-relieving beams also keep the micromirror flat during its resonant operation. The dynamic deformation of the mirror, between the center and the four corners of the mirror, within this linear region of operation, is less than 6 nm or  $\lambda/110$  (**Figure 51**).

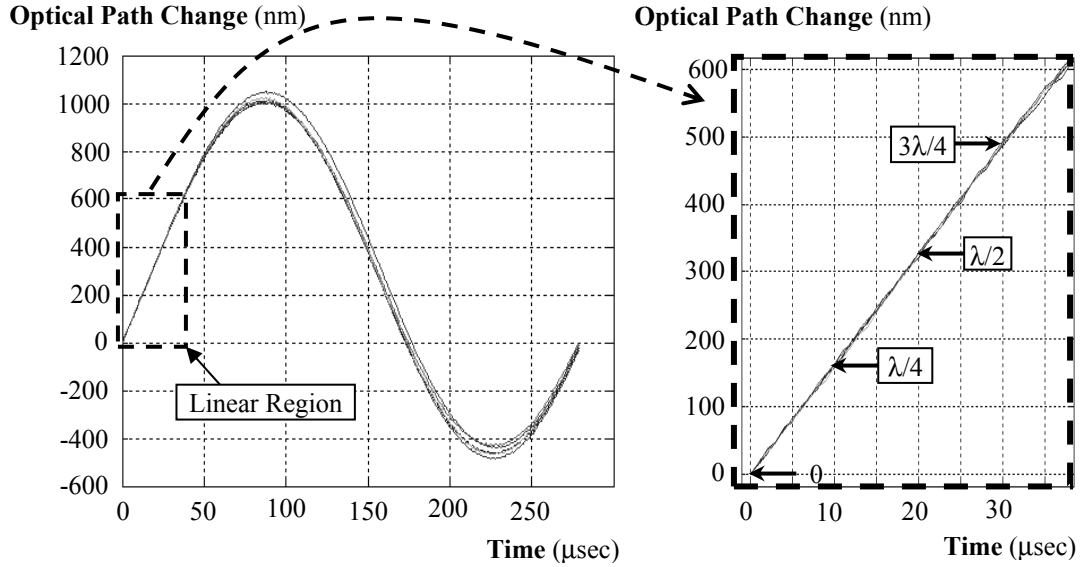


**Figure 51: Resonant-motion analysis for the phase-shifting MEMS mirror at 5 locations on the plate (left) and the linear region used for phase-shifting (right) (peak-to-peak deviation in position:  $< 6\text{ nm}</math>). The 5 locations are shown in Figure 50 at locations labeled 1, 2, 3, 4, and the center of the plate.$**

To demonstrate the measurement capability of the MBPSI, we have used the system to characterize the motion of a PZT (Choo, Kant, et al., Fast, MEMS-based Phase-Shifting Interferometer June 2006) by obtaining 150 measurements of a PZT stepping 100nm every 0.5 seconds with a resolution of the PZT motion below 10nm (Figure 52). We have also employed the system to characterize the motion of a piezo actuator driven at high rates exceeding 30 Hz (Kant, et al. 2007).

**Figure 52: Measurement the response of a PZT stepper (device under test) using our MEMS-based phase shifting interferometer after the plate motion was characterized.**

For stepping the plates, we achieved the calibration curves shown in **Figure 53**. The advantage of stepping the phase-plate instead of resonating the phase-plate is that a continuous-wave (CW) laser may be used instead of a pulsed laser diode. The integration in each frame for a CW laser is done by shuttering the CCD over one step of the phase plate. The stability of a continuous laser is better and the cost is  $1/10^{\text{th}}$  of the laser diode.

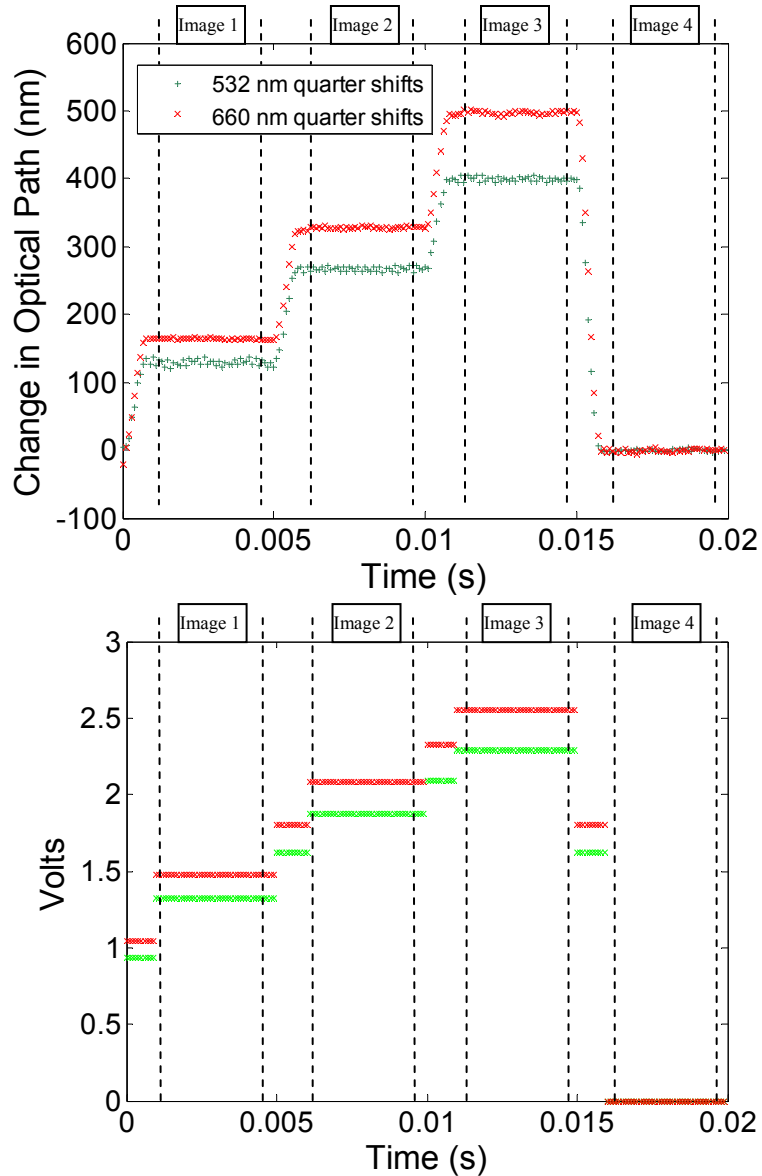


**Figure 53: Motion of stepping plate (top) driven by stepping function (bottom).**

## 6.5 Conclusions

Our MBPSI system is low-cost, high-performance solution to the issue of generating accurate phase-shifts. We can capture at a rate of 300 height-maps per second. This component provides a balance between cost, accuracy, and speed. These improvements

expand the range of PSI applications to the realms of studying fast changing, dynamic phenomena like those of present great interest in fields like biosystems and crystallographic growth (Onuma, Tsukamoto and Nakadate 1993).

## Chapter 7: MEMS Metrology Applied to Enable Torsional-Microscanner Applications

This chapter concerns the creation, development, and application of low-cost, high-performance torsional microscanners. MEMS torsional microscanners are useful in many applications ranging from beam-steering for autonomous aircraft communication (Zhou, et al. August 2003) to microprojectors for mobile devices to laser-based surgery tools. A torsional microscanner is simply composed of a mirror coupled to silicon torsional beams that are anchored to the substrate and actuated by several sets of methods. An important feature of torsional microscanners is that a smaller mass allows a faster response time of the mirror and thinner torsional beams can be rotated through larger angles. Because no rubbing takes place, scanners using torsion beams will last longer than scanners using gimbaled and other types of mechanical supports. Section 7.1 gives a more detailed introduction to microscanner technology.

We have fabricated microscanners using the vertical offset combs as described previously in Section 5. The design of the microscanners is detailed in Section 7.2. The fabrication results are shown in Section 7.3. The characterization of the microscanners is given in Section 7.4. With resonant frequencies between 58 Hz and 24 kHz, actuation voltages between 14.1 and 67.2 Volts, and optical-scanning angles above  $8^\circ$  and reaching  $50^\circ$ , these devices are useful for many scanning applications. Section 7.5 then discusses our metrology techniques and experimental results for demonstrating a laser-ablation system for ocular corneal surgery. The performance of the system exceeds the stability and

accuracy achieved by state-of-the-art ablation systems. Parts of this chapter are based on our patent (Choo et al., Simple Fabrication Process for Self-Aligned, High-Performance Microscanners; Demonstrated Use to Generate a Two-Dimensional Ablation Pattern 2007) and on our publications (Choo et al., A simple process to fabricate self-aligned, high-performance torsional microscanners: demonstrated use in a two-dimensional scanner. 2005) and (Choo et al., Simple Fabrication Process for Self-Aligned, High-Performance Microscanners; Demonstrated Use to Generate a Two-Dimensional Ablation Pattern 2007).

## 7.1 Introduction

Scanners have a wide range of uses in industry including in high-definition and retinal displays, range-finding systems, bar-code scanning for check-out counters, optical switches for telecommunication, tomography systems in biology and medicine, and free-space laser communications. The top priorities in all of these areas are to make these scanners smaller, more cost-effective and durable, faster, and with a greater stability and accuracy (R. Conant 2002). Creating a CMOS-compatible MEMS-fabrication process to create microscanners satisfies all of these goals. MEMS scanners are sufficiently small for most practical applications approaching the diameter limit of collimated laser light (sub millimeter). The small sizes of MEMS scanners also lowers their cost because the wafers are typically fixed in cost. The small size of MEMS lowers the mass of the scanning element and thereby increases the scanning speed and lowers the power consumption. Because the stretching of silicon torsional beams follows Hookes Law,

MEMS scanners are very durable lasting more than a year in continuous lab testing with no degradation in performance.

While electrostatic drives are ideal to create torsional microscanners, the torque produced using current techniques has been insufficient to create large scan angles at low driving voltages (Conant, et al. June 2000). We overcome this challenge by creating vertically offset comb drives with the key realization that both sides do not need to be offset. This realization allows us to make entirely photolithographically defined vertically offset combs in a reliable way and compatible with current MEMS fabrication facilities. Other techniques to create vertically offset electrostatic comb-drives have included using bimorph layers (susceptible to hysteresis) (Patterson, et al. January 2002), aligning two wafers (high labor cost) (Kim, et al. June 2003), and depositing multiple-masking layers (expensive and alignment inaccuracies go up linearly with the number of layers) (McCormick and Tien August 2003). We decided to focus our research on the development of fabrication methods that would produce vertically offset comb pairs using more conventional IC processing tools.

Galvano scanners are the current method of choice for steering the laser beams in ocular corneal surgery (Bille, Harner and Loesel 2004). Galvano scanners work by mechanically positioning the mirrors using electric-stepper motors. However, typical galvano scanners cost over \$10000 for precise motion control and must be replaced every 2 years in systems for LASIK eye surgery. MEMS scanners are ideal for this application if they can perform well enough. We fabricated and demonstrated their performance and compared

this performance to the performance of commercial eye-surgery microscanners in simulating the ablation of a prespecified image.

The processing technique used in making these torsional microscanners is unique in allowing the practical gap size to be reduced below 1 micron while maintaining very good alignment. This fact allows more vertical actuators to fit in a given area as well as increases the force proportional to the inverse of the gap size. A good alignment of the vertically offset combs will also allow a higher potential to be used to actuate the microscanners.

## 7.2 Design of the Torsional Microscanner

We have investigated different designs of microscanners. The main design components are the shape and size of the central mirror, the torsional beam supporting the mirror, and the actuators driving the mirror. As the mirror is made larger, the resonant frequency of the mirror decreases. As the mirror is made smaller, alignment with a laser becomes more difficult and damping makes it harder to achieve a large optical scanning angle. To reduce the chip real estate, a straight torsional beam may be replaced with a crab suspension. The components of a microscanner are shown in **Figure 54**.

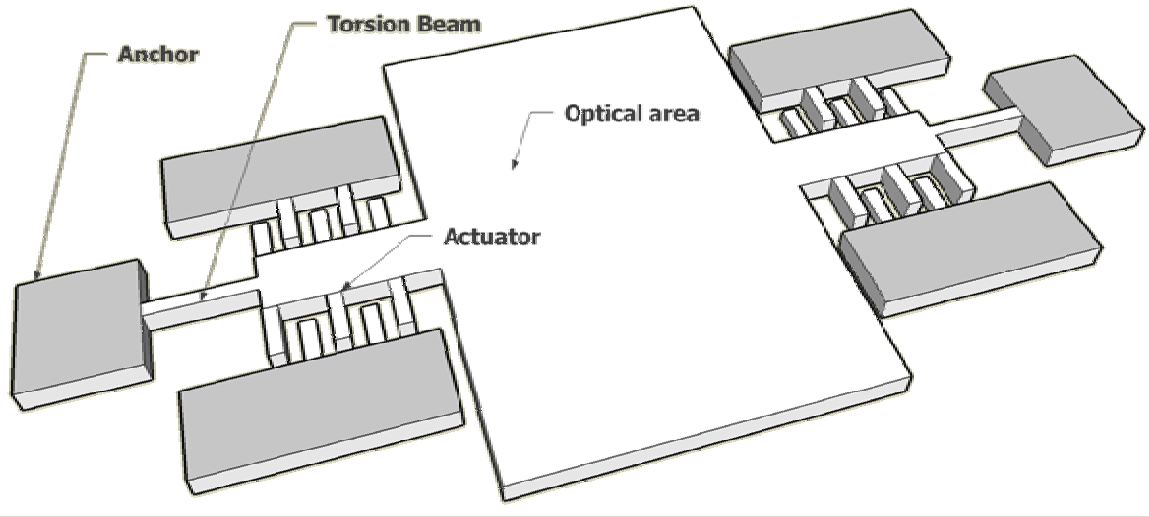


**Figure 54: The different components of a scanning mirror. Anchored components are shown in gray.**

We have varied the dimensions and shapes (circular or rectangular) of the optically reflective areas as well as the lengths and the widths of the torsion beams. The resonant frequency can be predicted from Timoshenko's equation (Eq. 22) (Timoshenko and Goodier 1951).

$$f_r = \frac{1}{2\pi} \sqrt{\frac{k_t}{I_m}}, k_t = \frac{1}{3} G w_t^3 \frac{h_t}{l_t} \left( 1 - \frac{192}{\pi^5} \frac{w_t}{h_t} \sum_{n=1,3,5,\dots}^{\infty} \frac{1}{n^5} \tanh\left(\frac{n\pi h_t}{2w_t}\right) \right); h_t > w_t \quad \text{Eq. 22}$$

In Eq. 22,  $G$  is the torsional modulus for silicon,  $I_m$  is the mass-moment of inertia of the microscanner calculated from the geometry, and  $w_t$  and  $h_t$  are the width and height of the beam. If a circular scanner of diameter,  $d$ , density,  $\rho$ , and thickness,  $t$ , is used, the moment of inertia is simply  $\frac{\pi \rho t d^3}{64}$ . If a rectangular plate of length,  $l$ , and width,  $w$ , is used, the moment of inertia is  $\frac{\rho t l w^3}{12}$ .

### 7.3 Fabrication of the Torsional Microscanner

The fabrication of the microscanners was similar to the fabrication of the phase-shifting interferometers and is further detailed in (Choo et al., Simple Fabrication Process for Self-Aligned, High-Performance Microscanners; Demonstrated Use to Generate a Two-Dimensional Ablation Pattern 2007). However, the microscanner fabrication process started with a  $\langle 100 \rangle$   $n$ -type SOI wafer with a device-layer thickness of 30 or 50  $\mu\text{m}$  and resistivity ranging from 0.005-0.01  $\Omega\text{-cm}$ . For releasing the microstructures, we found that because the backside was removed, the torsional scanners could be wet-released in HF without a critical-point-drying (CPD) step and not suffer from any stiction effects. The durability of the final scanner was tested by dropping it from heights of up to 1 meter without any damage to the scanner.

The fabricated microscanners are shown after being processed using an SEM (**Figure 55** and **Figure 56**).

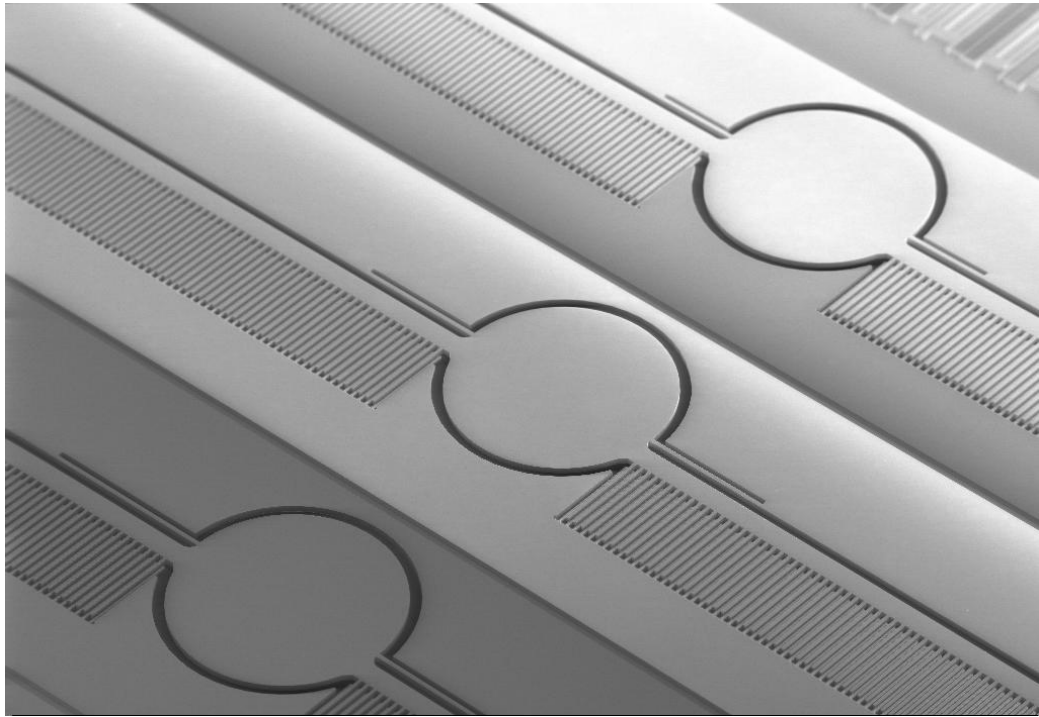


**Figure 55: SEM image of circular microscanners (5 kHz – 7 kHz resonant frequencies).**

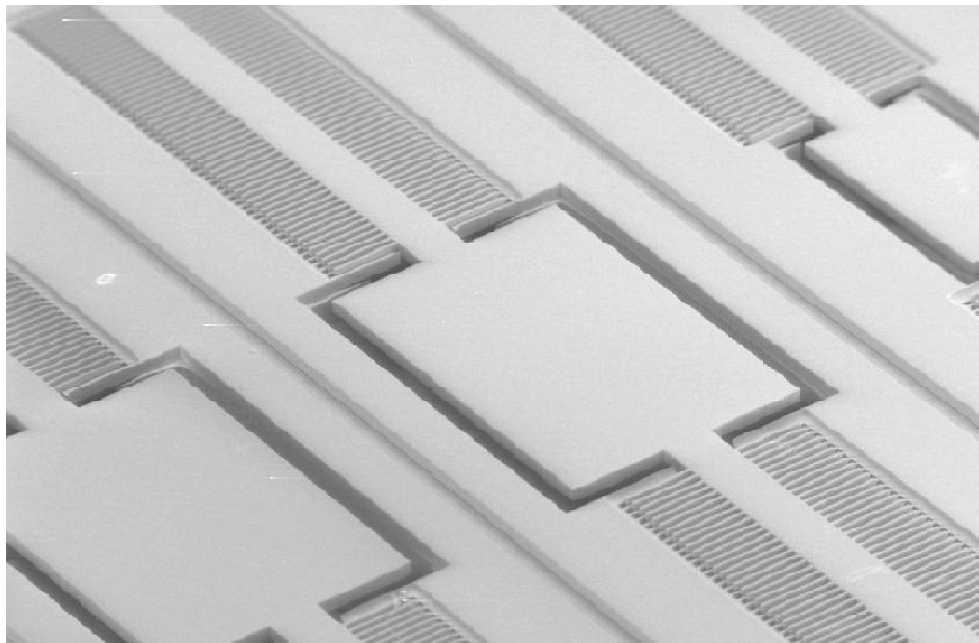


**Figure 56: SEM image of rectangular microscanners (17 kHz – 24 kHz).**

## 7.4 Testing and Characterization of the Torsional Microscanner

We tested the micromirrors for resonant frequencies ( $f_r$ ) (ranged from 58 Hz to 24 kHz), Q-factor (ranged from 40 to 300), and maximum optical-scan angles (OSA) (ranged from 8° to 48°). The actuation voltages ranged from 14 to 67 V<sub>ac</sub>. We made these measurements by reflecting a laser beam off of the scanning mirror and measuring the size of the swept beam against the wall. (**Figure 57**)

$f_r$	Q	OSA	V <sub>ac</sub> (rms)	Dimensions
58 Hz*	40	20.8 °	14.1	$l = 3$ mm $w = 8$ mm
6.01 kHz**	67	24.2 °	26.4	$d = 1$ mm (Circular Microscanner)
8.89 kHz**	70	22 °	34.9	$d = 1$ mm (Circular Microscanner)
12.5 kHz ***	180	48 °	67.2	$l = 1.5$ mm $w = 1$ mm
24 kHz***	300	17 °	35.2	$l = 1$ mm $w = 0.5$ mm

\*: Slow large rectangular microscanner; \*\*: Fast circular microscanners;  
\*\*\*: Very fast rectangular microscanners

**Figure 57: Table representing different attributes of tested scanning mirrors.**

We plot the normalized response of several different scanners to show how rapidly the deflection angle falls off as the frequency is swept away from the resonant frequency (**Figure 58**). This high Q is good for obtaining large amplitude deflections, but also requires that frequency tuning be used to maintain the scanner at a high amplitude of deflection. The resonant frequencies of the scanners will be sensitive to process and environmental variations furthering the importance of metrology for accurate calibration of microscanners.

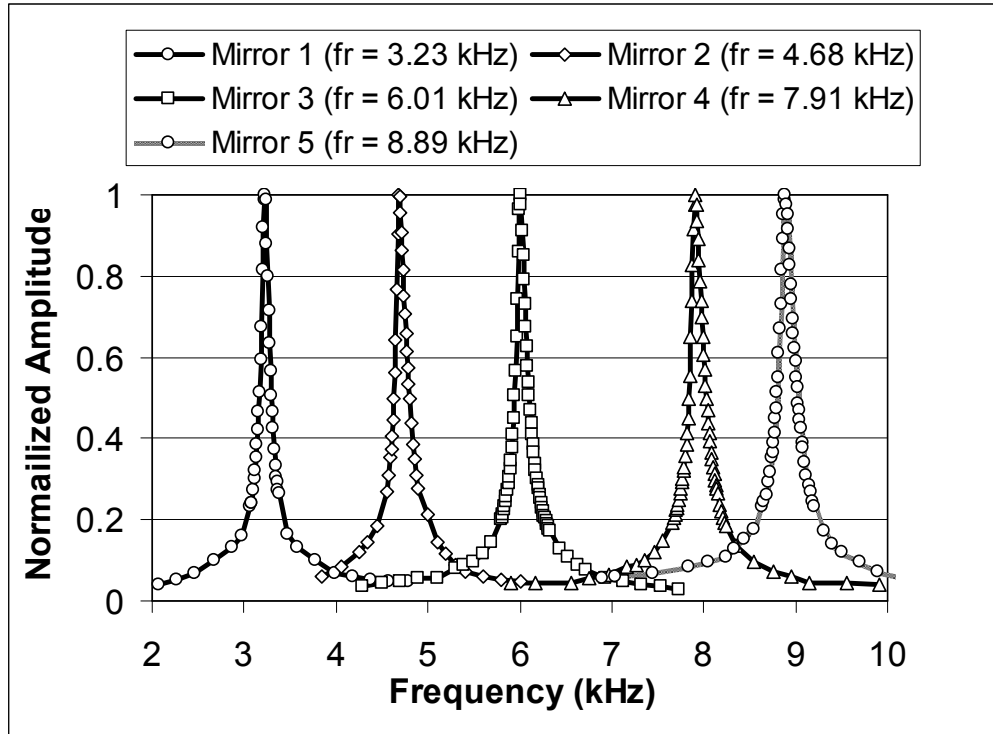
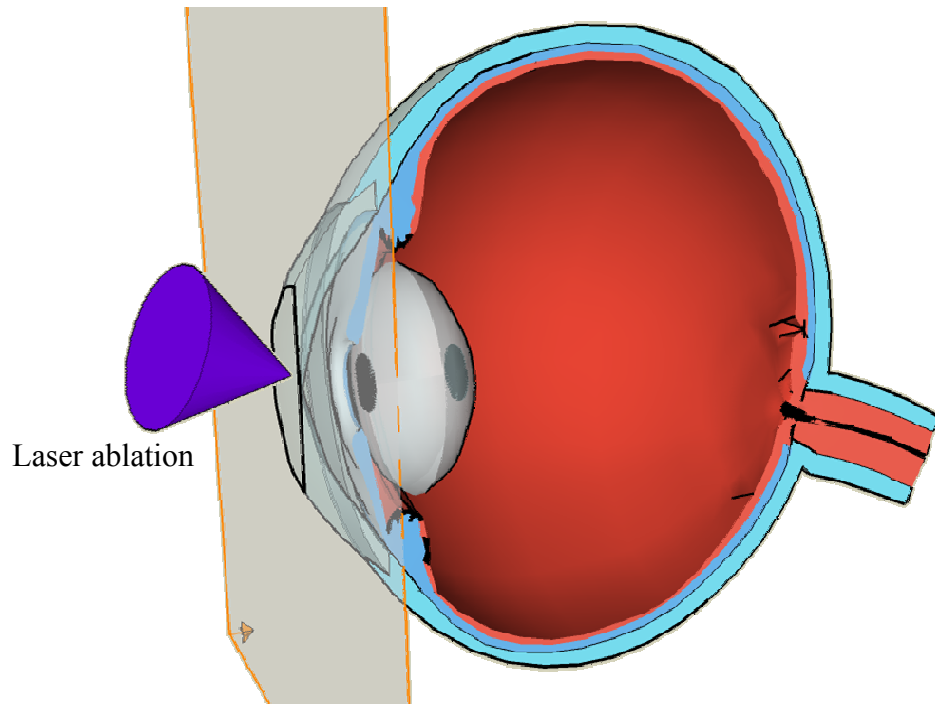
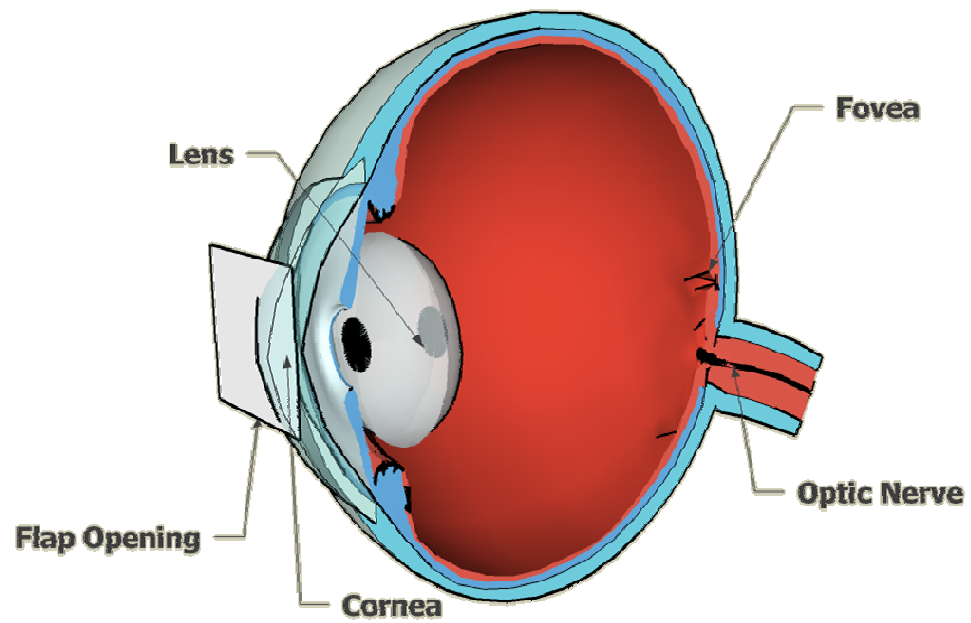


Figure 58: Scanning magnitude of the mirrors.

## 7.5 Application of the Torsional Microscanner to Refractive Laser Surgery

We tested the mirrors for the possible application of refractive laser surgery of the ocular cornea. In ocular cornea surgery, an excimer laser with a wavelength around 200 nm is used to ablate the surface of the eye to correct optical aberrations (**Figure 59**). In order to be suitable for this application, the scanners should be able to steer fast enough to correct for the natural twitching of the eye and should be highly accurate.



**Figure 59: Ocular refractive surgery: a flap of tissue is removed from the cornea and the underlying area is ablated with an excimer laser to reshape the surface and correct the vision.<sup>7</sup>**

<sup>7</sup> Parts of this image were produced with Google SketchUp by an anonymous user: [www.google.com](http://www.google.com)

When pulsing the laser, a portion of the beam carrying energy higher than  $50 \text{ mJ/cm}^2$  causes the material in the cornea to ablate to a depth proportional to the logarithm of the light intensity. By repeatedly scanning the laser over the surface and ablating in precise locations, the cornea can be reshaped to produce the appropriate focus (**Figure 60**).

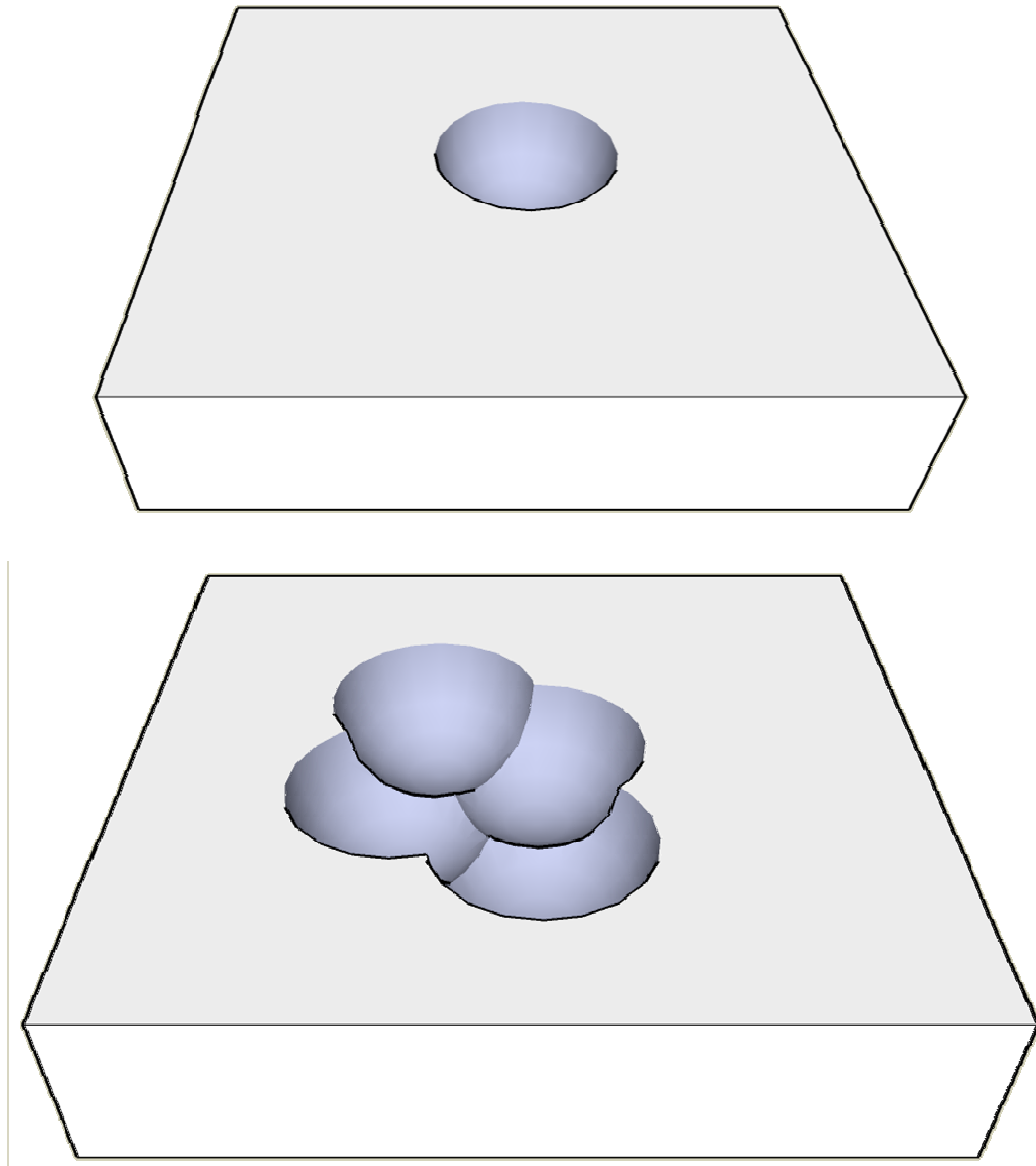


**Figure 60: A single ablation (top) and multiple ablations (bottom): by using many ablations in the appropriate spots, the eye surface may be reshaped to correct vision.**

The process for scanning a pattern onto the cornea consists of a two-part process that includes the setup and calibration of the scanner and then the scanning of the image. Our experimental setup is shown in **(Figure 61)**. A pulsed 660 nm laser diode is collimated against two scanning mirrors of the same resonant frequency and steered into a CCD imager to simulate the cornea. The intensity of the registered laser pulse is recorded by the CCD and used to determine the effective ablation depth on the human cornea had the laser been an excimer laser and the CCD been the patient's cornea. The two mirrors with resonant frequencies at 6.01 kHz, which are oriented at right angles with respect to each other, are driven with sinusoidal voltages that are 90° out of phase with each another. By varying the amplitude of the driving signal and the time-delay of the pulse, the pattern can be mapped out onto the cornea. The time-delay of the pulse is achieved through a delay pulse-generator (DG535). Circular scanning allows the geometry of the cornea to be well matched and greater precision to be used near the center of the cornea where this detail is needed.

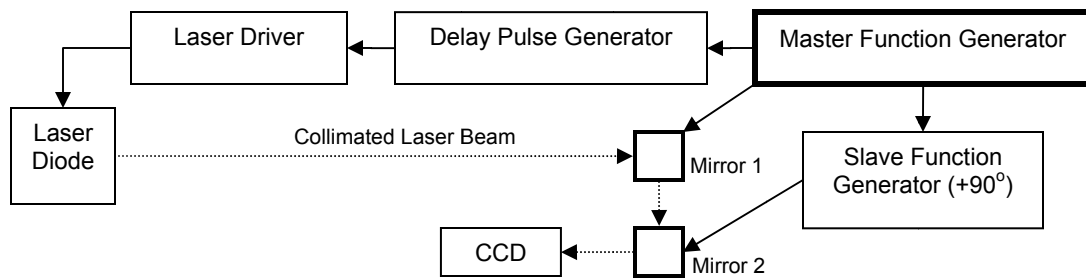
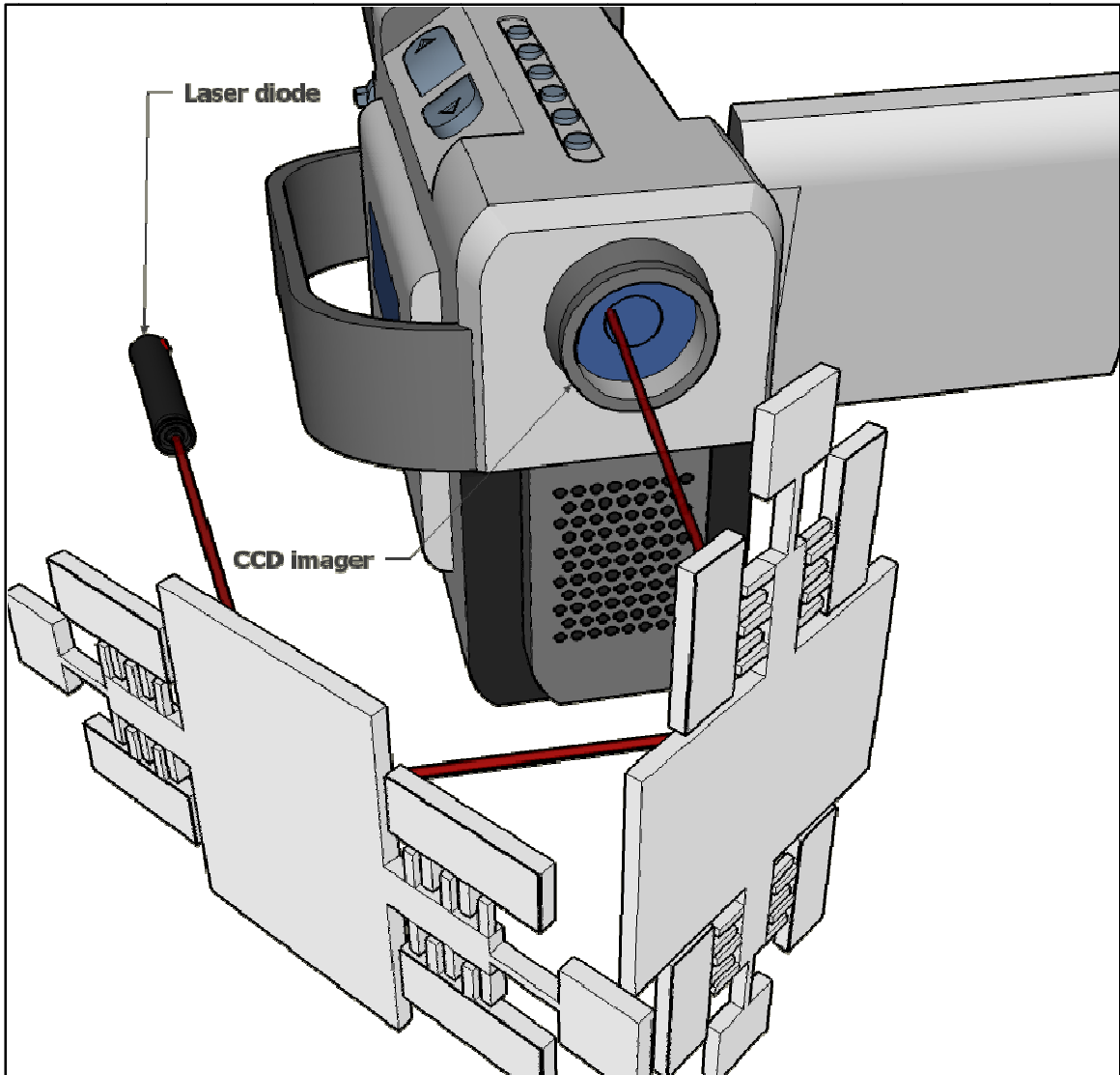


**Figure 61: Laser-scanning experimental setup showing the physical device setup (top) and system setup (bottom).**

We calibrated the scanning of the specified ablation pattern by producing a mapping of the time-delay and amplitude values that are required to drive the scanners and the pulse

generator with x and y pixel locations on the CCD imager. This method was the easiest way to calibrate the scanner. The calibration pattern was a sequence of circles. In order to save time, unknown time-delays and voltage amplitudes were interpolated with a cubic interpolation function.

We measured with the CCD imager the diameter (full width at half maximum) of the laser spots generated by the 660 nm laser diode to be 220  $\mu\text{m}$  on average.

For continuous operation of the laser ablation process which can last up to half an hour, stability of the laser's position and diameter is important and was measured at various locations about the simulated cornea. The standard deviation of the position of the pulse was measured to be less than 0.56  $\mu\text{m}$ . The standard deviation of the diameter of the pulse was measured to be less than 0.68  $\mu\text{m}$ .

For demonstrating the surface-ablation process, we chose to ablate the pattern of the ear of Roosevelt on the US dime as the size is similar to the area of ablation on the cornea of the eye (**Figure 62**). The topology of the ablation was determined by measuring the dime under a white-light interferometer (WYKO NT3300). The height information was encoded in a gray-scale image, the gray value scaled proportionally to the depth of desired ablation. For producing the desired depth of ablation, the depth of desired ablation was divided by the depth of single ablation to determine the total number of ablations needed per pixel.

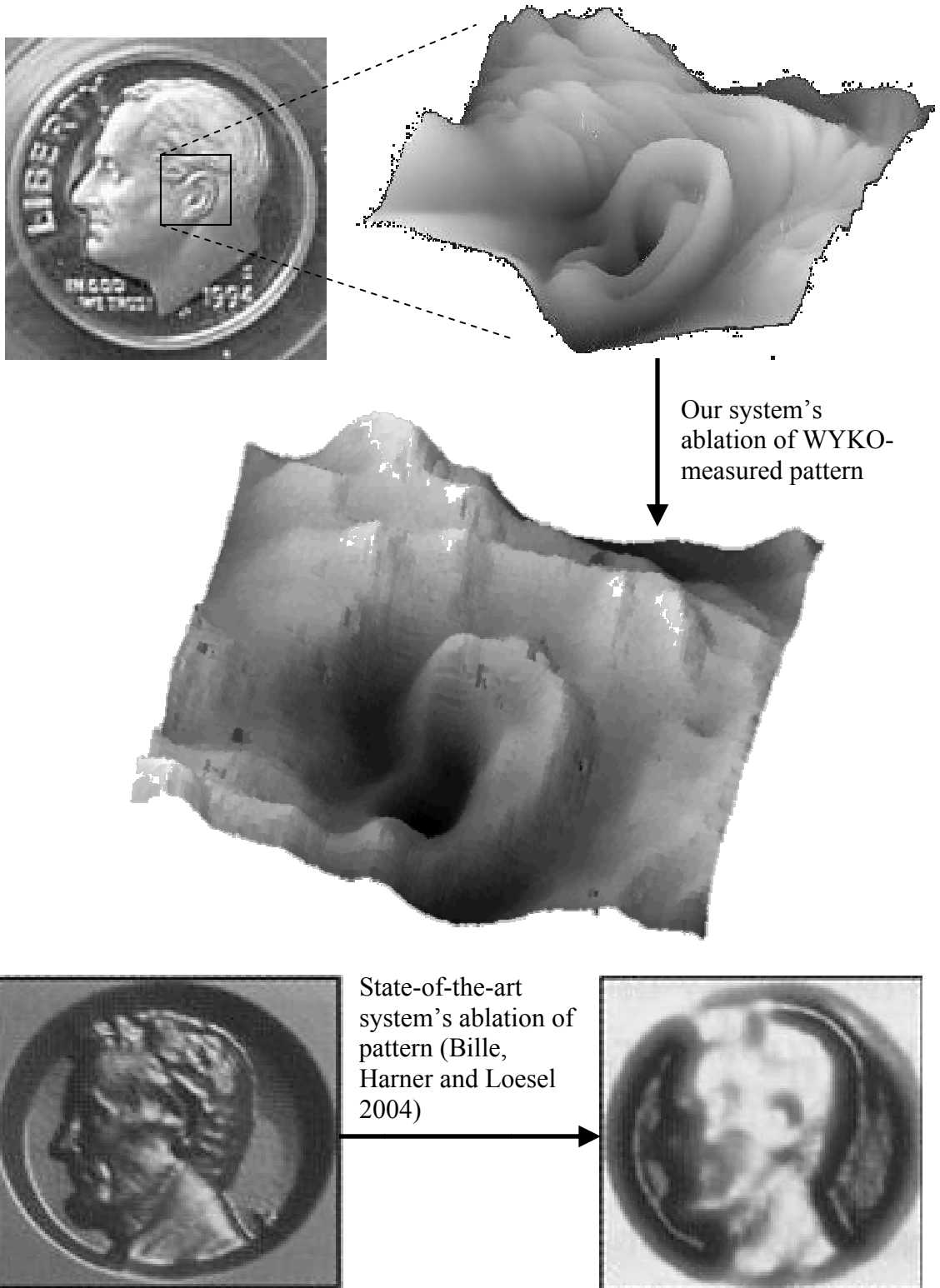


**Figure 62: Comparison of ablating an image from a dime with our setup (top) vs. ablating an image of a penny with a state-of-the-art setup (bottom).**

The quality of ablation using our microscanners is sufficient (if not better) than a state-of-the-art ablation system. The maximum deviation of the simulated ablation pattern from the desired ablation pattern is less than 35 microns.

## 7.6 Conclusions

We have designed, fabricated, and tested microscanners using our new fabrication techniques. The process uses well-developed integrated-circuit processing tools, and is simple, high-yielding, and reliable. The major advance in our fabrication process results from its straightforward method to produce vertically offset comb pairs that provide for robust electrostatic drive of torsion-bar suspensions. In practice, we achieve uniform offset-heights for vertical comb fingers processed across the 10-cm wafers. We have produced microscanners having resonant frequencies ranging from 50 Hz to 24 kHz having OSA values typically approximating  $20^\circ$  but varying from  $8$  to  $48^\circ$ . The actuation voltages required were from 14.1 to  $67.2 V_{ac\_rms}$ .

A 2-D scanning system, built using these microscanners, produced emulated ablation patterns that compare favorably to results published by researchers to illustrate the performance of a state-of-the-art macro-scale ablative surgery system.

# Chapter 8: MEMS Metrology Applied to Enable Levitated Accelerometry

In the past, stable levitation of proof masses has been achieved through numerous methods, including acoustic (Ueha, Hashimoto and Koike 2000), optical (Gauthier and Wallace 1995), aerodynamic, electrostatic (Toda, et al. 2002), magnetic (Simon, Heflinger and Ridgway 1997), and diamagnetic (Berry and Geim 1997). Whereas most of these techniques result in spurious vibrations in order to achieve levitation, this chapter presents the theory and verification for a low power, MEMS-based, diamagnetically levitated proof mass. Section 8.1 motivates the importance of using a levitated accelerometer for measuring vibrations that occur at low-frequencies ( $<10$  Hz). Section 8.2 examines the diamagnetic force and produces a concise formula for the levitation of a rectangular plate above checkerboard configurations of magnets. Section 8.3 uses the metrology techniques of Chapters 3 and 4 to produce proof-of-concept measurements of the levitated accelerometer. We have built a levitated proof-mass device and obtained experimental results that show electrostatic-measurement sensitivity of  $34 \mu\text{g}$  at a  $0.1$  V sense signal and interferometer-measurement sensitivity of  $6 \mu\text{g}$ . The measurements are targeting  $5\text{Hz}$  vibrations. An ADXL 203<sup>8</sup>, a commercial MEMS accelerometer, achieves  $285 \mu\text{g}$  for the same vibrations. Section 8.4 details how our accelerometer may be manufactured in bulk. This work is based on our publication (Garmire et al. 2007).

## 8.1. Equations of Motion

---

<sup>8</sup> <http://www.analog.com/en/prod/0,2877,ADXL203,00.html>

We show that a slightly damped, non-stiff suspension has a better precision for measuring low-frequency vibrations than a stiff suspension typically found in MEMS. Diamagnetic levitation provides MEMS devices with the means to create such optimized suspensions.

The 1D mechanical theory for accelerator response is formulated in Eq. 23. Calling  $x$  the target displacement, the acceleration,  $\ddot{x}(t)$ , is:

$$\ddot{x}(t) = -\frac{1}{M}(D\dot{z}(t) + Kz(t)) - \ddot{z}(t) \quad \text{Eq. 23}$$

where  $y(t)$  is the proof-mass position,  $z(t) = y(t)-x(t)$  is the measured displacement, and  $M$ ,  $D$ , and  $K$  are the mass, damping, and stiffness of the system. We simulate the response of this system on a  $10 \mu\text{g}$  sinusoidal excitation over frequencies ranging from 0.1 Hz to 10 Hz (**Figure 63**). The noise of the position detector is simulated to have a standard deviation of 1 nm sampling at 500 Hz. This simulated noise in the measurement of the position detector is the sole contributor to the plotted standard deviation of the error in the acceleration measurement. An interesting result is that monitoring with an isolated proof mass (isolated monitoring) is not as good as monitoring with a suspended but highly damped proof mass (damped monitoring) at low frequencies. This result is likely due to the fact that isolated monitoring relies on a second derivative of motion whereas damped monitoring relies only on a first derivative of motion. Our manufactured device shown later has  $K/M = 158 \text{ Hz}^2$  and  $D/M = 73 \text{ Hz}$ .

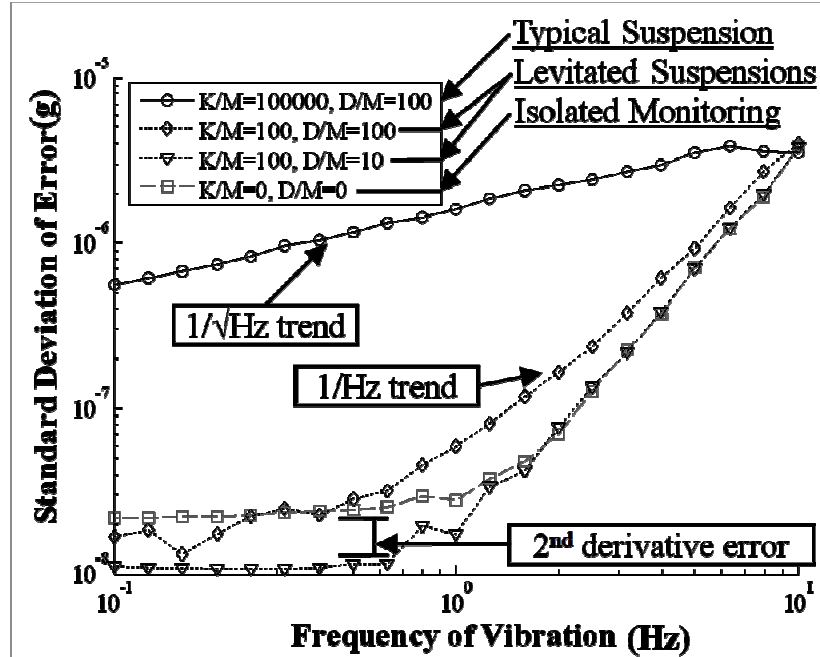


Figure 63: The accuracy of accelerometers using four different suspensions is measured by finding the standard deviation of the suspension response compared to a sinusoidal input at each frequency.

## 8.2. Diamagnetic Force

Using Fourier analysis and Taylor series expansions applied to the diamagnetic governing equations of a square piece of graphite above a checkerboard configuration of magnets (Figure 64), we derive Eq. 24 which approximates the plate levitation height,  $z$ , when the proof-mass weight balances the diamagnetic force (the derivation of this equation is included in the appendix):

$$h_{\text{total}}\rho g \approx 0.0123 \frac{\chi}{\mu_0} B^2 \left( \frac{h_{\text{graphite}}w}{(z+h_{\text{graphite}})z} \right) \quad \text{Eq. 24}$$

where  $h_{\text{total}}$  is the total plate thickness,  $\rho$  is the plate density ( $2300 \text{ kg/m}^3$ ),  $g$  is  $9.8 \text{ m/s}^2$ ,  $\chi$  is graphite's magnetic susceptibility ( $450 \times 10^{-6}$ ),  $\mu_0$  is  $4\pi \times 10^{-7} \text{ N}\cdot\text{A}^{-2}$ ,  $B$  is the magnetic flux density (1 Tesla for NdFeB),  $w \times w$  is the magnet size ( $100 \mu\text{m} \times 100 \mu\text{m}$ ), and

$h_{\text{graphite}}$  is the graphite-layer thickness. We experimentally validate this approximation in the next section.

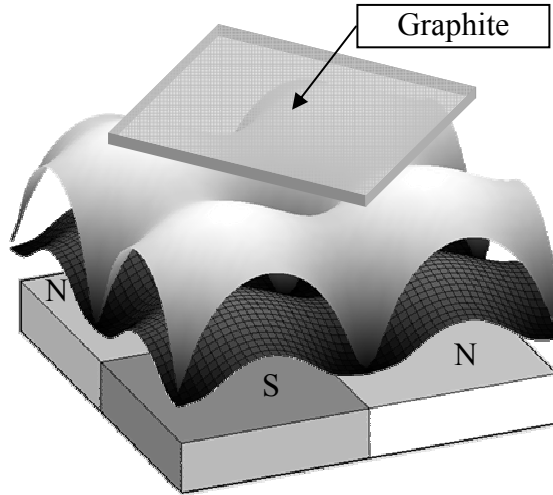


**Figure 64:** Two equipotential surfaces of the diamagnetic field above alternating north-pole and south-pole magnets (potential increases closer to the magnets).

### 8.2.1 Diamagnetic Force Experimental Validation

We verify the formula (Eq. 24) to use for our levitated accelerometer design by placing weights onto a levitated piece of pyrolytic graphite ( $7.7 \times 10^{-5}$  N) while monitoring the vertical displacement through a side-mounted microscope (**Figure 65a**). We reduce tilting of the proof mass by positioning the weight while monitoring the angular change of a reflected laser beam. We also compare adding additional pieces of pyrolytic graphite (**Figure 65b**).

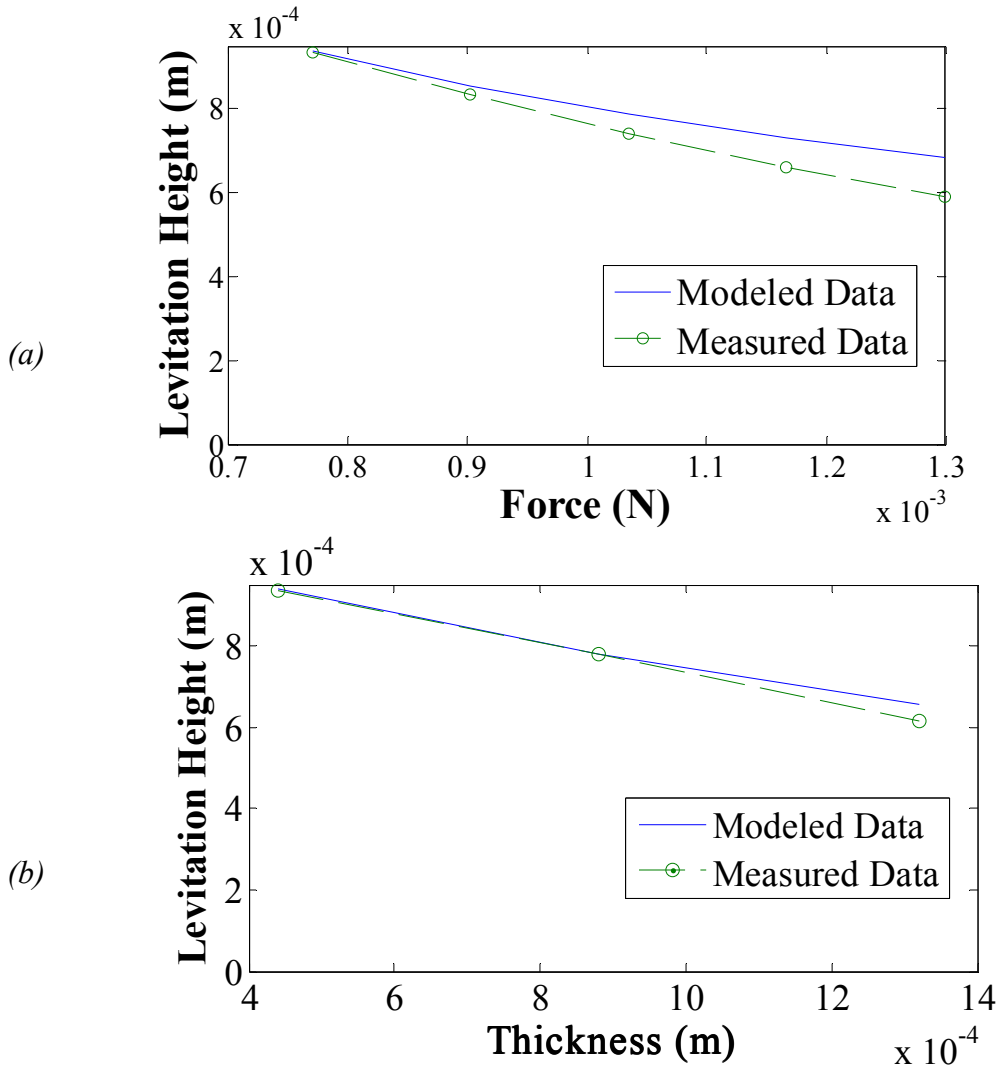


Figure 65: We use Eq. 24 to predict the levitation height of the proof mass (a) under load and (b) with varying thicknesses of graphite.

### 8.3. Proof-of-Concept Results

To test the MEMS levitated accelerometer, we mount a fabricated SOI proof mass to several layers of pyrolytic graphite. We levitate it above NdFeB magnets and align the electrostatic-sensing combs to it using a 3-axis stage (Figure 66). We directly compare the response of a levitated accelerometer to the response of the ADXL 203 accelerometer subject to small impulses applied to the whole table (Figure 66). We reflect a laser beam

off of the proof mass and record its position on a CCD image sensor to measure out-of-plane tilting motions of the plate (**Figure 65**). The tilting motion determines whether coupling happens between the lateral motion and the out-of-plane motion. The lateral motion quickly dies away due to damping. After the tilting motion dies away, we should be measuring only the lateral motion from the vertically offset comb-drives. By processing the results using off-chip circuitry, we show that the noise level of the electrostatically-sensed levitated accelerometer is at least a factor of 12 smaller than the noise level of the ADXL 203 using only 0.1V for the differential sense (specific results are at 5 Hz). Upon excitation of the air table, a high-frequency, 40 Hz coupling is evident in the accelerometer (higher frequency peaks in **Figure 67a**) but lessens as the out-of-plane motion dies away. By packing more magnets under the levitated proof-mass, this tilting mode can be further mitigated.

At rest, the standard deviation of the ADXL vs. the levitated accelerometer is 285  $\mu\text{g}$  vs. 34  $\mu\text{g}$  using a 0.1 V sense signal for samples averaged over 0.1 seconds. Note that the noise of the detector scales with the applied sense voltage. A 0.34  $\mu\text{g}$  detector is possible at a 10 V applied signal if the voltage output can be adjusted to see the full range of capacitance change. On-chip circuitry will further improve this sensitivity.

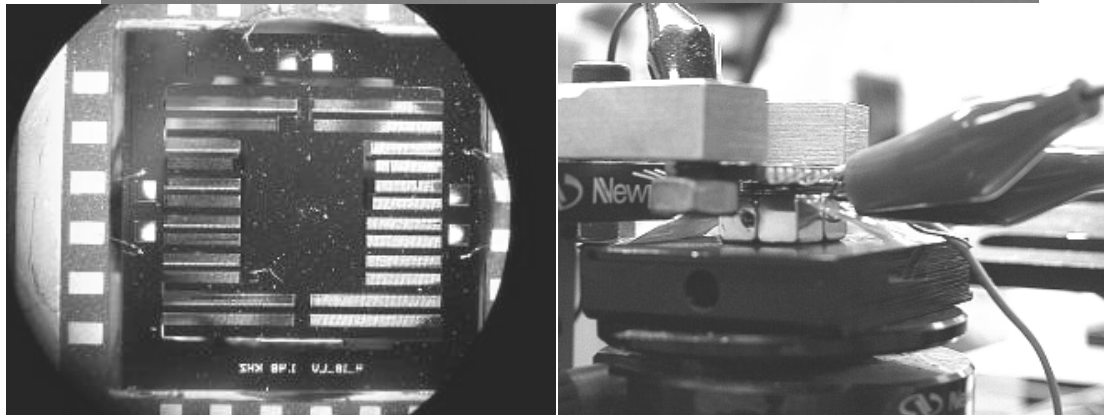
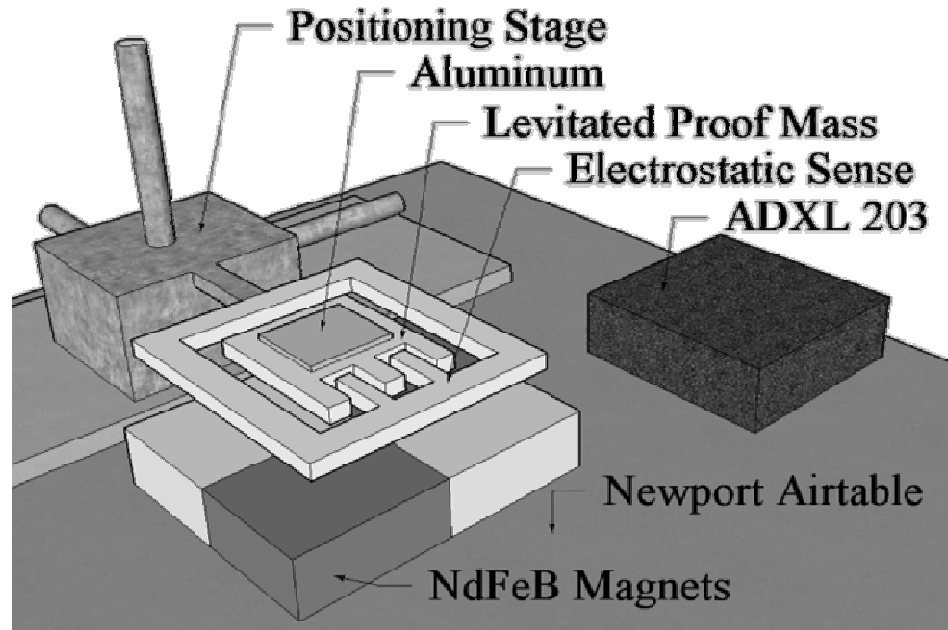


**Figure 66: Schematic of experimental setup (top); microscope photo of levitated proof mass (bottom left); the magnets under the levitated proof mass (bottom right).**

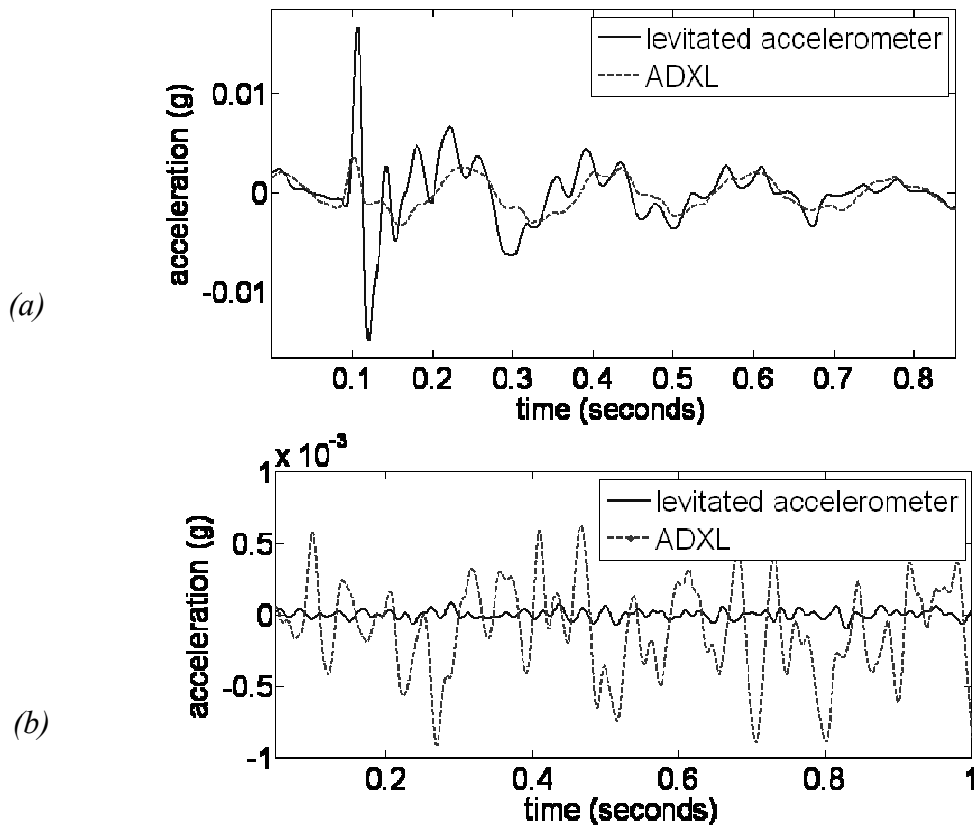


Figure 67: Comparison of an ADXL 203 and the levitated accelerometer excited (a) and at rest (b).

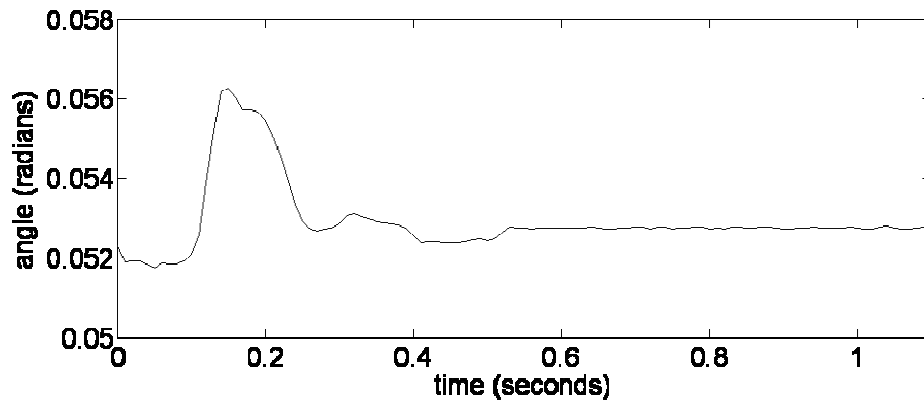
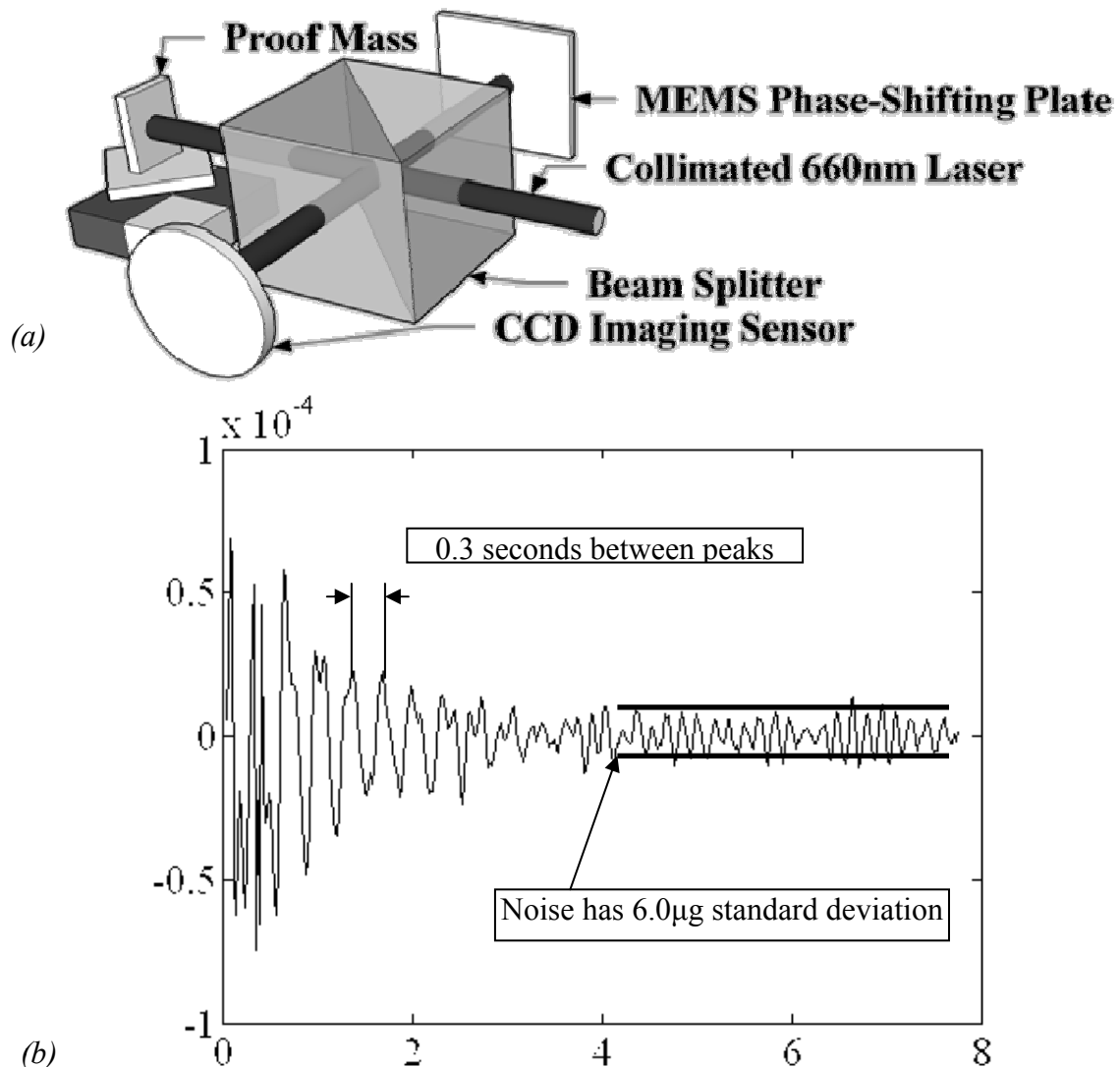


Figure 68: Tilt of levitated proof mass that shows some out-of-plane effects in the first 0.4 seconds.

Next, we examine the motion of a diamagnetic proof-mass ( $D/M = 73$  Hz,  $K/M = 158$  Hz<sup>2</sup>) using a fast phase-shifting interferometer that is based on vibrating a MEMS plate to

achieve rapid phase-shifting and therefore a high sampling rate (50 Hz) (**Figure 69**). We use a Fisher Scientific U56001 vibration generator to supply a 1.6 N impulse to the 300 Kg Newport air table. From the response measured by the levitated accelerometer (**Figure 69**), we are able to determine the table's suspension values,  $K/M \approx 438 \text{ Hz}^2$  and  $D/M \approx 2.3 \text{ Hz}$ . The noise in the system has a standard deviation of  $6.0\mu\text{g}$ , not the limit of the detector but the limit of isolating the table from surrounding vibrations.



**Figure 69:** The fast phase-shifted interferometer (a) measures the acceleration (b) of the 300 kg air table after a 1.6 N impulse is applied to it.

## 8.4. Ideal Fabrication and Design

We show the feasibility of a MEMS process to fabricate a levitated accelerometer with the necessary levitation height and dynamic properties. Evaluating Eq. 24, we calculate a levitation height of 26  $\mu\text{m}$  for a 2  $\mu\text{m}$ -thick pyrolytic graphite layer (Kostecki, et al. 2001) on top of a 20  $\mu\text{m}$ -thick silicon plate with square magnets (100  $\mu\text{m}$  on a side) fabricated on the substrate. The magnet arrays can be made separately and bonded to the device to reduce complexity. Thus, the plate is separated by a 6  $\mu\text{m}$ -gap from the substrate and magnets. Depositing a 0.122  $\mu\text{m}$  layer of aluminum on top of the plate results in damping of  $D/M = c B^2/\rho h_{aluminum}/h_{total} = 100 \text{ Hz}$ , where  $c$  is aluminum's conductivity ( $37.7 \times 10^6$  /ohm m).

**Figure 70** shows a conceptual view of a processed device made directly in SOI. The magnets can be grown separately and placed in a backside trench or opening. Additional magnets should be placed above to keep the proof mass in place during the release of the proof mass from its surrounding, and lessen out-of-plane tilting effects during operation.

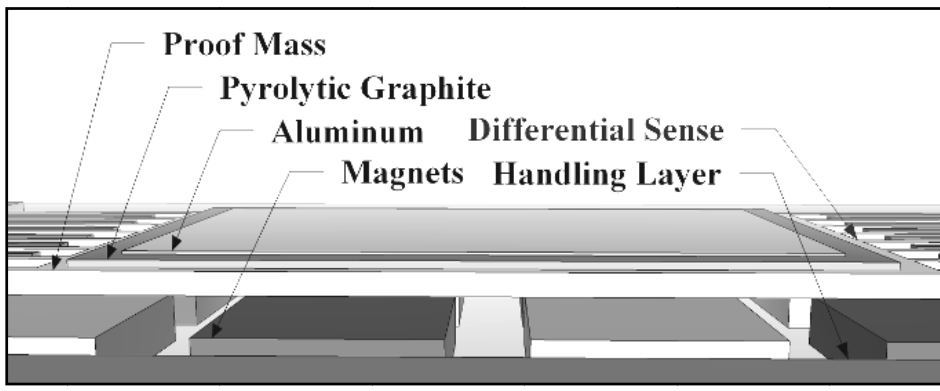
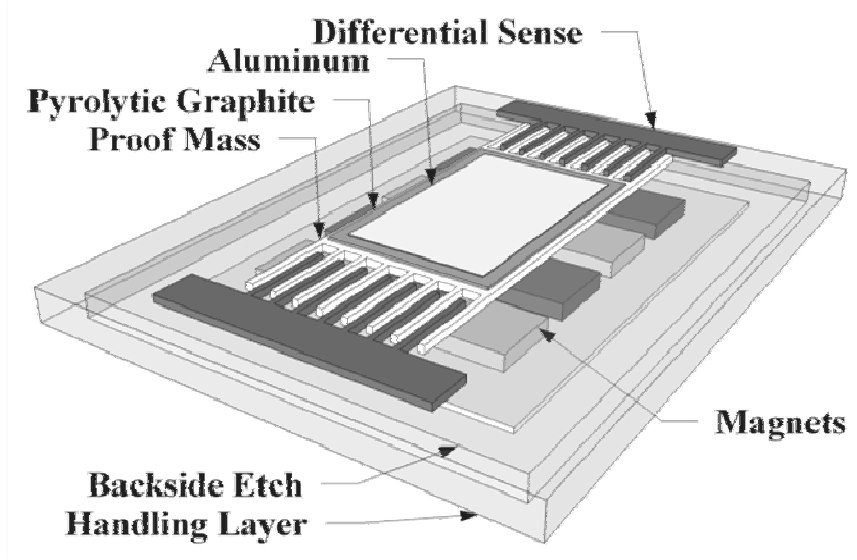


**Figure 70: The levitated proof mass construction.**

Differential comb-drives are used in electrostatic sensing for accurately determining position. Differential vertical-offset combs can be fabricated directly in SOI to electrostatically resolve out-of-plane motion (Figure 71).

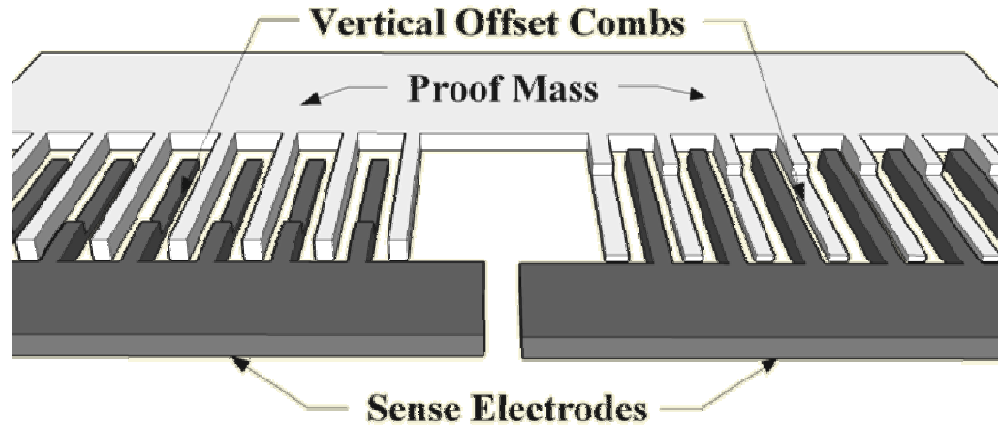


**Figure 71: Vertical sensing using offset combs.**

The levitated accelerometer can be designed to use either electrostatic sensing or interferometric sensing. As demonstrated, using fast phase-shifting interferometer techniques, we can inexpensively and rapidly monitor lateral motion at a rate of above 100 Hz with a precision down to 2 nm per frame. With the invention of a fast phase-shifting component, the interferometer can also be reduced in size through a simplification of the driving power-supply components.

## 8.6. Conclusions

This research addresses a need for highly sensitive, low-cost, low-frequency accelerometers in fields such as earthquake monitoring, vehicle navigation using dead reckoning, and in deterioration of bridges and other structures. The low-cost nature of MEMS and the high sensitivity of diamagnetically levitated MEMS accelerometers will allow the deployment of large arrays of accelerometers to resolve the origin and propagation of low-frequency waves.

## Chapter 9: Conclusion

As the size of MEMS become smaller due to improvements of photolithography and processing, more devices fit onto a single chip, lowering the cost of each device. At the same time, variability in the processing of smaller structures has a larger impact on their operation. The unavoidable result is that more device testing needs to be done on a smaller scale and more testing needs to be done per unit area. In order for MEMS to be cost-effective, methods need to be developed that will automate this wafer-level test and measurement of MEMS. Furthermore, the functionality of MEMS devices is expanding specifically to include out-of-plane electrostatic actuation methods and metrology methods must address this added functionality to expand the usefulness of MEMS in fields that will use this added functionality.

We have demonstrated the use of metrology, both optical and electrical, as a means to rapidly test devices and alleviate this dilemma. In the optical metrology domain, we have created a way for teleoperated testing of components and matching simulation with physical devices during the operation of those devices. In the electrical metrology domain, we have created new devices for accurately measuring key parameters using simple circuitry. These electrical probing techniques are reusable, inexpensive to implement, consume only a small amount of area, and are highly accurate exceeding the accuracy of purely optical methods. These methods will allow for the reliable production of MEMS at smaller scales and pave the way for future scaling of MEMS in size and adapting of MEMS to more variable processes such as printed MEMS.

In addition to our core work on metrology, we have also expanded the types of MEMS possible by developing a photolithographic process to create vertically-offset comb-drives. The additional dimension of motion allows a myriad of types of devices to be possible including devices we have thought about and developed like deformable mirrors and twist-up structures. However, metrology plays just as an important role in this type of MEMS device with the added challenge that it must be able to calibrate the out-of-plane motions. We have presented additional procedures and experiments for measuring out-of-plane forces and changes.

As an application of this metrology work, we have characterized the motion of a MEMS-based phase-shifting interferometer component. This characterization allows us to achieve under 2 nm rms noise per pixel for unwrapped heightmaps that are produced at a rate of up to 300 Hz. Further work in this area will allow for *in situ* monitoring of biological specimens, finely detailed studies of crystal growth and surface reflow from thermal annealing, and further examination of MEMS processing characteristics such as with printed MEMS.

We also demonstrated torsional microscanners that may be applied to a wide variety of problems ranging from portable projectors to corneal laser surgery systems. For these microscanners, we demonstrated optical scanning angles up to 48° with 67.2 V actuation and frequencies up to 24 kHz. We showed circular raster scanning as a way of using mirrors with the same resonant frequency to still obtain a scanned image. We showed a way of calibrating this scanning technique and adapting it to variations in the scanner

performance. Finally, we demonstrated the use of microscanners in corneal laser surgery systems by ablating the pattern from the US Dime to a depth accuracy of 35 microns.

Lastly, we achieved the first demonstration of diamagnetic levitation as a means for high-accuracy, low-cost, accelerometers to measure vibrations in the seismic frequency range. We applied both optical and electrostatic metrology techniques to these measurements. Electrostatically, we were able to achieve 36  $\mu\text{g}$  resolution for a 5 Hz frequency of vibration. Using our fast phase-shifting interferometer, we were able to achieve 6  $\mu\text{g}$  resolution for vibrations ranging from 10 Hz to 0.1 Hz in frequency.

There is little doubt that optical and electrostatic metrology methods will continue to affect the applicability of MEMS to different fields as well as reduce the overall cost while improving process capabilities and resulting device performance. The research contained in this thesis is meant as a start along this path. Through successful integration into the industrial setting, metrological devices and techniques, as presented here, will bring the usefulness of MEMS to the broader markets.

## Bibliography

- Afghahi, M. Integrated CMOS Imager. US Patent 985,838 . June 8, 2004.
- Baidya, B., S. K. Gupta, and T. Mukherjee. "An Extraction-Based Verification Methodology of MEMS." *Journal of Microelectromechanical Systems* 11, no. 1 (February 2002): 2-11.
- Berry, M. V., and A. K. Geim. "Of flying frogs and levitrons." *Eur. J. Phys.* 18 (1997): 307-313.
- Bille, J. F., C. F. H. Harner, and F. H. Loesel. *Aberration-Free Refractive Surgery*. 2nd Edition. New York, USA: Springer-Verlag, 2004.
- Boser, B. E. "RF Analog-to-Digital Converters; Sensor and Actuator Interfaces; Low-Noise Oscillators, PLLs and Synthesizers." Edited by R. J. van de Plassche, J. H. Huijsing and W. M. C. Sansen. Kluwer Academic Publishers, 1997.
- Burgwald, G. M., and W. P. Kruger. "An Instant-on Laser for Distance Measurement." *Hewlett-Packard Journal*, 1970: 14.
- Candler, R. N., et al. "Single Wafer Encapsulation of MEMS Devices." *IEEE Transactions on Advanced Packaging* 26, no. 3 (August 2003): 227-232.
- Canny, J. "A Computational Approach to Edge Detection." *IEEE Transactions on Pattern Analysis and Machine Intelligence* 8, no. 6 (1986): 679-698.
- Cao, L., T. S. Kim, S. C. Mantell, and D. L. Polla. "Simulation and Fabrication of Piezoresistive Membrane Type MEMS Strain Sensors." *Sensors and Actuators A.: Physical* (Elsevier) 80, no. 3 (March 2000).

- Carley, L. R., G. R. Ganger, and D. F. Nagle. "MEMS-based Integrated-Circuit Mass-Storage Systems." *Communications of the ACM* 43, no. 11 (2000): 72-80.
- Chan, E. K., K. Garikipati, and R. W. Dutton. *Comprehensive Characterization of Electrostatically-Actuated Beams*. 1999. <http://citeseer.ist.psu.edu/407250.html>.
- Choo, H. *Devices, Structures, and Processes for Optical MEMS*. PhD Thesis, Berkeley, CA: UC Berkeley, 2007.
- Choo, H., and R. S Muller. "Devices, Structures, and Processes for Optical MEMS." *Special Issue on IEEJ Transactions of Electrical and Electronic Engineering 2* (May 2007): 216-232.
- Choo, H., and R. S. Muller. "Optical Properties of Microlenses Fabricated Using Hydrophobic Effects and Polymer-Jet-Printing Technology." *2003 IEEE/LEOS International Conference on Optical MEMS and Their Applications*. Kona, Hawaii USA , 2003. 169-170.
- Choo, H., D. Garmire, J. Demmel, and R. S. Muller. "A simple process to fabricate self-aligned, high-performance torsional microscanners: demonstrated use in a two-dimensional scanner." *IEEE/LEOS Optical MEMS*. 2005. 21-22.
- Choo, H., D. Garmire, J. Demmel, and R. S. Muller. *CMOS-Compatible High-Performance Microscanners, Including Structures, High-Yield Simplified Fabrication Methods and Applications*. 2005.
- . "Simple Fabrication Process for Self-Aligned, High-Performance Microscanners; Demonstrated Use to Generate a Two-Dimensional Ablation Pattern." *Journal of Microelectromechanical Systems*, April 2007.

- Choo, H., D. Garmire, R. S. Muller, and R. Kant. MEMS-Based Phase-Shifting Interferometer. 2006.
- Choo, H., R. Kant, D. Garmire, J. Demmel, and R. S. Muller. "Fast, MEMS-based Phase-Shifting Interferometer." *Hilton Head Solid-State Sensor and Actuator Workshop 2000*. Hilton Head, South Carolina, USA, June 2006. 94-95.
- . "MEMS-Based, Phase-Shifting Interferometer." *Solid-State Sensor and Actuator Workshop*. Hilton Head, SC, 2006. 94-95.
- Clark, J. V. *Electro Micro-Metrology*. PhD Thesis, Berkeley, CA: UC Berkeley, 2005.
- Clark, J. V., D. Garmire, M. Last, and J. Demmel. "Practical Techniques for Measuring MEMS Properties." *Nanotech 2004*. 2004. 402-405.
- Clark, J. V., et al. "3D MEMS Simulation Modeling Using Modified Nodal Analysis." *Proceedings of the Microscale Systems: Mechanics and Measurements Symposium*. Orlando, FL, USA, 2000. 68-75.
- Conant, R. A., J. T. Nee, K. Y. Lau, and R. S. Muller. "A flat high-frequency scanning micromirror." *Hilton Head Solid-State Sensor and Actuator Workshop 2000*. Hilton Head, South Carolina, USA, June 2000. 6-9.
- Conant, R. *Micromachined Mirrors*. PhD Thesis, Berkeley, CA: UC Berkeley, 2002.
- Crowell, B. *Vibrations and Waves*. Light and Matter, 2002.
- Damrongsak, B., and M. Kraft. "Electrostatic suspension control for micromachined inertial sensors employing a levitated-disk proof mass." *MME 2005 Conference*. Sept. 2005. 240-243.
- Diamond, B. M., J. J. Neumann, and K. J. Gabriel. "Digital Sound Reconstruction Using Arrays of CMOS-MEMS Microspeakers." *TRANSDUCERS, 12th International*

- Conference on Solid-State Sensors, Actuators, and Microsystems*. IEEE Xplore, June 2003. 238-241.
- Fang, W., and J. A. Wickert. "Determining Mean and Gradient Residual Stresses in Thin Films Using Micromachined Cantilevers." *J. Micromech. Microeng.* 6 (1996): 301-309.
- Farrell, P. V., G. S. Springer, and C. M. Vest. "Heterodyne Holographic Interferometry - Concentration and Temperature Measurements in Gas Mixtures." *Applied Optics*, May 1982: 1624-1627.
- Forsyth, D. A., and J. Ponce. *Computer Vision: A Modern Approach*. Prentice Hall, 2002.
- Garmire, D., et al. "Diamagnetically Levitated MEMS Accelerometers." *Transducers 2007*. Lyon, France, 2007.
- Garmire, D., H. Choo, R. S. Muller, S. Govindjee, and J. Demmel. Integrated MEMS Metrology Device using Complementary Measuring Combs. USA Patent Pending. 2006.
- . "MEMS Process Characterization with an on-Chip Device." *Nanotech 2006, The Technical Proceedings of the Nano Science and Technology Institute*. Boston, MA, May 2006. 550-553.
- Garmire, D., R. S. Muller, and J. Demmel. "Vision-based Teleoperation of a Stroboscopic Microscopic Interferometric System for Remote Dynamic MEMS Testing." *IEEE/LEOS International Conference on Optical MEMS 2005 and Their Applications, Technical Digest*. Oulu, Finland, August 2005. 163-164.

- Gauthier, R. C., and S. Wallace. "Optical Levitation of Spheres: Analytical Development and Numerical Computations of the Force Equations." *Journal of the Optical Society of America B*, 1995: 1680.
- Gerbe, J. P., and J. B. Migozzi. Optical system of collimation notably for helmet display unit . US Patent 5453877. 1995.
- Guckel, H. "Diagnostic Microstructures for the Measurement of Intrinsic Strain in Thin Films." *J. Micromech. Microeng.*, 1992: 86-95.
- Gupta, R. "Electronically Probed Measurements of MEMS Geometries." *Journal of Microelectromechanical Systems* 9, no. 3 (September 2000).
- Haga, Y., and M. Esashi. "Biomedical microsystems for minimally invasive diagnosis and treatment." *IEEE*. IEEE, January 2004. 98-114.
- Hariharan, P. "Phase-Stepping Interferometry with Laser Diodes 2: Effects of Laser Wavelength Modulation." *Applied Optics*, 1989: 1749.
- . "Phase-Stepping Interferometry with Laser Diodes: Effects of Changes in Laser Power with Output Wavelength." *Applied Optics*, 1989: 27.
- Hart, M. R., R. A. Conant, K. Y. Lau, and R. S. Muller. "Stroboscopic Interferometer System for Dynamic MEMS Characterization." *J. MEMS*, December 2000: 409-418.
- Hofman, U., S. Muehlmann, M. Witt, K. Dorschel, R. Schutz, and B. Wagner. "Electrostatically driven micromirrors for a miniaturized confocal laser scanning microscope." *Miniaturized Systems with Micro-Optics and MEMS*. SPIE, September 1999. 29-38.

- Hon, R. W., and C. H. Sequin. "A Guide to LSI Implementation." *Xerox Palo Alto Research Center technical memo SSL-79-7*. January 1980.
- Hung, E. S., and S. D. Senturia. "Extending the Travel Range of Analog-Tuned Electrostatic Actuators." *Journal of Microelectromechanical Systems* 8, no. 4 (December 1999): 497-505.
- Isamoto, K., K. Kato, A. Morosawa, C. Changho, H. Fujita, and H. Toshiyoshi. "A 5-V Operated MEMS Variable Optical Attenuator by SOI Bulk Micromachining." *IEEE Journal of Selected Topics in Quantum Electronics* 10, no. 3 (May 2004): 570-578.
- Jain, A., H. Qu, S. Todd, and H. Xie. "A Thermal Bimorph Micromirror with Large Bi-directional and Vertical Actuation." *Sensors and Actuators A*, 2005: 9-15.
- Jeong, J., S. Chung, S. Lee, and D. Kwon. "Evaluation of Elastic Properties and Temperature Effects in Si Thin Films Using an Electrostatic Microresonator." *Journal of Microelectromechanical Systems*, August 2003: 524-530.
- Johnson, W. A., and L. K. Warne. "Electrophysics of Micromechanical Comb Actuators." *Journal of Microelectromechanical Systems* 4, no. 1 (March 1995).
- Kamalian, R., H. Takagi, and A.M. Agogino. "Optimized Design of MEMS by Evolutionary Multi-objective Optimization with Interactive Evolutionary Computation." *2004 Genetic and Evolutionary Computation Conf., GECCO-2004*. 2004. 1030-1041.
- Kant, R., D. Garmire, H. Choo, and R. S. Muller. "Characterization of an Improved, Real-Time, MEMS-Based, Phase-Shifting Interferometer." *2007 IEEE/LEOS*

- International Conference on Optical MEMS and Their Applications*. Hualien, Taiwan, 2007. 57-58.
- Kim, J., H. Choo, L. Lin, and R. S. Muller. "Microfabricated torsional actuator using self-aligned plastic deformation." *The 12th International Conference on Solid-State Sensors, Actuators, and Microsystems -- Transducers*. Boston, MA, USA, June 2003. 1015-1018.
- Ko, Y. C., et al. "Eye-type scanning mirror with dual vertical combs for laser display." *MOEMS Display and Imaging*. SPIE, January 2005. 14-22.
- Kostecki, R., B. Schnyder, D. Alliaata, X. Song, K. Kinoshita, and R. Kotz. "Surface studies of carbon films from pyrolyzed photoresist." *Thin Solid Films* (Elsevier) 396 (September 2001): 36-43.
- Li, X., Bhushan B., Takashima K., Baek C.-W., and Kim Y.-K. "Mechanical Characterization of Micro/nanoscale Structures for MEMS/NEMS Applications." *Ultramicroscopy* 97 (2003): 481-494.
- Lieb, M., and A. Meixner. "A high numerical aperture parabolic mirror as imaging device for confocal microscopy." *Optics Express* 8, no. 9 (2001): 458-474.
- Lu, M. S.-C., and G. K. Fedder. "Position Control of Parallel-Plate Microactuators for Probe-Based Data Storage." *Journal of Microelectromechanical Systems* 13, no. 5 (2004): 759-769.
- Malacara, D., ed. *Optical Shop Testing*. 2nd Edition. New York, USA: Wiley, 1992.
- Mansell, J., and R. L. Byer. "Micromachined silicon deformable mirror." Edited by D. Bonaccini and R. K. Tyson. *Adaptive Optical System Technologies*. SPIE, 1998. 896-901.

- Markov, D. A., S. Dotson, S. Wood, and D. J. Bornhop. "Noninvasive Fluid Flow Measurements in Microfluidic Channels with Backscatter Interferometry." *Electrophoresis* (Wiley-VCH) 25, no. 21-22 (2004): 3805-3809.
- Marshall, J. C. *MEMS Length and Strain Measurements using an Optical Interferometer*. August 2, 2001. <http://www.eeel.nist.gov/812/files/NISTIR6779.pdf>.
- McCormick, D. T., and N. C. Tien. "Multiple layer asymmetric vertical comb-drive actuated trussed scanning mirrors." *IEEE/LEOS International Conference on Optical MEMS and Their Applications 2003*. Hawaii, USA: IEEE/LEOS, August 2003. 12-13.
- McKeogh, L. F., J. P. Sharpe, and K. M. Johnson. "A Low-Cost Automatic Translation and Autofocusing System for a Microscope." *Meas. Sci. Technol.* 6 (1995).
- Millerd, J. E., N. J. Brock, J. B. Hayes, M. B. North-Morris, M. Novak, and J. C. Wyant. "Pixelated Phase-Mask Dynamic Interferometer." *Interferometry XII: Techniques and Analysis*, 2004: 304-314.
- Miyajima, H., M. Nishio, Y. Kamiya, M. Ogata, and Y. Sakai. "Development of two dimensional scanner-on-scanner for confocal laser scanning microscope LEXT series." *IEEE/LEOS International Conference on Optical MEMS and Their Applications 2005*. Oulu, Finland: IEEE/LEOS, August 2005. 23-24.
- Mrochen, M. "Converting wavefronts into corrections." *3rd International Congress of Wavefront Sensing and Aberration-free Refractive Correction*, February 2002.
- Muthuswamy, J., M. Okandan, T. Jain, and A. Gilletti. "Electrostatic Microactuators for Precise Positioning of Neural Microelectrodes." *IEEE Transactions on Biomedical Engineering* 52, no. 10 (October 2005): 1748-1755.

- Nakadate, S., and I. Yamaguchi. Japan Patent H02-287107.
- Nakajima, T. "Sensitivity of Ground-based Infrared Interferometer for Aperture Synthesis Imaging." *Publications of the Astronomical Society of the Pacific*, 2001: 1289-1299.
- Novak, E. "MEMS Metrology Techniques." Edited by D. M. Tanner and R. Ramesham. *Proceedings of SPIE -- Volume 5716 Reliability, Packaging, Testing, and Characterization of MEMS/MOEMS IV*. 2005. 173-181.
- Onuma, K., K. Tsukamoto, and S. Nakadate. "Application of Real-Time Phase Shift Interferometer to the Measurement of Concentration Field." *Journal of Crystal Growth*, 1993: 706-718.
- Osterberg, P. M., and S. D. Senturia. "M-TEST: A Test Chip for MEMS Material Property Measurement Using Electrostatically Actuated Test Structures." *Journal of Microelectromechanical Systems* 6, no. 2 (June 1997).
- Patterson, P. R., D. Hah, H. Nguyen, H. Toshiyoshi, R. Chao, and M. C. Wu. "A scanning micromirror with angular comb drive actuation." *International Conference on Micro Electro Mechanical Systems 2002*. Las Vegas, NV, USA, January 2002. 544-547.
- Preumont, A. *Vibration Control of Active Structures: An Introduction*. New York, NY, USA: Kluwer Academic Publishing, 2002.
- Pritt, M. D. "Phase Unwrapping by Means of Multigrid Techniques for Interferometric SAR." *IEEE Transactions on Geoscience and Remote Sensing* 34, no. 3 (1996): 728-738.

- Qin, S. Joe, G. Cherry, R. Good, J. Wang, and C. A. Harrison. "Semiconductor Manufacturing Process Control and Monitoring: A Fab-wide Framework." *Journal of Process Control* 16, no. 3 (March 2006): 179-191.
- Saha, R., and W. D. Nix. "Effects of the Substrate on the Determination of Thin Film Mechanical Properties by Nanoindentation." *Acta Materialia* 50, no. 1 (January 2002): 23-38.
- Seligson, J. L., C. A. Callari, J. E. Greivenkamp, and J. W. Ward. "Stability of Lateral-Shearing Heterodyne Twyman-Green Interferometer." *Optical Engineering*, 1984: 353-356.
- Simon, M. D., L. O. Heflinger, and S. L. Ridgway. "Spin Stabilized Magnetic Levitation." *Am. J. Phys* 65, no. 4 (1997): 286-292.
- Stengel, R. F. *Optimal Control and Estimation*. New York, NY, USA: Courier Dover Publications, 1994.
- Suzuki, T., and R. Hioki. "Translation of Light Frequency by a Moving Grating." *Journal of Optical Society of America*, 1967: 1551.
- Suzuki, T., O. Sasaki, and T. Maruyama. "Phase Locked Laser Diode Interferometry for Surface Profile Measurement." *Applied Optics*, 1989: 4407-4410.
- Suzuki, T., O. Sasaki, K. Higuchi, and T. Maruyama. "Phase-locked Laser Diode Interferometer: High-Speed Feedback Control System." *Applied Optics*, 1991: 3622-3626.
- Tadigadapa, S. A., and N. Najafi. "Developments in Microelectromechanical Systems (MEMS): A Manufacturing Perspective." *Transactions of the ASME* 125, no. 818 (November 2003).

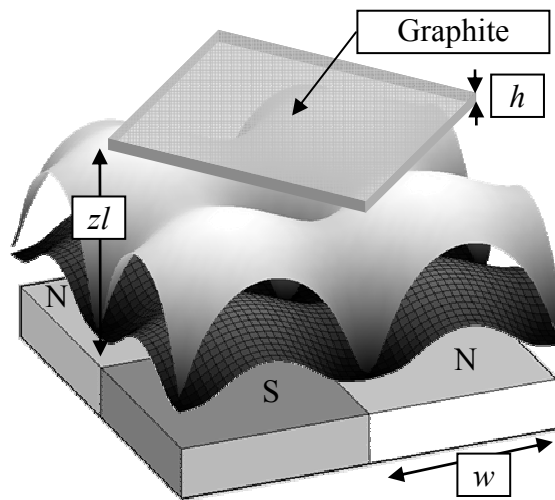
- Tang, W. C., and T.-C. H., Howe, R. T. Nguyen. "Laterally driven polysilicon resonant microstructures." *Sensors and Actuators*, 1989: 25-31.
- Tang, W. C., M. G. Lim, and R. T. Howe. "Electrostatic Comb Drive Levitation and Control Method." *Journal of Microelectromechanical Systems*, 1992: 170-178.
- Tarjan, R. E. "Applications of Path Compression on Balanced Trees." *Journal of the ACM* 26, no. 4 (1979): 690-715.
- Thomson, W. T. *Theory of Vibrations with Applications*. Englewood Cliffs, N. J.: Prentice-Hall, 1988.
- Timoshenko, S., and J. N. Goodier. *Theory of Elasticity*. 2nd Edition. New York, USA: McGraw-Hill Book Company, 1951.
- Toda, R., N. Takeda, T. Murakoshi, S. Nakamura, and M. Esashi. "Electrostatically Levitated Spherical 3-Axis Accelerometer." *IEEE MEMS 2002*. 2002. 710-713.
- Ueha, S., Y. Hashimoto, and Y. Koike. "Non-contact Transportation Using Near-Field Acoustic Levitation." *Ultrasonics* 38, no. 1-8 (2000): 26-32.
- Ugural, A. C. *Mechanics of Materials*. New York, USA: McGraw-Hill Book Company, 1991.
- Urey, Hakan. "MEMS scanners for display and imaging applications." SPIE – Volume 5604: Optomechatronic Micro/Nano Components, Devices, and Systems, 2004. 218-229.
- Veijola, T., and M. Turowski. "Compact Damping Models for Laterally Moving Microstructures with Gas-Rarefaction Effects." *Journal of Microelectromechanical Systems* 10, no. 2 (June 2001): 263-273.

- Wang, K., M. Sinclair, G. K. Starkweather, and K. F. Bohringer. "An Electrostatic Zigzag Transmissive Microoptical Switch for MEMS Displays." *Journal of Microelectromechanical Systems*, 2007.
- Ward, Mary, and Frank Briamonte. *Lucent's New All-Optical Router Uses Bell Labs Microscopic Mirrors*. Alcatel-Lucent. November 10, 1999. <http://www.bell-labs.com/news/1999/november/10/1.html>.
- Williams, F. A. "The Effect of Temperature on the Viscosity of Air." *Proceedings of the Royal Society of London. Series A, Containing Papers of a Mathematical and Physical Character*. The Royal Society, 1926. 233-237.
- Wright, M. "Miniaturization Enables Innovation—Past, Present, and Future." *Electronics Design, Strategy, News*. September 28, 2006. <http://www.edn.com/index.asp?layout=article&articleid=CA6372831>.
- Yadid-Pecht, O. "Challenges in CMOS Imager Design." *11th IEEE International Conference on Electronics, Circuits and Systems*. IEEE Xplore, December 2004. 240.
- Yeh, R., S. Hollar, and K. S. J. Pister. "Single mask, large force, and large displacement electrostatic linear inchworm motors." *International Conference on Micro Electro Mechanical Systems 2001*. Interlaken, Switzerland, January 2001. 260-264.
- Yoda, M., et al. "A MEMS 1D optical scanner for laser projection display using self-assembled vertical combs and scan-angle magnifying mechanism." *The 13th International Conference on Solid-State Sensors, Actuators and Microsystems*. Transducers, June 2005. 968-971.

Zhou, L., M. Last, V. Milanovic, J. M. Khan, and K. S. J. Pister. "Two-axis scanning mirror for free-space optical communication between UAVs." *IEEE/LEOS International Conference on Optical MEMS and Their Applications 2003*. Hawaii, USA: IEEE/LEOS, August 2003. 157-158.

## Appendix

We study 4 magnets in a north-south checkerboard configuration (**Figure 64** and reproduced here). The magnets are square with width,  $w$ , and we enforce periodic boundary conditions on the sides (the magnets straddle the origin). A plate of thickness,  $h$ , sits a distance,  $zl$ , above the magnets.



From Maxwell's equation, without current or motion:

$$\nabla \times B = 0 .$$

We let the scalar potential,  $V$ , have the following relationship with  $B$ :

$$B = -\nabla V .$$

Therefore, the Laplacian of  $V$  must be 0.

$$\nabla^2 V = 0 .$$

Let the magnetic flux density for the magnet be  $M$  (in units of Tesla). The potential function should be:

$$\frac{\partial}{\partial z} V(x, y, 0) = \begin{cases} -M & xy > 0 \\ M & xy < 0 \end{cases}$$

Let us decompose  $V$  into a Fourier series with the following form:

$$V(x, y, z) = \sum_k \sum_l f_{kl}(z) c_{kl} \sin(k\pi \frac{x}{w}) \sin(l\pi \frac{y}{w}) .$$

We can solve for  $f(z)$  by enforcing the Laplacian should be 0 for all terms over the entire domain:

$$f_{kl}''(z) - \left(\frac{k\pi}{w}\right)^2 f_{kl}(z) - \left(\frac{l\pi}{w}\right)^2 f_{kl}(z) = 0$$

subject to the boundary conditions that  $f'_{kl}(0) = -M$  and  $f_{kl}(\infty) = 0$ . An obvious solution is:

$$f_{kl}(z) = \frac{Mw}{\pi\sqrt{k^2 + l^2}} \left( e^{-\sqrt{k^2 + l^2} \pi \frac{z}{w}} \right).$$

Next, the Fourier coefficients,  $c$ , may be determined by direct integration over the domain. We find that

$$c_{kl} = \frac{16}{\pi^2} \frac{1}{kl}$$

only for odd  $k$  and  $l$ . The final equation for the potential is then

$$V(x, y, z) = \frac{16Mw}{\pi^3} \sum_{k=1,3,\dots} \sum_{l=1,3,\dots} \frac{1}{kl\sqrt{k^2 + l^2}} \left( e^{-\sqrt{k^2 + l^2} \pi \frac{z}{w}} \right) \sin(k\pi \frac{x}{w}) \sin(l\pi \frac{y}{w}) .$$

To find the force on a plate object of susceptibility,  $\chi$ , in the vertical direction, compute:

$$f(z, w, h) = \int_{z_1}^{z_1+h} \int_{-w}^w \int_{-w}^w \frac{\chi}{2\mu_0} \frac{\partial}{\partial z} (\nabla V \cdot \nabla V) dx dy dz$$

We substitute  $V$  into the equation for  $f$  and solve with Mathematica<sup>9</sup> (first taking the double summation outside of the integrals).

$$f(z_1, w, h) =$$

$$\sum_{k,l,m,n=1,3,\dots} \int_{z_1}^{z_1+h} \int_{-w}^w \int_{-w}^w \frac{\chi w^2}{\mu_0 \pi^6} 256 M^2 \frac{e^{-\frac{\sqrt{k^2+l^2}\pi z}}{w} \sqrt{k^2+l^2} \pi^2 \sin\left[\frac{k\pi x}{w}\right] \sin\left[\frac{l\pi y}{w}\right] e^{-\frac{\sqrt{m^2+n^2}\pi z}}{w} \pi \sin\left[\frac{m\pi x}{w}\right] \sin\left[\frac{n\pi y}{w}\right]}{klw^2} dx dy dz$$

$$+$$

$$\sum_{k,l,m,n=1,3,\dots} \int_{z_1}^{z_1+h} \int_{-w}^w \int_{-w}^w \frac{\chi w^2}{\mu_0 \pi^6} 256 M^2 \frac{e^{-\frac{\sqrt{k^2+l^2}\pi z}}{w} \sqrt{k^2+l^2} \pi^2 \cos\left[\frac{k\pi x}{w}\right] \sin\left[\frac{l\pi y}{w}\right] e^{-\frac{\sqrt{m^2+n^2}\pi z}}{w} \pi \cos\left[\frac{m\pi x}{w}\right] \sin\left[\frac{n\pi y}{w}\right]}{lw^2} dx dy dz$$

$$+$$

$$\sum_{k,l,m,n=1,3,\dots} \int_{z_1}^{z_1+h} \int_{-w}^w \int_{-w}^w \frac{\chi w^2}{\mu_0 \pi^6} 256 M^2 \frac{e^{-\frac{\sqrt{k^2+l^2}\pi z}}{w} \sqrt{k^2+l^2} \pi^2 \sin\left[\frac{k\pi x}{w}\right] \cos\left[\frac{l\pi y}{w}\right] e^{-\frac{\sqrt{m^2+n^2}\pi z}}{w} \pi \sin\left[\frac{m\pi x}{w}\right] \cos\left[\frac{n\pi y}{w}\right]}{kw^2} dx dy dz$$

= (each internal summation is nonzero iff  $k = m$  and  $l = n$ )

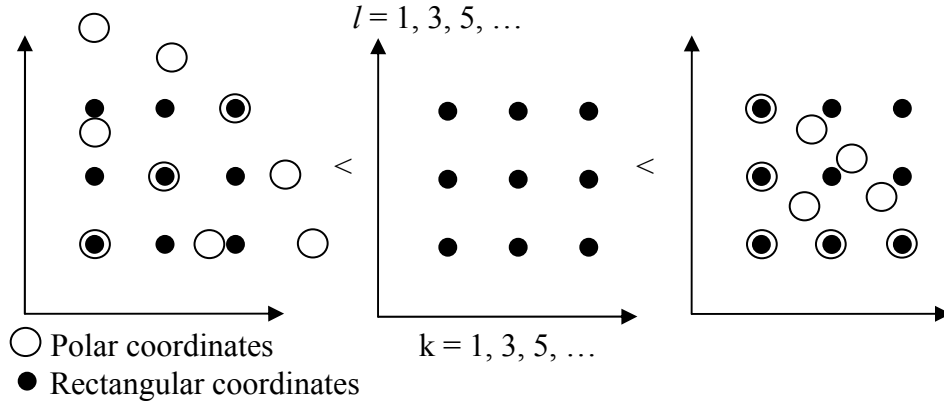
$$\sum_{k,l=1,3,\dots} \int_{z_1}^{z_1+h} \frac{512 \chi e^{-\frac{2\sqrt{k^2+l^2}\pi z}}{w} \sqrt{k^2+l^2} M^2 w}{\mu_0 k^2 l^2 \pi^3} dz$$

= (switching integration and summation)

$$\int_{z_1}^{z_1+h} \sum_{k,l=1,3,\dots} \frac{512 \chi e^{-\frac{2\sqrt{k^2+l^2}\pi z}}{w} \sqrt{k^2+l^2} M^2 w}{\mu_0 k^2 l^2 \pi^3} dz$$

To further simplify such an expression, we must switch the double summation of  $k$  and  $l$  to polar coordinates,  $r$  and  $\theta$ . However the points for the summation will change as we are no longer using a regular grid. Fortunately, we can bound the result between two polar coordinate summations that are easier to carry out.

<sup>9</sup> <http://www.mathematica.com>



Substituting  $l = r \sin \theta$  and  $k = r \cos \theta$ , where  $\theta$  is summed over  $2r - 1$  equally spaced angles from  $\frac{1}{r}$  to  $\frac{\pi}{2} - \frac{1}{r}$ , we have:

$$\int_{z_1}^{z_1+h} \sum_{r=1,3,\dots} \sum_{\theta=\frac{1}{r}, \frac{3}{r}, \dots, \frac{\pi}{2} - \frac{1}{r}} \frac{512\chi e^{\frac{2\sqrt{2}r\pi z}{w}} M^2 w}{\mu_0 2^{3/2} r^3 \text{Cos}[\theta]^2 \text{Sin}[\theta]^2 \pi^3} dz < f(z_1, w, h) < \int_{z_1}^{z_1+h} \sum_{r=1,3,\dots} \sum_{\theta=\frac{1}{r}, \frac{3}{r}, \dots, \frac{\pi}{2} - \frac{1}{r}} \frac{512\chi e^{\frac{2r\pi z}{w}} M^2 w}{\mu_0 r^3 \text{Cos}[\theta]^2 \text{Sin}[\theta]^2 \pi^3} dz$$

We can integrate over  $\theta$  separately to find an average for each  $\theta$  term.

$$\int_{z_1}^{z_1+h} \sum_{r=1,3,\dots} \frac{4096\chi e^{\frac{2\sqrt{2}r\pi z}{w}} M^2 w}{2^{3/2} \mu_0 r^2 \pi^4} dz < f(z_1, w, h) < \int_{z_1}^{z_1+h} \sum_{r=1,3,\dots} \frac{4096\chi e^{\frac{2r\pi z}{w}} M^2 w}{\mu_0 r^2 \pi^4} dz$$

Each series drops off quickly with  $r$  – so quickly, that only the first term is needed.

$$\int_{z_1}^{z_1+h} \frac{4096\chi e^{\frac{2\sqrt{2}\pi z}{w}} M^2 w}{2^{3/2} \mu_0 \pi^4} dz < f(z_1, w, h) < \int_{z_1}^{z_1+h} \sum_{r=1,3,\dots} \frac{4096\chi e^{\frac{2\pi z}{w}} M^2 w}{\mu_0 \pi^4} dz$$

And so

$$\frac{2048(e^{\frac{2\sqrt{2}\pi z_1}{w}} - e^{\frac{2\sqrt{2}\pi(h+z_1)}{w}}) M^2 w^2 \chi}{2^{3/2} \pi^5 \mu_0} < f(z_1, w, h) < \frac{2048(e^{\frac{2\pi z_1}{w}} - e^{\frac{2\pi(h+z_1)}{w}}) M^2 w^2 \chi}{\pi^5 \mu_0}$$

We can use the simplification that for  $x$  near 0,  $e^x \approx (1+x)$ . Let us also change  $z_1$  back to

$z$ .

$$\frac{512M^2\chi hw^3}{\pi^6\mu_0 z(h+z)} < f(z, w, h) < \frac{1024M^2\chi hw^3}{\pi^6\mu_0 z(h+z)}$$

Therefore,

$$f(z, w, h) = c \frac{M^2\chi hw^3}{\mu_0 z(h+z)}$$

So the general relationship holds (we replace  $M = B$ ), and for our configuration, we must fit a constant. Also, we convert the force on the proof mass to a pressure by dividing through by the area over which the force is exerted,  $4w^2$ . We found through experiments:

$$p(z, w, h) \approx 0.0123 \frac{\chi}{\mu_0} B^2 \left( \frac{hw}{(z+h)z} \right)$$